MASTERARBEIT / MASTER'S THESIS

Titel der Masterarbeit / Title of the Master's Thesis

„Morpho-Kinematics of star forming galaxies

in the field of Abell 2163 "

verfasst von / submitted by

Veronica Menacho Menacho, Bakk. rer. nat.

angestrebter akademischer Grad / in partial fulfilment of the requirements for the degree of

Master of Science (MSc)

Wien, 2018 / Vienna 2018

Acknowledgements

Contents

Abstract

The present thesis aims to study the kinematics of a sample of star forming disk galaxies in different environments and to analyse the imprints of physical transformation processes that are observed in the galaxy sample on the kinematics and morphology.

In the universe, galaxies are observed in different environments. Isolated field galaxies are expected to show regular morphology and kinematics. However, if their gravitational potential is affected they will change either their structure or kinematics, or both. On the other hand, galaxies found in rich groups and clusters of galaxies, which are situated in dense environments, undergo a much more faster physical transformation ruled by their interplay with the surrounding medium. Gravitational interactions such as Merging and Harassment drastically alter their morphology and kinematics, whereas Ram Pressure Stripping (RPS) acts only on the gas component - which is stripped away - preserving their morphology. Signs of these processes are imprinted in the rotation curve and in the morphology of those galaxies.

This thesis, which is part of a collaboration of two groups around B. Ziegler in Vienna and S. Maurogordato in Toulouse, is based on spectroscopic observations carried out with VLT/VIMOS (Very Large Telescope / VIsible MultiObject Spectrograph) instrument between 2005 and 2011. Additionally, galaxy structural parameters were either taken from my Bachelor Thesis (Menacho (2012)) or estimated in the present work following the method described there. As the aim was to observe cluster members and to study galaxy transformation processes, the majority of the selected targets display irregularities in their kinematics and morphology. This work focuses principally on galaxy members of the massive cluster Abell 2163 and compares the derived galaxy properties of cluster members and non members. Non cluster members include galaxies in groups, interacting pairs, mergers and isolated galaxies.

The sample consists of 53 galaxies in a redshift range from z=0.05 to z=0.4. Their stellar masses vary between 10^9 and 10^{11}. Balmer recombination lines: Hα, Hβ and the forbidden [OIII] λ5007 emission lines were used to extract kinematic information such as the maximum rotation velocity, the dynamical mass and the shape of rotation

curve. R- and K-Band photometry was used for the morphological analysis.

From the galaxy sample, half of the galaxies are cluster members, whereas slightly more than half of them exhibit regular rotation curves. Only one third of the non-cluster members group are kinematically relaxed systems. In total, 23 galaxies exhibit regular rotation curves, but only 19 galaxies with photometric information about stellar masses were used for the Tully-Fisher analysis.

Galaxies with distorted rotation curves by means of their morphology were compared to rotation curves of simulated and observed galaxies, which are undergoing a physical transformation. This analysis was used to identify the most important mechanisms e.g RPS, Merging, Tidal interaction acting in the observed galaxies. Finally, additional information about stellar masses allow for a deeper understanding of the physical processes playing a role in each galaxy, whereas the global analysis gives clues about galaxy evolution processes.

Chapter 1

Introduction

The galaxies of the Universe and their physical laws have fascinated the astronomical community from the very beginning. The knowledge about the diversity of galaxy populations has been accelerated with the development of new powerful and sensitive astronomical instruments. Since the last decade, when deep surveys appeared, properties such as stellar mass, gas, dust content, metallicity and photometric colours have shown that a large diversity exists among galaxy populations that evolves with redshift. More recently, galaxy samples have become more complete enabling statistical studies, which have resulted in a much better understanding of the processes of galaxy formation and evolution. Processes such as cosmic star formation rate, quenching, nuclear activities, environmental processes, feedback and star formation history.

This progress was made possible thanks to the successful combination of observational data and theoretical analysis. Numerical simulations play a crucial role in the understanding the observed assembly of galaxies and helps to constrain and optimise analytical models.

Up till now, interesting findings regarding the galaxy evolution have been made, such as the peak of the star formation rate at $z \sim 2$ Madau and Dickinson (2014), the colour information of active and passive galaxies Baldry et al. (2004) De Lucia et al. (2007), the mass and luminosity function evolution with their characteristic M^* and L^* Peng et al. (2010b) Peng et al. (2012) and the transformation of two massive disk galaxies into an elliptical galaxies due to merging. However, at the same time other questions still exist, e.g. the connection between different galaxy populations. Their origin and evolution are not yet fully understood. For example, the origin of lenticular galaxies is still unclear Icke (1985) likewise the origin of massive black holes at higher redshift (z>6) Mortlock et al. (2011) Shapiro (2005) or the influence of feedback processes on galaxy evolution Springel et al. (2005) Murray et al. (2005).

Many of these uncertainties arise from incomplete observational data which limits the parametrisation of physical processes in (semi)analytical models.

In the framework of galaxy evolution, the analysis of the spatial distribution of gas and stars, the dynamic structures and internal processes, the kinematic, morphologies as well as the environmental effects are clues to understand these issues.

In this context, the present master thesis describes my work with long-slit spectroscopic data and their analysis including the kinematics of star forming disk galaxies at redshift between 0.05 and 0.4. After disentangling regular and irregular galaxies by a morpho-kinematic analysis, three main goals were defined. Since the sample includes cluster- and field galaxies, for those with regular kinematics, the Tully-Fisher-Relation (TFR) could be analysed in dependence of the environment. Next, the sample selection is biased towards galaxy interactions which allows the investigation of the influence of interaction processes and environmental effects on the kinematic patterns. Finally, many other parameters such as the dynamical mass, the morphology (Menacho (2012)) and the stellar mass were all studied in dependence of the kinematics. This work results from a collaboration between research groups in Austria and France, led by Bodo Ziegler (Vienna) and S. Mourogordato (Toulouse), with the objective to study the massive and complex cluster Abell 2163.

This thesis is organised as follows:

- Chapter 1: A brief introduction.

- Chapter 2. Overview of the main topics in this thesis: Properties of galaxies, galaxy interactions and environmental effects and the Cluster Abell 2163.

- Chapter 3. The description of the physical processes responsible for the observed emission lines is described here.

- Chapter 4. In this chapter a introductory topic regarding the kinematics of galaxies is described.

- Chapter 5. This chapter outlines the data and methods used to derive the rotation curve and maximum rotation velocity. This includes the optical image, the long-slit spectroscopic data, the data reduction with VIPGI, the extraction of the observed rotation curves and the simulation of those rotation curves with a regular shape.

- Chapter 6. This chapter presents the results of the thesis and is divided as follows. First the galaxy sample is presented. Then, after a morpho-kinematic analysis, the galaxies are divided in two sub-samples, regular and irregular galax-

ies. For regular galaxies, the morphological classification with respect to Hubble type is presented. Next, the extracted and modelled rotation curves of the regular galaxies sub-Sample is presented. Furthermore, analysis of the Tully-Fisher relation, Stellar Tully-Fisher relation and dynamical mass to stellar mass ratio is presented. Finally, an analysis of the transformation mechanisms and the effect of the environment in the observed irregular galaxy sub-sample is studied.

Chapter 2

Introduction on the nature of galaxies

2.1 Properties of galaxies

A galaxy is an assembly of a huge amount of gas, stars and dust that are gravitationally bound by the same gravitational force, where the fraction of their components depends on the galaxy type. Most galaxies are surrounded by a halo of dark matter on their own. However, satellite galaxies do not have dark matter haloes, because they are embedded in the dark matter halo of their host galaxy. Interestingly, dwarf galaxies seem to be formed only from baryonic matter.

Since the first extragalactic observations were made, a diversity of galaxies in terms of morphology, mass and kinematics have been discovered. In the beginning, E. Hubble tried to classify this diversity based on its morphological characteristics, with the idea that galaxies with the same morphological appearance have similar physical properties. However, the well-known extended Hubble classification of ellipticals, lenticulars, spirals and irregular galaxies describes only a fraction of a whole zoo of galaxies with different morphological appearances - interacting galaxies, peculiar galaxies, dwarfs or AGN -. Therefore, other galaxy classifications based on luminosity, mass, star formation rate or colour exist. However, they are less popular. Nowadays, automatic approaches to classify galaxies are commonly used, especially at high redshifts, where morphological characteristics typically remain unresolved. Important parameters include the concentration of surface brightness density within radius or Sersic Index s_n, the position angle, asymmetries, smoothness and galaxy colour.

The difference between galaxy types can be understood when analysing their physical

properties. In this zoo of galaxies, I will define three groups depending mainly on the properties of star formation, kinematics and morphology. The first group consists of galaxies without, or with very low, star formation: ellipticals (E) and lenticulars (S0), which are spheroidals and disks with a prominent bulge. Since the kinematics of ellipticals are dominated by dispersion, these systems are pressure supported. However, the huge bulge ($\gtrsim$ 70% of the total mass) of lenticulars can be rotationally supported or pressure supported, whereas their disks are always rotationally supported. Their spectra mainly show features from old low-mass stars such as red giants of type G and K, whose spectra are dominated by absorption lines. In these systems, the cold gas is exhausted or below the collapse density limit, which is the reason for the low star formation. Some ellipticals and lenticulars, with an observed UV excess (Salim et al. (2012)), have been found to have low-level ongoing star formation around $\sim 0.5 M_{\odot} yr^{-1}$. This value is very low compared to their total mass. Due to the dominance of old stellar populations, they populate the red sequence of passive galaxies in the colour magnitude diagram, which also shows that these systems have large absolute magnitudes. The mass of ellipticals varies in a wide range. The less massive ones are the dwarf ellipticals (dE) with a total mass of several hundred times lower than the mass of the Milky Way. Dwarf galaxies do not follow the same relations like "normal "galaxies, mainly because they are strongly affected by internal processes such as supernovae, stellar winds or environmental effects. Recently, cold gas has been discovered in E/S0 galaxies populating the blue-sequence of star forming galaxies. This new population of galaxies appears to be the result of a recent merger which continues consuming the in-falling gas from its progenitor galaxies. Thus, they can provide a direct link between the evolutionary stage from late to early type galaxies (Wei et al. (2010)).

The next group of galaxies discussed here consists of galaxies with ongoing active star formation. They are disk galaxies with a regular morphology, i.e. galaxies in which environmental effects did not take place or their effects were very small, so that the galaxies still appear regular in morphology and kinematics. This group corresponds to spiral galaxies. In the Hubble classification, the early type spirals are of type Sa/SBa and the late type spirals are Sd/SBd. The character B indicates the presence of a bar. At high redshift, the spiral structures usually cannot be resolved, so the galaxies are called only disk galaxies. Spiral galaxies have a large amount of neutral and molecular gas. The molecular (H_2) gas to neutral atomic gas (HI) mass ratio increases from late (Sd/Sm) to early (S0/Sa) type spirals by a factor of hundred (Thronson et al. (1989)). The fraction of total gas mass to dynamical mass decreases from late to early type spirals. In late type spirals in which the atomic gas mass dominates, the total gas mass is larger than the stellar mass and represents about 50% of the total dynamical

mass (Rubin et al. (1985a)). The dust content strongly depends on the galaxy's star formation history, but in general increases with Hubble Type. Interestingly, although the dust mass is very low, typically 600 times lower than the gas mass or 0.01% to 0.001% of the total mass, data from the ISO satellite has shown that almost 30% of the emitting light in normal spiral galaxies is absorbed by dust.

In contrast to the gas mass, the stellar mass (M_*) decreases with increasing Hubble type. Typical values for the stellar mass lie between 10^9 to $10^{12} M_\odot$ and for the absolute luminosity in blue, between $-16 L_\odot$ to $-23 L_\odot$. Spirals have, in general, similar global star formation efficiencies (SFE), whereas the star formation rates do not depend on the Hubble type. The stellar population in spirals varies from old stars to young massive stars.

Early spirals are dominated by old stars, show strong absorption lines and only weak emission lines. On the other hand, late type spirals, dominated by a young stellar population consisting of hot and massive stars (OB-spectral class), show strong emission lines. Star forming galaxies are blue, when they are not affected by strong dust extinction.

The third group consists of emission line galaxies, which do not have regular kinematics or morphology. Irregular (Irr) and dwarf irregular (dIrr) galaxies are small in both size and mass, with typical diameters between 1 to 10 Kpc and 10^7 to $10^{10} M_\odot$. Due to relative higher gas and dust content, they have enhanced star formation characterising their blue colour. Dwarf irregulars (dIrr) are the less massive and smaller irregulars often orbiting huge elliptical or spirals. Despite the fact that this type of galaxies dominates in number density, dIrr are observed only in our vicinity and the Irrs compose only a fraction of the observed galaxies in the local universe (about 10%). At high redshifts they are difficult to observe due to their lower mass.(Gallagher and Hunter (1984)).

Interacting, merging or distorted galaxies form another class of galaxies in this group. They are preferentially found in dense environments such as in groups and cluster. Due to interaction processes, instabilities and shock fronts, the gas is compressed and star formation is triggered. Several studies (Di Matteo et al. (2007), Young et al. (1996), Solomon and Sage (1988)) show that the star formation efficiency is enhanced in merging and interacting systems by a factor of 1.5 to 5, depending on the merger stage with higher factors for close interactions. This episode of starburst exhausts the available cold gas rapidly. Gas is converted into stars heating the ISM. The result is a passive galaxy without any "fuel" left (at least cold gas) for further star formation. Details about interaction processes, environmental effects in clusters of galaxies are described in the next sections.

At this point, I want to emphasise that classifying galaxies within specific physical parameters is a very difficult task with relatively large scatter. The values specified in this section correspond to analysis of galaxies in the local universe, while galaxies at high redshift have different ratios in their physical properties, e.g. the morphology-density distribution changes at high redshift and morphological structures such as clumpy and peculiar types dominate the galaxy population.

2.1.1 Evolution of galaxies

Deep field observations reveal that, depending on the age of the universe, different populations of galaxies exist. This is due to galaxy evolution processes driven by internal secular evolution or external processes, e.g. environmental effects.

Thus, observations at various redshifts provide insight into the evolution of galaxies over time. How did $S0$ and ellipticals form? Which processes are responsible for the quenching of galaxies? Numerical simulations show that merging processes of two massive progenitors lead to the formation of an elliptical galaxy. This scenario is supported by observations of merging galaxies at different stages as shown in Fig: 2.2. However, the origin of $S0$ galaxies is still an open question. Ram pressure stripping in star forming disk galaxies in cluster environments is one of the proposed mechanisms (Bösch et al. (2013a)). Also the merging of dark matter haloes and the subsequent heating of the cold gas content is suggested for the formation of S0 galaxies, at least for galaxies with halo masses $> 10^{12} M_\odot$.

Peng et al. (2010b, 2012) describe a simple model of quenching mechanisms: 1) Mass quenching for galaxies with $M > M^* \simeq 10^{10.6} M_\odot$ at a rate proportional to the specific star formation rate (sSFR $= SFR/Mass$). 2) Environment quenching in satellite galaxies falling into massive dark matter halos. 3) Quenching in dependence of the environment, e.g. due to merger.

Analysis of the intrinsic properties of high redshift galaxies gives clues about galaxy evolution in a statistical point of view, when they are considered to be progenitors of present galaxies.

2.1.2 Surface brightness profiles

The surface brightness distribution is fundamental to derive structural parameters of galaxies. Ellipticals and bulges have large concentrations of light in their central

part, i.e. their radial brightness profile decreases rapidly, whereas disk galaxies have shallower profiles. Different profiles are available with a dependence on morphology. Nevertheless, the **Sersic profile** as described in Equation (2.1) is commonly used.

$$\Sigma(r) = \Sigma_e exp[-k((\frac{r}{r_e})^{1/n} - 1)] \tag{2.1}$$

where Σ_e is the effective surface brightness, and r_e is the effective radius within which half of the total flux is emitted . The parameter n is the sersic number or concentration parameter. k is a parameter connected to n (Peng et al. (2002)).

The surface brightness of ellipticals is well described by a **de Vaucouleurs profile**, which is a special case of a sersic profile with $n = 4$. Disk galaxies can be well described by a two component fit. For the bulge the **de Vaucouleurs profile** is used and for the disk component an **exponential profile** is suitable. The latter is derived from the sersic profile with $n = 1$ (2.2)

$$\Sigma(r) = \Sigma_e exp(\frac{r}{r_s}) \tag{2.2}$$

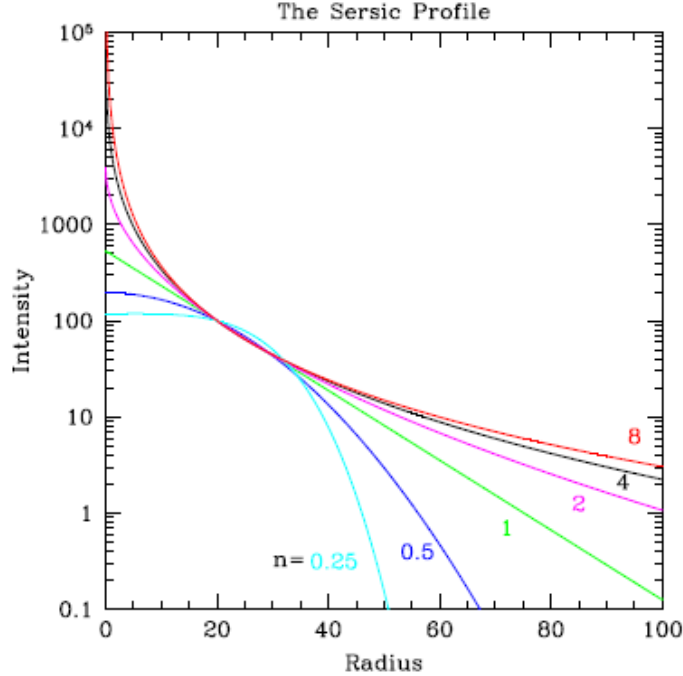with r_s is the scale length of the disk.

Figure 2.1: Sersic profiles for different sersic numbers from Peng et al. (2002).

Despite the wide use of *de Vaucouleur* and *exponential profiles*, many galaxies show light distributions that are best fitted by an intermediate *sersic profile*. Ellipticals and

bulges show Sersic indexes larger than $n > 2$, whereas intermediate luminosity systems have $n \approx 1 - 2$ and disk components are fitted well with $n \leq 1$. For bars, spiral arms, mergers and other irregularities in the light distribution, the two component fitting does not reproduce the entire galaxy surface brightness distribution. In these cases, other more complex profiles may be used during the fitting process. Nowadays, this is performed using different automatic fitting routines like *GALFIT*.

2.2 Galaxies in dense environments

Galaxies can be found in many different environments. Field galaxies are isolated systems. Galaxy pairs, groups and clusters are systems of galaxies which are gravitationally bound by the same force. Their number counts range from two to several hundreds or thousands of galaxies. Surveys and deep observations show that galaxy interactions occur frequently in dense environments and are therefore important for galaxy evolution. The correlation of galaxy properties for the environment and their evolution with redshift is still under investigation.

Dressler (1980) analysed populations of galaxies and found a dependence on morphology with environment. The number of passive galaxies (E and S0) increases proportional to the number density of galaxies and with the proximity to the cluster centre. Star forming galaxies populate preferentially less dense environments.

2.2.1 Cluster of galaxies

Clusters are the largest gravitationally bound systems. Large dark matter masses are needed to explain observed gravitational effects such as strong lensing. The baryonic matter component is dominated by kinematically hot gas, observable in X-rays, which is filling the intracluster medium (ICM). Secondary, the mass-fraction of galaxies in clusters is of the order of only 10%. Clusters have typical masses ranging from 10^{14} to $10^{15} M_{\odot}$ within diameters of 5 to 10 Mpc. Ellipticals and lenticulars dominate the population of galaxies following the morphology-density relation, therefore the colour magnitude diagram is dominated by red sequence galaxies. Nevertheless the fraction of blue galaxies increases with redshift. This is known as the Butcher-Oemler effect (Butcher and Oemler (1984)). Desai et al. (2007) have studied the morphology of cluster galaxies up to a redshift of $z = 0.8$ and have found that at $z = 0.6$ the number of S0 galaxies is increasing, whereas at the same rate the number of spirals decreases. However, the fraction of ellipticals remains constant. This result gives evidence that

SO galaxies are the successors of spiral galaxies, which were environmentally quenched in structures that have grown in mass according to the ΛCDM model.

Many galaxy properties are linked to the environment: luminosity, red- and blue-galaxy fractions, colours and AGN activity. These quantities seem to follow the morphology-density relation, whereas the star formation rate in active galaxies does not change with environment.

2.2.2 Environmental effects - Galaxy interaction processes

Galaxies in dense environments, like rich groups and clusters, are frequently exposed to gravitational interactions with the surrounding medium. Merging is commonly observed in groups, whereas in massive clusters ram pressure stripping (RPS), strangulation and harassment are frequent phenomena that are happening on timescales of Gyrs. Different dynamical processes affect the galaxy properties and their evolution. In the cluster Abell 2163, as well as other massive clusters, ongoing mergers and post-merging processes are a common occurrence.

Ram Pressure Stripping (RPS)

Massive galaxy clusters, embedded in massive haloes, have a dense intracluster medium (ICM). Galaxy members moving at high speeds through the cluster experience a force proportional to the intracluster density and their squared velocity, $P = D \times v^2$. The affect of this force is strong in gas rich galaxies, specially if they fall into the cluster centre, where the density of the ICM is much higher. The gas component that is less strongly bound to the galaxy is stripped away if the ram-pressure force is larger than the gravitational potential force. The efficiency of gas loss by RPS depends strongly on the inclination angle of the in-falling galaxy and its structure. This can be seen in the top if Fig: 2.2. When the gas tail behind the galaxy is compressed and heated in interaction with the ICM, it starts forming new stars. In some galaxies a stream of dust is also observed. This phenomenon mainly removes the gas component and leaves the galaxies without morphological change, is the principal mechanism for the transformation of blue star forming galaxies into red passive galaxies. The timescale for this transformation is approximately 10^7 Yrs (Gunn and Gott (1972), Abadi et al. (1999), Moore et al. (1999)).
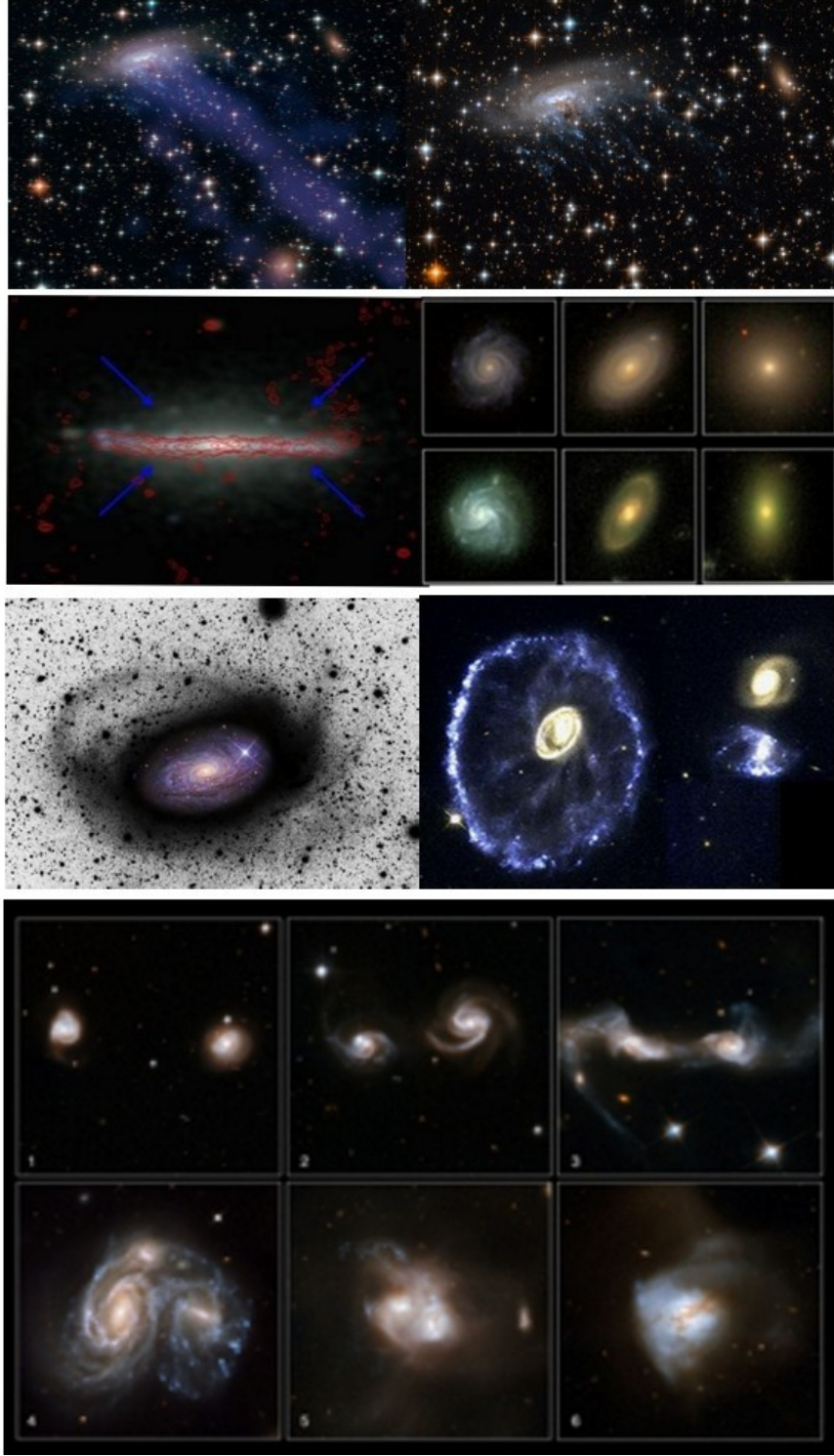
Figure 2.2: Collection of interacting galaxies taken by the Hubble Telescope. First row: Ram pressure stripping effect. Second row: Strangulation of galaxies. Third row: To the left, Cannibalism. On the right, Harassment. Forth and fifth row: Tidal interactions and Merging respectively. (Credit: NASA, ESA, the Hubble Heritage (STScI/AURA)-ESA/Hubble Collaboration, and A. Evans (University of Virginia, Charlottesville/NRAO/Stony Brook University))

Strangulation

Neutral gas reservoirs are located in the halos of galaxies. As soon as this hot gas cools down, it falls into galaxies providing a supply of metal-poor cold gas to form new stars. This gas supply can be ceased by two mechanisms: Ram Pressure Stripping and Strangulation. Although both processes remove gas from galaxies without modifying their morphology, they can be distinguished by means of the metallicity and stellar mass parameters. Figure 2.3 illustrates the difference in both mechanisms. Galaxies form new stars from inflowing cold gas. Consequently the metallicity and the stellar mass increase with time. But this increase in metallicity is not strong, since the new metal poor gas reduces the metal content in the galaxies. If RPS acts on a galaxy, the gas supply is stripped away immediately and the star formation is halted. Resulting in the stellar mass and metallicity content being similar to the progenitor galaxy. In the Strangulation mechanism, as seen in the second row of Figure 2.2 and in the illustration 2.3, the gas reservoir in the halo is heated due to environmental effects. The galaxy continues forming stars until the gas in its disk is exhausted. Since the metal poor gas from the in-falling gas reservoir is absent, the metallicity increases steeply (Peng et al. (2015)). Strangulation acts on long timescales, > 3 Gyr, and similarly to RPS it does not change the structure of the galaxy (Kawata and Mulchaey (2007)). Both mechanisms are observed in clusters and compact groups of galaxies (Rasmussen et al. (2008).

Tidal Interactions

Two galaxies with low relative velocities, i.e. low velocity dispersion, passing close to each other, shown in the forth row of Figure 2.2, experience gravitational interactions that produce instabilities in the intergalactic medium. Consequently, the gas velocity dispersion increases until the gas is finally removed, building up a tidal arm with a filamentary structure in peripheral regions of the galaxies. These tidal effects can be observed through distortions in the morphology and kinematics in one part of the galaxy disk. Typical signs are deviations in the spiral structure from the galactic plane as well as distortions of the velocity field (Eneev et al. (1973), Aguilar and White (1985)). Such close interactions induce starburst activities in both galaxies.

Merging

As a result of tidal forces, interacting galaxies loose angular momentum. If their dispersion velocities decrease sufficiently so that they can not escape the gravitational
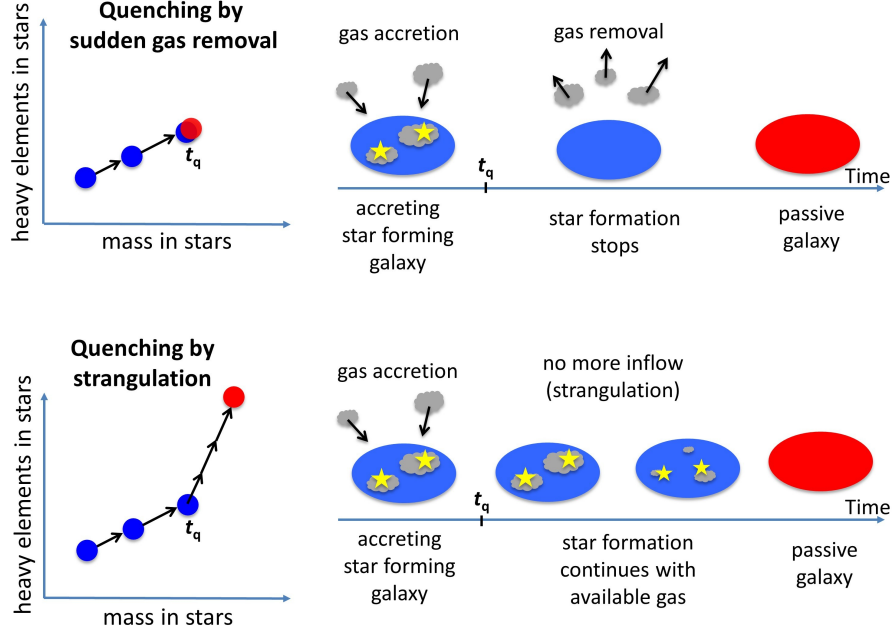
Figure 2.3: Illustration of Ram Pressure Stripping and Strangulation processes taken from Peng et al. (2015)

forces, the interacting systems will collide slowly governed by the dynamical friction till the relaxation, this is seen in the fifth row of Figure 2.2. During the merging process, the shocked ISM compresses the cold gas triggering an episode of starburst. This exhausts the cold gas supply for subsequent star formation. Velocity dispersion begins to dominate the kinematics of the stars and in major mergers an elliptical galaxy forms. Typical timescales of merging processes are < 1 Gyr (Aarseth and Fall (1980)).

Cannibalism

Luminous giant galaxies may grow in mass also by accretion of small galaxies with low dispersion velocities. Once the small galaxies fall into the potential of the host galaxy, dynamical friction causes them to fall into the massive galaxy. As a result, the low mass galaxy is destroyed and redistributed according to the dynamics of the system. This process is observed in the third row on the left in Figure 2.2). This process progressively enhances the luminosity of the dominant galaxy. Such galaxies are often giant cD galaxies and are located at the centre of galaxy clusters (Hausman and Ostriker (1978)).

15

Harassment

This phenomena arises from rapid encounters of small disk galaxies with larger cluster galaxies. During each passage, strong tidal shocks produce multiple bursts of star formation, disturb the orbits of up to 90% of the stars, this is seen in the third row on the right in Figure 2.2. Consequently, the disk galaxy is transformed into a spheroidal galaxy after a few Gyrs. Remnants of this phenomenon are observed as tidal tails in the diffuse intracluster light, that trace the path of the intruder. Afterwards about 50% of the stars move to the intracluster medium. High surface brightness (HSF) galaxies are less susceptible to harassment effects. Harassment disturbs or changes the morphology of the involved galaxies producing warps, tidal tails, bars and asymmetrical or disturbed morphologies. Additionally, it may be responsible for the transformation of the dwarf population in clusters into spheroidals (Moore et al. (1998, 1999)).

2.3 Abell 2163

Located at $z = 0.2005$ with an apparent size of 30'x30', Abell 2163 is a cluster of superlatives. Studies of its physical properties in x-rays, the optical and the radio range, reveal that this cluster is the most x-ray luminous and hottest cluster of the Abell Catalog and is also one of the most massive clusters in the universe (Maurogordato et al. (2008), Bourdin et al. (2011), Soucail (2012)). Holz and Perlmutter (2012) derived the halo mass function at redshifts $0.12 < z < 0.36$ from N-body simulations and found that Abell 2163 is likely the most massive observed cluster in the universe to date. Its mass is close to the maximum cluster masses predicted by the λCDM model. Derived from photometric and spectroscopic data in the optical range, its virial mass within a radius of 4.6 Mpc is calculated to $M_{vir} = 3.8 \pm 0.4 \, 10^{15} M_{\odot} \, h_{70}^{-1}$. This is more massive than even the Coma cluster. Its mean redshift and velocity distribution are $z = 0.2005 \pm 0.0003$ and $1434 \pm 60 \, km/s$, respectively.

A detailed study of the dynamics of the cluster have been performed by the S. Mouragourdato's group in Toulouse (Maurogordato et al. (2008)). Their analysis is based on optical observations shows a cluster with a complex structure. The projected galaxy density distribution is derived from multicolour (R and G Band) wide-field imaging and spectroscopic data and exhibits a sub-clustering morphology, see Fig: 2.4 for reference. Two dominant components are observed in the X-ray and optical images. A bimodal main component **A** in the centre of the system and a northern smaller component **B**. Additionally, three substructures **C**, **D** and **E** can be identified

in the optical. They are classified as groups and located in the east, the west and south of the cluster.The main component **A** with a bimodal structure, denoted as **A1** and **A2**, dominates the central potential and hosts the two brightest cluster galaxies (BCGs) in the centre of each structure, east and west of the central part. The centre has an apparent size of $10' \times 10'$. Its distribution of galaxy densities is elongated from east to west. The velocity distribution also exhibits a bimodality in the NE-SW with a velocity gradient of $1250\,Km/s$. The component B is classified as s sub-cluster and appears to be connected to the main component A through a bridge of galaxies. The analysis of the galaxy density distribution and their luminosities suggest a cluster morphology in which the outer components, the sub-cluster B and the groups C, D and E are falling into the potential of the main component A.
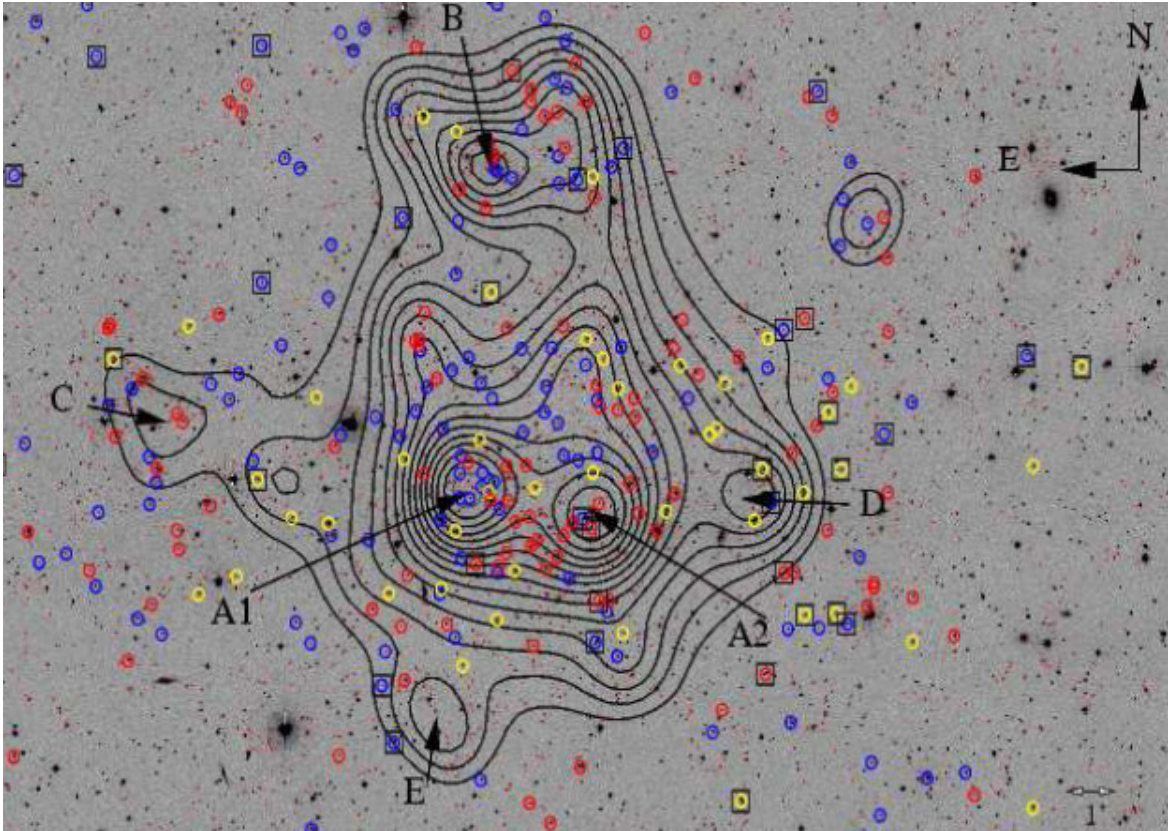
Figure 2.4: The isocontours of the projected galaxy density distribution map for galaxies with $R < 21$ magnitude overlaid on the WFI (Wide Field Imager) R-band image (Maurogordato et al. (2008))

Studies of the hot intracluster gas (ICM) component and its dynamics have been performed by Bourdin et al. (2011) by means of X-ray imaging and spectroscopic data. The gas distribution shows irregularities in the morphology, with temperature gradients resulting from shock heating, which is a typical signature of an unrelaxed system. Observations in the radio range at 20 and 6 cm show a largely extended radio

halo with a size of 2.9 Mpc crossing the centre of the cluster. Additionally, a diffuse relic is found at a distance of 2.2 Mpc from the centre. The aligned orientation of three tidal structures suggest the remnants of the bulk motion during a past merging event. The connection between radio haloes of hot massive clusters and cluster mergers is still poorly understood (Feretti et al. (2001); Feretti et al. (2004)).

Figure 2.5: On the left, the projected galaxy density map for galaxies with apparent R magnitude $R < 21$ from Observation at the CFHT telescope. The superimposed isocontours correspond to X-ray emission from $[0.5 - 2.keV]$ from the XMM-Newton Telescope (Maurogordato et al. (2008)). On the right, the radio map at 20 cm from VLA observations (Very Large Array) with overlaid from X-Ray isocontours (Feretti et al. (2001).
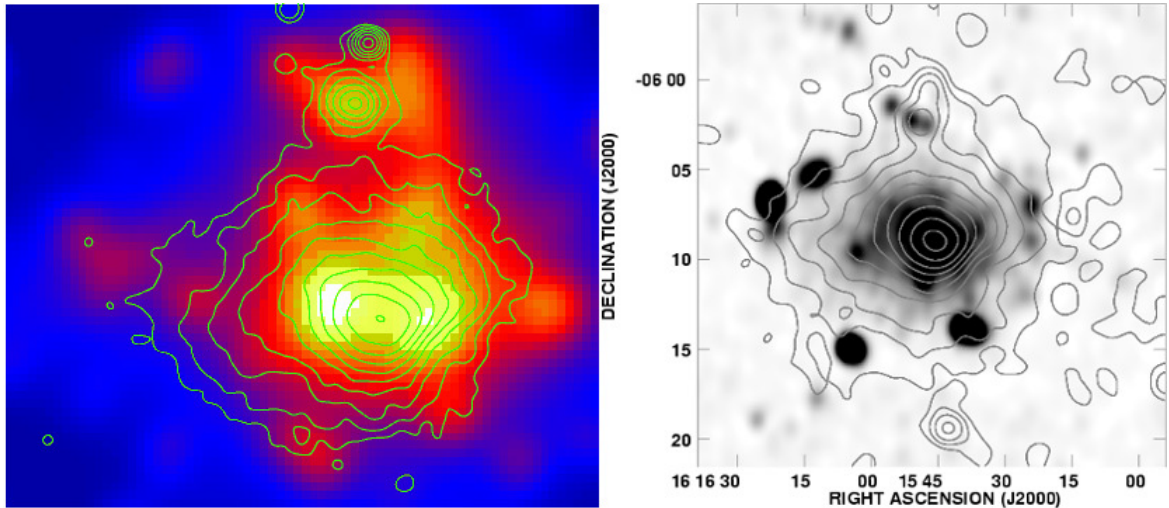
From optical analysis, the galaxy density distribution seems to be concentrated in two areas, located on the eastern and western side of the main component A. However, the concentration of the hot gas component has a peak in-between. This suggests a post-merging scenario of two sub-cluster components were the concentration of gas results from high velocity shocks (super sonic) during the collision. In this process, the hot IC-gas is adiabatically compressed, hydrostatic equilibrium is violated, this results in gas loss of the sub-cluster components. This fascinating phenomenon is comparable to the so called **"Bullet Cluster"**. (Markevitch et al. (2002)) suggests a recent merger scenario, where two sub-clusters with a mass-ratio of 1:4 collide. Thereby the A2163-A component has accreted a sub-cluster along the E-W direction.

Analysis of X-ray, optical and radio data of Abell 2163 reveals signatures of a main merger, post-merging events as well as in-falling of groups and the sub-cluster B. However, in the northern component B no evidence for previous merging events is found. For this reason, Abell 2163 is an eligible candidate to study environmental effects and galaxy evolution.

Figure 2.6: Visual image of the $10' x 10'$ Abell 2163 centre. The dark matter distribution derived from weak lensing analysis is superimposed in blue colour. The superimposed magenta colour shows the hot gas concentration from the Chandra X-Ray observation (Soucail (2012))

Chapter 3

Kinematics theory

In this charper, basic concepts of galaxy kinematicas and observational claims are described.

3.1 Rotation curves

From the Virial Theorem, in the simple case of dynamic equilibrium, the gravitational force compensates the centrifugal force in galaxies and thus, stars rotate in circular orbits.

$$\frac{mV^2}{r} = \frac{GM(r)m}{r^2} \implies M(r) = \frac{V_{rot}^2 r}{G} \tag{3.1}$$

where $V(r)$ is the circular velocity, $M(r)$ is the galaxy mass within a radius r and G is the gravitational constant.

However, the observed rotation curves of galaxies are more complex than simple Keplerian motion of stars and gas. In the outskirts the rotation velocity remains constant even if the observable matter declines exponentially. Therefore, an extra non observable galaxy component of galaxies has been introduced, namely dark matter. As result, four components are necessary to reproduce the observed rotation curves (3.2). These components are: an exponential disk of stars, gas and dust, the neutral gas outside the galaxy disk, a bulge and a dark matter halo. Thus, galaxies have a rotation velocity

$$V_{rot} = (V_{gas}^2 + V_{disk}^2 + V_{bulge}^2 + V_{halo}^2)^{\frac{1}{2}} \tag{3.2}$$

where V's correspond to the circular velocities of the different components.

Furthermore, the rotation velocity depends on the distance to the galactic centre. In the inner part, the rotation velocity increases linearly ($v(r) \propto r$) and is characterized by a rigid-body rotation with constant angular velocity. Stars move in paths that are determined by the equilibrium between the gravity and the effective centrifugal forces. On the outskirts of galaxies, the baryonic matter falls off as $v(r) \propto 1/r^{1/2}$ and the orbits are described by the Keplerian law. The Dark matter keeps the rotation curve flat $v \propto const$ in the external part of the galaxy as showed in followed figure 3.1.
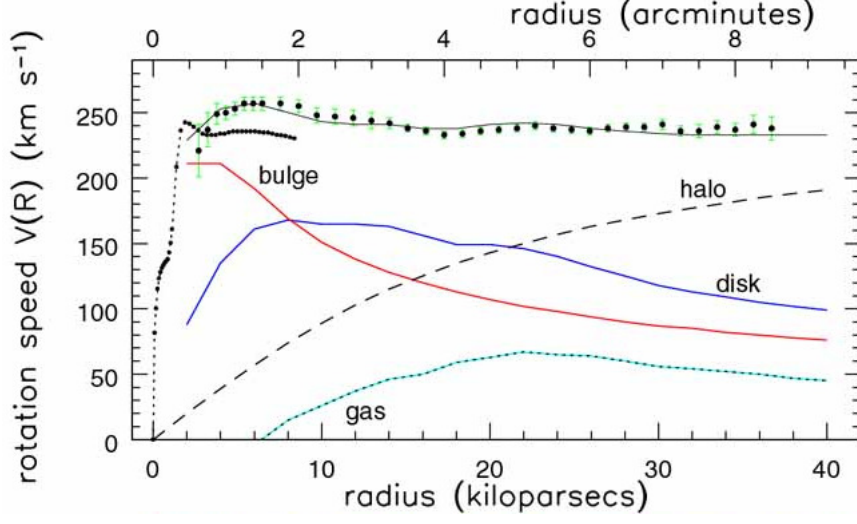
Figure 3.1: Rotation curve decomposition of NGC 7331. (Sparke and Gallagher (2007))

The dark matter halo follows a spherical symmetry distribution with a density profile described by the following equation 3.3:

$$\rho(r) = \frac{V_{rot}^2}{4\pi G r^2} \tag{3.3}$$

and their circular velocity:

$$V_{halo}^2 = \frac{GM(r)}{r} \tag{3.4}$$

Galaxies are projected with different inclinations on the sky, which induces an underestimation of the intrinsic rotation velocity and should be corrected. In extragalactic observations the rotation velocity along the line-of-sight is derived from the Doppler Shift that yields the position-velocity diagram (PV) along the galaxy major axis. Different methods can be used to derive the intrinsic rotation velocities.

3.2   Tully-Fisher Relation

From the equation of the Virial Theorem 3.1 applied to a system in dynamical equilibrium, we know that:

$$M(r) \propto rV^2 \tag{3.5}$$

The measured surface brightness I 3.6 and the luminosity L are directly linked with the radius r.

$$L = 4\pi r^2 I \Rightarrow r \propto (\frac{L}{I})^{1/2} \tag{3.6}$$

Equation 3.5 and equation 3.6 are connected as followed:

$$I\frac{M^2}{L} \propto v^4 \tag{3.7}$$

With the assumption that the mass-to-light ratio (M/L) and mean surface brightness I are constant for all galaxies, the relation luminosity-rotation velocity is derived from 3.6 $/L$ in the following way:

$$L \propto v_{rot}^4 \tag{3.8}$$

This correlation was presented by Tully and Fisher (1977) in their work on rotation velocities as method to measures cosmological distances. In spectroscopic observations the maximum width (W) of the emission lines and absorption lines approximate the rotational velocity of galaxies $W \sim 2V_{max}\, sin(i)$. The rotation velocity is proportional to the total mass and the luminosity is proportional to the stellar mass, this correlation provides a link between the baryonic matter and the dark matter component in galaxies. Therefore, studying this correlation at different redshifts provides insight into the history of galaxy evolution with time.

Chapter 4

Observations and data reduction

Using spectroscopic data in combination with photometric data, I was able to derive the kinematic properties of a sample of selected galaxies. Astronomical imaging has been used for more than hundred years to characterise objects in the universe. Thus, most of our current knowledge about the cosmos is based on the measured integrated light that is emitted due to various physical processes at different wavelengths. As a result, the transmission curve and its dependence on wavelength plays a crucial role. On the other hand, spectroscopy is another important technique in astronomy. It allows one to determine physical properties in more detail, e.g. chemical compositions, rotation and dispersion velocities of galaxies. Furthermore, only with spectroscopic data, redshifts of distant objects can be measured accurately by means of a quantitative analysis of spectral features.

4.1 The Abell2163 image

The structural parameters used in this master thesis were either derived during my Bachelor thesis "Study of galaxy structures in Abell 2163 with *SExtractor* and *GAL-FIT*"(Menacho (2012)) or estimated during this thesis following the method described in Menacho (2012). In this section, I want to present a brief overview of the data and the software used to derive the morphological parameters.

Optical imaging of Abell 2163 in the r-filter was carried out at the Canada-France-Hawaii Telescope (CFHT) with the so called "MegaCam" between April and May 2005 (Fig: 4.1). The camera consists of 36 detectors with a size of 2048×4612 pixels per each detector and a pixel scale of $0.186 \, arcsec \cdot px^{-1}$. 15 exposures of 600 seconds, corresponding to 2.5 hours were taken with seeing conditions of around 0.75 arcsec

($\sim$ 4 pixels) FWHM. The images were median-combined and have a gain value of $1.62\,e^-\,ADU^{-1}$. The final image covers one square degree (Soucail (2011)), has a photometric zeropoint of 29.89 mag and a limiting magnitude of 26.8 mag. The set of images was reduced at the Institut Astrophysique de Paris (IAP).
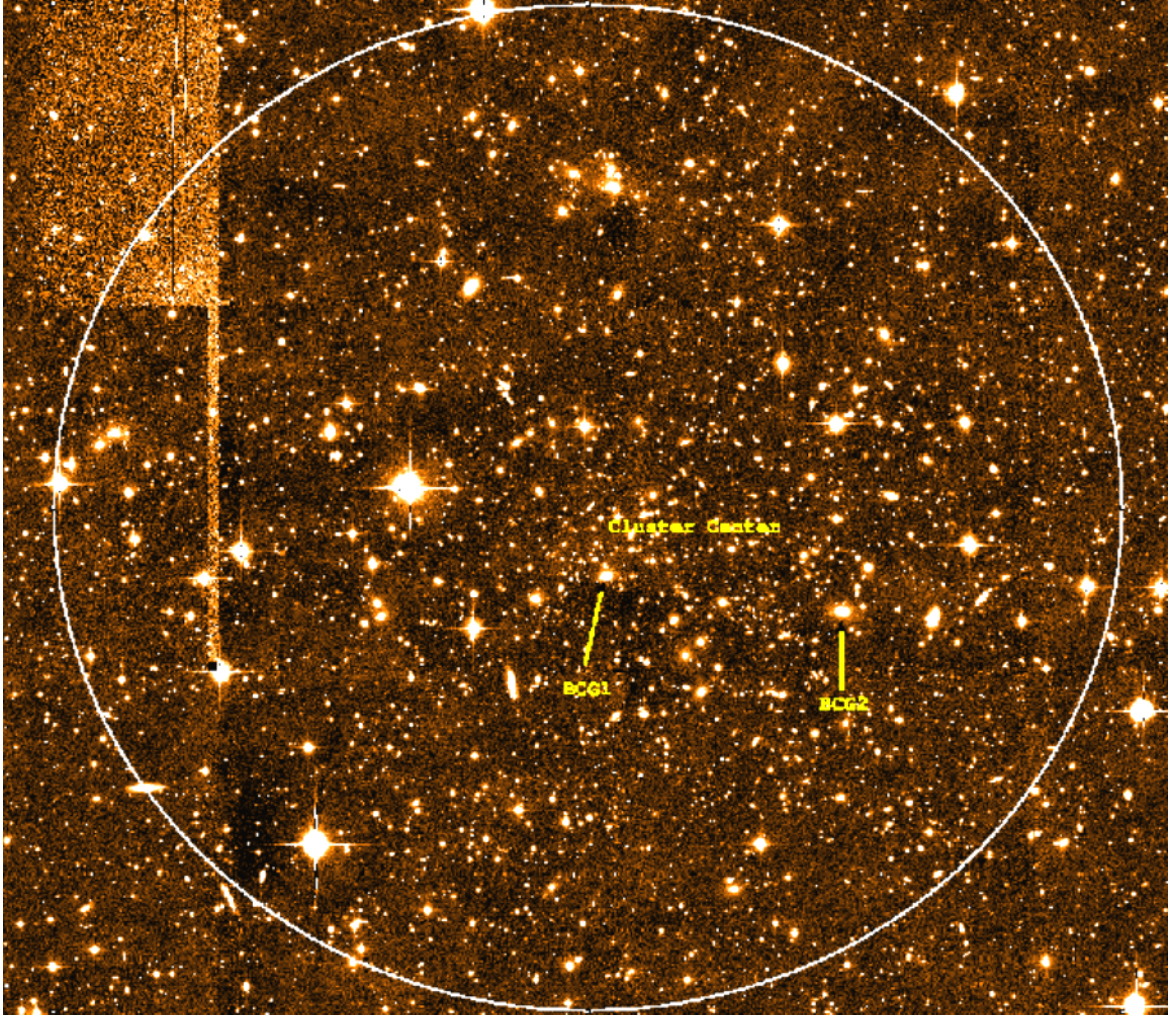
Figure 4.1: CFHT R-Band Image of the Abell 2163 region (white circle). Two prominent brightest cluster galaxies (BCG1 and BCG2) are located in centre of the cluster potential.

With this data, the structural parameters could be obtained in three steps: First, the software *PSFex* (PSF extractor) was used to extract models of Point Spread Functions (PSF) from the images (Bertin (2011, 2013)). Using these PSFs, photometry could be performed accurately.

Second, sources were identified and catalogued by the widely used software *SExtractor* (Source extractor), which automatically computes astrometric, photometric and geo-

metric parameters of all detected sources. *PSFex* and SExtractor are two widely used tools developed by E. Bertin at IAP (Bertin and Arnouts (2010), Holwerda (2005)).

Finally, the structural parameters calculated by *SExtractor* were used as initial input for the 2D fitting program *GALFIT* (Peng et al. (2002, 2010a)), which allows the fitting of various structural components within a galaxy with distinct light profile models (Fig: 4.2). A two-component fit with sersic profiles (n=1 and n=4) was used for modelling the light distribution of each galaxy. For the disk component an exponential profile with sersic number $s_n = 1$ was used and for the bulge a de Vaucouleurs profile with sersic number $s_n = 4$ was applied.
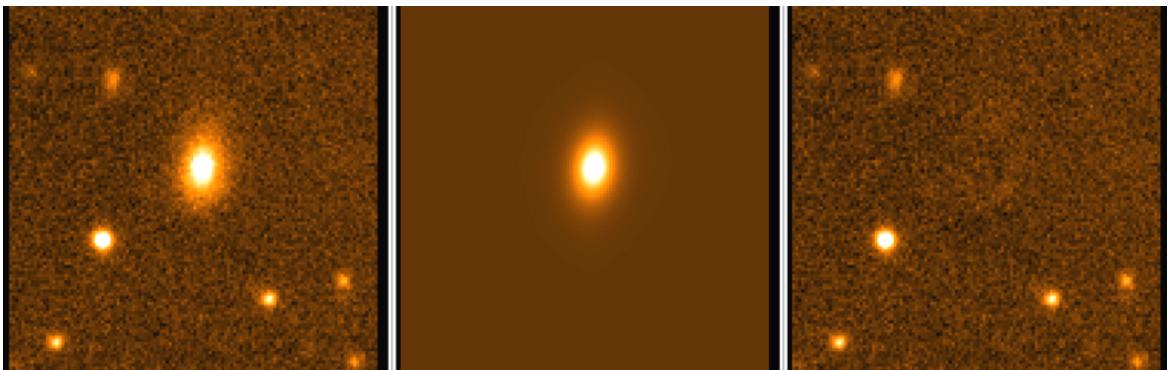
Figure 4.2: Example of GALFIT fitting output, showing the r-band Image of the galaxy Q3_w_M1_19 on the left, the GALFIT model solution on the middle and the residual image (i.e. data minus model) on the right

The structural parameters derived for each component are: the total surface brightest, the effective radius (r_e) for the bulge ($s_n = 4$) and the scale length radius (r_d) for the disk ($s_n = 1$), the axis ratio (b/a) and the position angle (PA). Most of the parameters were used for the kinematical calculations. Galaxies can be classified within a morphological Hubble type by means of the bulge-to-total-light ratios. This classification can be found in Section 5.

4.2 The spectroscopic data

All spectroscopic data used in this thesis were observed with VLT's (Very Large Telescope) UT3 Telescope in MOS (multi-object spectrograph) mode. The field of view of the instrument is split into 4 quadrants, which can be see inFig: 4.3, of sizes of $7' \times 8'$ each with a gap of $\sim 2'$ between them. The CCD camera is equipped with a detector size of $4k \times 2k$ pixels with a pixel scale of $0.205 \, arcsec \, px^{-1}$. The spectral resolution

varies between 200 and 2500 depending on the number of slits per mask (LeFevre et al. (2003)).
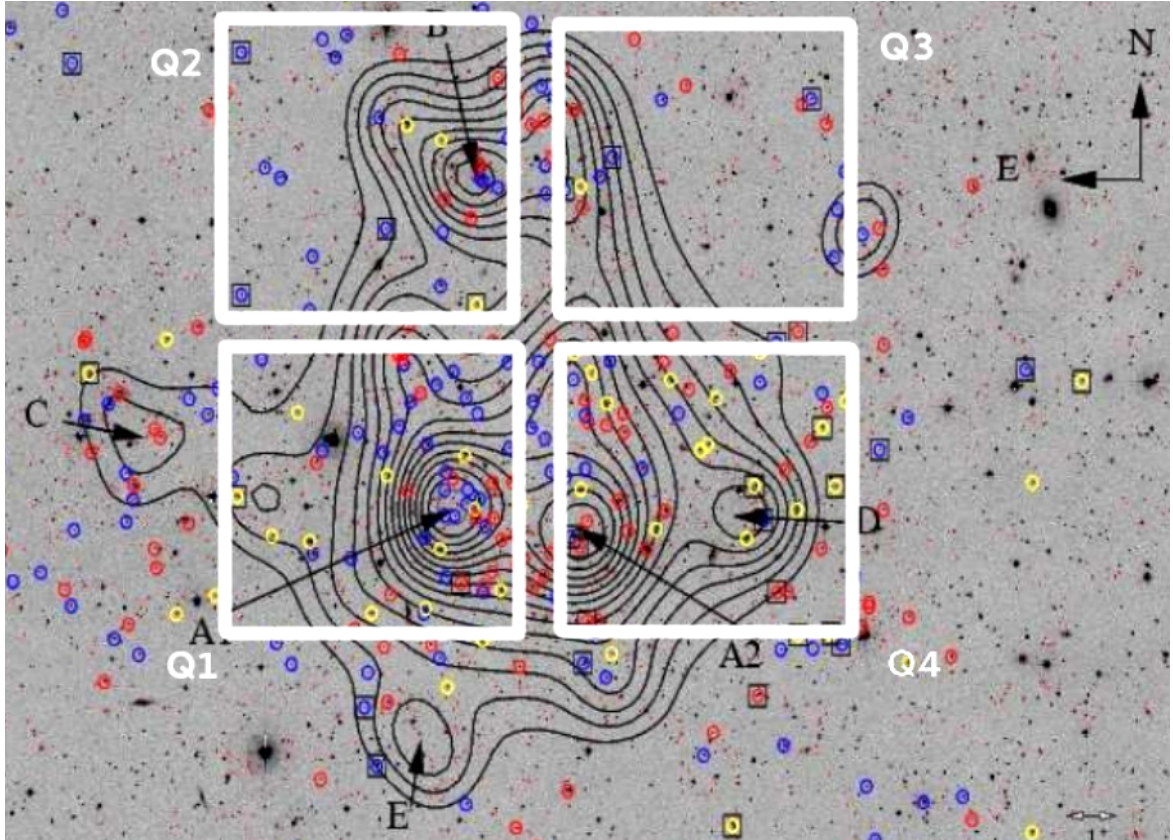
Figure 4.3: Same figure as Fig:2.4. The white boxes show the position of the 4 quadrants (Q1-Q4) of the VLT/MOS instrument (PI: B. Ziegler) in the Abell 2163 region..

The spectroscopic observations were executed by both research groups. Two observations were carried out by the S. Mouragourdato's group in 2004 and 2006, aiming to study the dynamics of the cluster (Maurogordato et al. (2008)). Their observations cover a field of $30' \times 30'$ with a slit-width of 1" corresponding to 3.31 kpc at the cluster's redshift. The old high resolution blue grism "(old-)HR-blue" provided a wavelength range of 4200–6200 Å with a spectral resolution of 2050-2550. Six pointings were observed four times with exposures of 45 min. For each pointing, 100 slits perpendicular to the dispersion direction were placed. The data reduction was performed using the VIPGI package (Scodeggio et al. (2005)).

Additionally, two observations were carried out by the B. Ziegler's group in 2010 and 2011, see Fig: 4.3, aiming to analyse interactions in the rich cluster Abell 2163 with 2-dim velocity fields, seen in Fig: 4.2. From the initially requested observing time, only a fraction has been awarded allowing only to study rotation curves of the cluster members. Two exposures of 45 min were taken per observation with seeing conditions

Grism	Filter	Spectral range	Spectral res. (1" slits)	Dispersion (Å/px)
old HR_blue	Free	415 -620 nm	2000 at 402 nm	0.51

Table 4.1: old-HR blue grism properties (vimos manual)

varying between $0.8 \leq FWHM \leq 1$ (arcsec) and a mean airmass of 1.06. The old HR-blue grism was used with tilted slits with different widths ($\leq 1''$) and $\sim 20''$ placed along the major axis of around 80 galaxies. The wavelength coverage ranges from 4200 to 6200 Å with a spectral resolution of $R = 2000$.

Tilted slits were used to measure accurately the intrinsic rotation curve of the galaxies. Furthermore, aiming to trace possible environmental signatures in the outer disks, long slits were used covering up to ~ 3 disk scale lengths (r_d) of the galaxies and leaving enough sky for an accurate sky subtraction. In many cases, neighbouring galaxies share the same slit, so that the major axis of at least one of them does not follow the slit direction anymore. In these cases, kinematic analysis was performed only if the angle between slit and major axis was less than 30 degrees.

The blue grism covering the blue optical range only, was selected in order to get spatially resolved spectra of the wavelength range that includes the recombination lines H_β, H_γ and the collisional forbidden lines [OII] and [OIII] at the cluster redshift as described in the following table 4.2.

Wavelength	H_β [Å]	H_γ [Å]	[OII] doublet [Å]	[OIII] [Å]
At rest frame	4861	4340	3726 / 3729	4958 / 5007
At $z = 0.2$	5833	5208	4471 / 4474	5949 / 6009

Table 4.2: old-HR blue grism properties (vimos manual)

A spectral resolution of 2000 allows for a resolution element of $\sim 2.24\,\mathring{A}\,(\Delta\lambda = \frac{\lambda}{R})$ enough for the deblending of the [OII] doublet.

4.2.1 Data Reduction with VIPGI

The spectroscopic data was reduced using the VIPGI (Vimos Interactive Pipeline Graphical Interface) software package (Scodeggio et al. (2005)). VIPGI works in a

semi-automatic manner. First, using the data organiser spectra are loaded and organised in pre-defined directories. After unpacking, the data is organised and viewed in a graphical interface according to its quadrant and type, e.g. bias, flat, lamp and science. The reduction procedures are described in well defined steps, during which the user is required to define all necessary input parameters. The most critical procedure, the wavelength calibration, is responsible for the quality of the data reduction and should be performed manually by the user. This is a very time consuming task and needs many iterations until a satisfactory result is achieved. The following steps were performed for each quadrant and each exposure. First, the master bias was created. Second, the first guesses were checked manually and adjusted:

- The lamp catalogue containing the wavelengths of the calibration lamp (ArHe) was checked. The alignment of the slit pattern was checked and adjusted if necessary. About 18 lines distributed throughout the spectra were chosen with emphasis on the borders (Fig: 4.4).

- Subsequently, the lamp lines, which can be seen inFig: 4.4, were selected for each slit of the mask in an iterative process until they were satisfactory for the final calibration. All this adjustments are fundamental for the proper reduction and extraction of single spectra.

- After that, the master flat and master lamp were created. At this point, the wavelength calibration was checked and, if necessary, first guesses were readjusted.

- Third, the preliminary reduction subtracts the bias and adds the extracted table to the science frames.

- Finally, a sequence of reduced single MOS scientific exposures from all possible observations were combined to enhance the signal-to-noise ratio in the final scientific exposure.
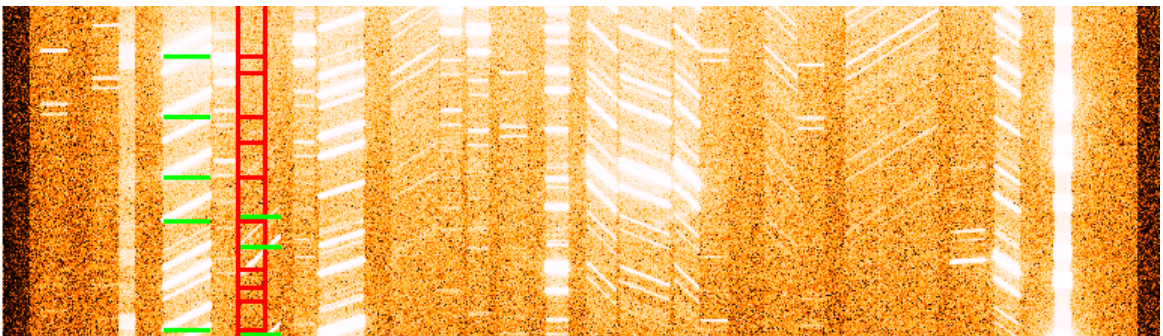

Figure 4.4: ArHe lamp spectra. Superimposed are the selected ArHe lamp lines from a catalogue (in green and red) and were used to identify these lines in the lamp spectra.

Due to low number of exposures per observation (2) and the difficulty in adding all (4) exposures of the 2010 and 2011 observations due to an upgrade in the VLT-camera, an additional cosmic cleaning process using the software MIDAS was performed before combining the reduced single exposures to the final scientific image. Finally, redshifts of the galaxies were measured by analysing their emission lines. Furthermore, the 1D-spectra used in the next step were extracted with VIPGI. Fig: 4.5 shows the short wavelength part of the reduced spectra for the quadrant 4 (exposure 2011). OII doublet of seven galaxies are shown.
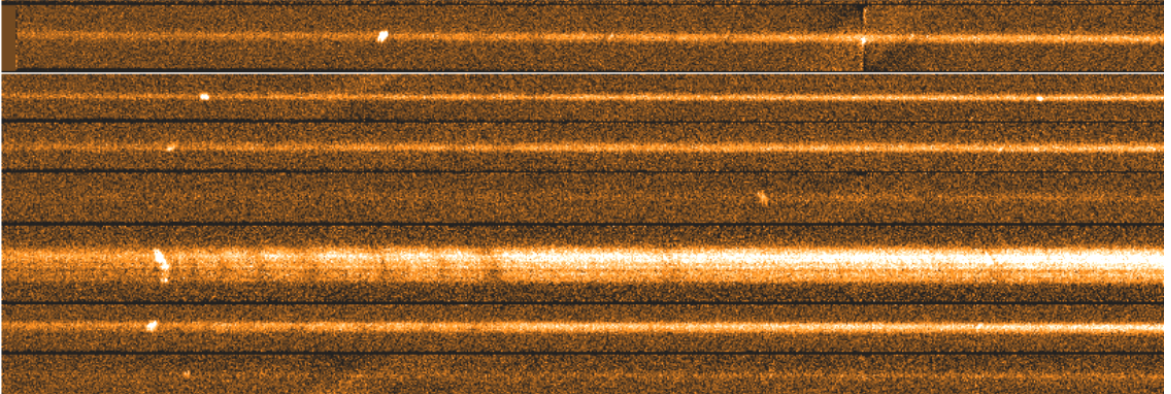
Figure 4.5: Spectra showing the OII emission line doublet from the galaxies Q4_6 to Q4_12. From the top, the first and fourth row show the spectra of the non-cluster galaxies Q4_12 and Q4_9 respectively, while the remaining spectra correspond to galaxies of the Abell 2163 cluster.

4.3 Kinematics extractions

The basic idea is to measure the shift in wavelength (spectral direction) along the major axis (spatial direction) of the emission line relative to the kinematic centre defined by the systemic velocity. Shifts are observed towards the blue and red side of the emission line centre, corresponding to the approaching and receding side of the rotating galaxy, respectively. Here, the luminous centre is defined as the centre of the galaxy with no rotation velocity ($V_{rot} = 0$).

The rotation velocity component along the line-of-sight was derived from emission lines in a semi-automatic manner. The software used for the rotation curve extraction and the rotation curve simulation is based on *MIDAS* and Python codes developed by A. Bohm and B. Bosch. The applied procedure is described in Böhm et al. (2004) and Bösch et al. (2013a,b).

Some parameters were needed as input parameters for the extraction, e.g. the redshift

of the galaxy, the line used for extraction (O[II] doublet, Hβ, Hγ, O[III]λ4958 or O[III]λ5007) and a "boxcar" size to enhance the S/N of the emission line flux, it is important that the lines are strong enough for kinematic analysis. However, enhancing the S/N at the same time reduces the resolution of the measured rotation velocities. A 3 pixel wide boxcar filter enables to measure the mean velocity every = 2.04 Kpc at $z = 0.2005$ (the Abell 2163 cluster redshift) along the major axis. For few cases, the boxcar was fixed to 4 pixels (= 2.72 Kpc at $z = 0.2005$) and for one case a 2 pixel wide boxcar (= 1.36 Kpc at $z = 0.2005$) was chosen.

Starting with the 2D spectrum centred in the emission line (Fig: 4.6), the integrated flux of the continuum plus the line (or 2 lines in [OII]) in spatial direction yield a Gaussian-like distribution profile. By fitting a Gaussian function to this profile the exact position of the centre of the peak is obtained. This luminous centre was defined as the kinematic centre of the galaxy with no Doppler shift. In many cases, most of the measured flux corresponds to the continuum emission of the stars, especially for early type spiral galaxies with low S/N emission lines. In cases, where galaxies do not show signatures of strong star formation activity in the outskirts, the peak of the Gaussian describing the luminous centre, may also be in good agreement with the potential centre, which gives the dynamical centre and consequently the kinematic centre of the galaxy. Otherwise for galaxies showing internal instabilities such as outflows due to supernovae or strong stellar winds, and also inflows of gas and posterior shocks in the ISM, as well as external effects such as RPS, merging and tidal interaction, the kinematic and luminous centre are not in good agreement.

Then, starting at the kinematic centre, the emission lines were fitted row by row in the spatial direction. One row corresponds to the defined boxcar. For the fit of one row, the integrated flux profile within the boxcar was fitted by a Gaussian providing the position of the centre of the line to 0.1 arcsec (0.33 Kpc at z=0.2005). For the [OII] doublet, two Gaussian with the same $FWHM$ and separated by $2.75(1 + z)\mathring{A}$ were used. After a cosmological correction of $(1 + z)^{-1}$, the differences in wavelength of the row fitting centre and the kinematic centre were converted into a rotation velocity along the lineofsight. If the radial velocity is much smaller than the speed of light $v(r) << c$, then the equation (4.1) is applied. This mean value corresponds to one point in the position-velocity diagram and defines the *observed* rotation curve (RC).

$$radial\,velocity\,(Km/s) \simeq speed\,of\,light\,(Km/s) \cdot \frac{shift\,(\mathring{A})}{rest\,wavelength\,(\mathring{A})} \qquad (4.1)$$

In this procedure, all rows used for fitting were carefully checked to guarantee the correctness in the resulting observed rotation curve. All fitted rows in which the
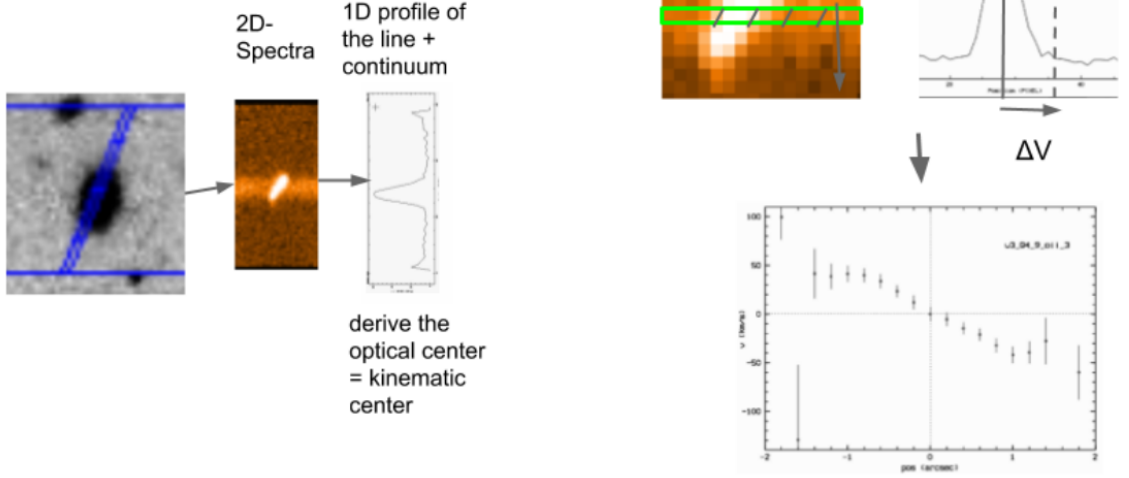
Figure 4.6: Rotation curve extraction method. On the left, as preamble, galaxies were observed with a long slit placed along the major axis. A two dimensional spectra (wavelength direction in x-axis, spatial direction along the slit in y-axis) is extracted. This 2D spectra is used to extract the 1D light profile from the continuum and emission lines. After fitting a gaussian like distribution profile, the kinematic center is determined. On the right, The emission line is fitted row by row. The kinematic luminosity peak for each row is extracted and its difference to the kinematic centre of the galaxy allows to derive the line of sight rotation velocity (Eq: (4.1))

quality of the fits were not good enough, were removed from the final position velocity diagram. The RC extraction was performed on all possible lines in each galaxy. Position-velocity diagrams with larger errors resulting from lines with lower S/N were rejected. The remaining observed rotation curves were visually inspected to distinguish between irregular rotation-curves-shapes, i.e. distorted kinematics for environmental effects studies and regular rotation curves shapes for the Tully-Fisher analysis. These observed rotation curves do not represent the true rotation velocity due to inclination i and other observational effects. Therefore, in the next step, the "rotation curve simulation", these effects were taken into account in order to derive the *intrinsic* rotation curves for galaxies showing regular rotation.

4.4 rotation curve simulations

Only galaxies with regular morphologies and observed regular rotation curves were used in this step. Galaxies with distorted or disturbed kinematics are subject to

strong instability effects in their dynamics. It is not surprising, that most of these unrelaxed systems, show merging signatures. Thus, it is not possible to derive the circular velocity and the maximum rotational velocity, which relies on the assumption of dynamical equilibrium. Therefore they were rejected for the simulation. For galaxies with two or more extracted position velocity diagrams from different emission lines, the diagram with better quality (lower errors) was chosen. In the following sections possible environmental effects observed through the morphology and kinematics of the studied galaxies are discussed.

In order to derive the intrinsic rotation curve, geometrical effects on the radial velocity component due to projection should be corrected for. The difference in the projection with respect to the line-of-sight is given by the inclination, which increases from face on galaxies with $i = 0°$ to edge-on galaxies with $i = 90°$. The maximum velocity due to the Doppler shift effect can be directly measured in edge-on galaxies, whereas galaxies with inclinations of $i < 90°$, the circular velocity component is split into two vector components and is a function of the inclination angle. One of them is the observed rotation velocity along the line of sight and the other one, connects the circular velocity with the observed rotation velocity. Other observational effects may also influence the true circular velocity, therefore galaxies with inclinations of $i > 30°$ were chosen for the kinematic analysis only.

Here the inclination was calculated using the following Tully (1988) correction for the Hubble equation:

$$ i = cos^{-1}(\frac{q^2 - 0.2^2}{1 - 0.2^2})^{1/2} + 3° \tag{4.2} $$

Besides that, the slit width influences the derived maximum velocity (Kinematics extractions), especially for very distant and apparently small galaxies. This should also be considered.

The simulation uses the structural parameters derived from $GALFIT$ and the observed position velocity information. From that, a rotating disk model of the galaxy with an exponential light profile is created (Fig:4.7). A convolution of this model with the PSF, simulates the RMS intrinsic to the observations. The spectroscopic observations are simulated by placing a slit with the same width and in the same direction onto the model galaxy. Finally, the true rotation velocity parameters are derived by matching the simulated with the observed rotation curve.

The required input parameters are the structural parameters obtained from $GALFIT$, the FWHM from the observation and the position-velocity information of the observed
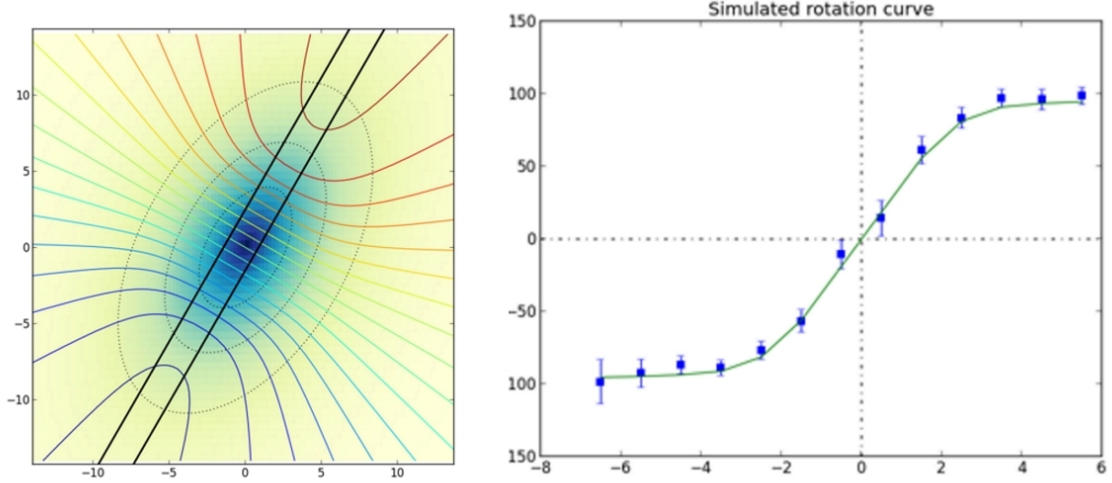
Figure 4.7: Example of a simulated rotation curve. On the left, the light profile of the galaxy Q1_8 is created by means of its structural parameters. On the right, its intrinsic rotation curve is derived when a simulated rotation curve model reproduce the observed position velocity information.

rotation curve. The position angle and the inclination calculated from the axis ratio (b/a) defines the geometric projection of the galaxy. From the r-band image (sec: The Abell2163 image) the photometric scale length in Kpc is calculated.

$$r_d\,[Kpc] = r_d\,[px] \cdot pixel\_scale\,[\frac{arcsec}{px}] \cdot (\frac{180 \cdot 3600}{\pi})^{-1}[arcsec]^{-1} \cdot D_A\,[Kpc] \quad (4.3)$$

where D_A is the angular size distance. For the redshift of the cluster Abell 2163, the angular size distance is 681.9 Mpc.

In the following, the simulation is briefly described. Beginning from an adopted intrinsic rotation equation from Courteau (1997); Courteau and Rix (1997) and 4.4, as well as the projected parameters of inclination and position angle of the observed galaxy, a projected 2-dim velocity field is created. From this the light-of-sight velocity component was derived. The assumed intrinsic rotation increases approximately linearly until it reaches the maximum followed by a region of constant or smoothly decreasing velocity. The position of the maximum velocity shows the location where the potential of the dark matter mass distribution dominates.

$$V_{rot}^{int}(r) = \frac{V_{max}(r + r_t)}{(r^a + r_t^a)^{1/a}}) \quad (4.4)$$

33

$a = 5$ is a factor controlling the sharpness of the turnover velocity. r_t is the turnover radius defined as the calculated scale length of the emitted gas $r_0 = (2 - z/2)r_d$ described in Ryder and Dopita (1994) and adjusted by Böhm et al. (2004). The free parameters for the fitting process are a and r.

Then, a projected 2-dim exponential intensity profile (eq: 4.5) is created.

$$I(x, y) = I_0 e^{-\frac{r}{r_d}} \tag{4.5}$$

where $I_0 = I(0, 0)$ is the intensity at galactic centre and $r = \sqrt{x^2 + y^2}$.

The velocity field superimposed on the intensity profile results in a rotating disc model with the same characteristics of the observed galaxy. In order to account for seeing effects, the created galaxy model was convolved with a Gaussian PSF with the observed real FWHM. Then, a virtual slit with the same boxcar width and orientation is placed exactly as it has been done during the observations. The simulated spectroscopic observation was obtained from the integrated velocity field in spatial direction within the slit, after weighting with the intensity profile centred on the kinematic centre (sec: Kinematics extractions). This leads to the simulated intensity-weighted mean rotation velocity along the line-of-sight at each spatial position and defines the simulated position-velocity diagram called *synthetic rotation velocity*. For the simulation, the parameters V_{max} and r_t parameters of the synthetic rotation curve are free during the whole fitting processes, which was done iteratively until the error-weighted χ^2 was minimised.

$$\chi^2 = \sum_i \left(\frac{V_{syn}(x_i) - V_{obs}(x_i)}{V_{err}(x_i)} \right) \tag{4.6}$$

where the variable x_i defines the position in the observed and simulated rotation curve with the velocities V_{syn} and V_{obs}. Errors are given by V_{err}.

This *Iteration Method* was developed by Takamiya and Sofue (2002) to derive velocity curves from position-velocity diagrams. It interactively corrects errors due to the galaxy projection by comparing the obtained rotation curve with the observed position-velocity diagram.

Chapter 5

Results

This chapter presents the results of this master thesis. It is divided into the following steps: Firstly, the galaxy sample, the Hubble Type classification and the morpho-kinematic classification of the galaxies are shown as a function of redshift. Secondly, the extracted and simulated rotation curves of the galaxies with regular rotation curves are presented. Next, the analysis of the Tully-Fisher relation, the stellar mass Tully-Fisher relation and the dynamical to stellar mass ratio are examined. Possible sources of bias that could affect the results of these relations are then discussed. Finally, the analysis of galaxies classified as irregular is reviewed.

For the calculations, the concordance cosmology parameters $\Omega_\Delta = 0.70$, $\Omega_M = 0.3$ and $H_0 = 70\ kms^{-1}Mpc^{-1}$ have been assumed.

5.1   The sample

As previously mentioned, this thesis is base on spectroscopic data taken by the groups S. Maurogordato in Toulouse and B. Ziegler in Vienna. A portion of the galaxies were observed by both groups, while the majority were observed by just one group. Throughout this thesis, the data reduction of the spectroscopic data, taken by the group in Vienna, was completed and is described in the section Observations and data reduction.

The French group has targeted 506 galaxies in total (see Table 5.1). Of them, 389 galaxies do not show emission lines. In these quiescent galaxies, the spectroscopic redshifts were derived from absorption lines. Two thirds of the galaxies in this group are members of the Abell 2163 cluster. Of the 117 galaxies with detected emission lines, only 38 galaxies are cluster members. Indicating, only 11% of the cluster galaxy

Maurogordato spectra	total	Quiescent galaxies	EL-galaxies	% of EL
Total galaxy spectra	506	389	117	
Abell 2163 members	331	293	38	11.5 %
Non-cluster members	175	96	79	45 %

Table 5.1: Galaxies observed by the French group

Ziegler spectra	total (Quiescent galaxies)	EL-galaxies	Spectra usable for RC
Total galaxy spectra	74 (41)	33	23
Abell 2163 members		19	13
Non-cluster members		14	10

Table 5.2: Galaxies observed by the Vienna group

targets show emission lines, whereas for non-member targets this is almost 50 % .

This observation does not deviate from the expected as the cluster population is dominated by spheroidal and "S0"-Type quiescent galaxies.

Nevertheless, the number of star forming galaxies in Abell 2163 is half of the expected star forming galaxy fraction usually found in multicomponent clusters (Cohen et al. (2014)), this value should be approximately 23%.

This lower value may be indicative of he hierarchical build-up scenario, in which galaxies first evolve in groups and sub-clusters before becoming gravitationally bound to a massive cluster. Once this occurs it then becomes susceptible to to the effect of environmental quenching - strangulation and Ram Pressure Stripping - due to a higher intracluster gas density. It is necessary to emphasise, that these results have not been corrected for completeness, but the large number of cluster members observed should be sufficiently representative of the cluster population.

The Vienna group has observed 74 galaxies (see Table 5.2). The fraction of emission line galaxies is higher than those selected by the French group by selection. Most of the star forming galaxies observed are cluster members. Since the cold gas content in cluster members is, in general, lower than in non-cluster galaxies, the intensity of their emission lines is weaker. As a result, several emission lines were rejected for the rotation curve extraction.

Fig:5.1 and Table: 5.3 shows the final sample of galaxies with emission lines, where the
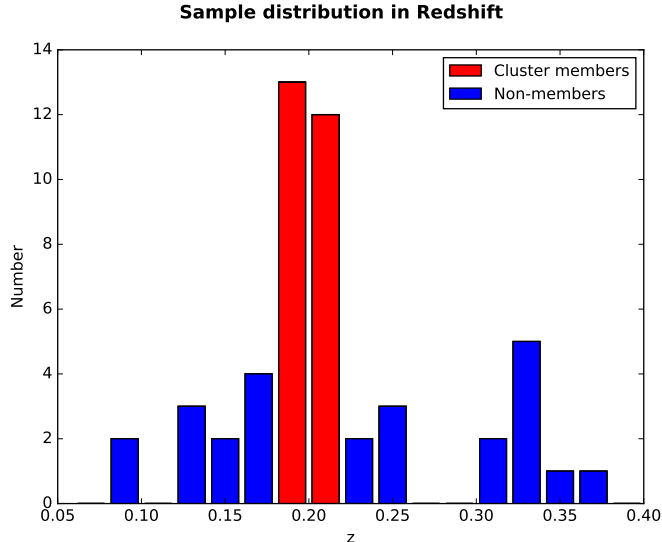
Figure 5.1: Galaxy sample distribution in redshift within bins of z=0.2.

intensity of at least one line is strong enough to extract rotation curves. The sample is composed of 50 galaxies distributed in a wavelength domain ranging from z=0.08 to z=0.37. Following the criteria of Maurogordato et al. (2008), Abell 2163 members were selected within a wavelength from z=0.18 to z=0.22. Half of the galaxies in the sample are cluster members, whereas the balance are classified as non-members. Of the last group, 10 galaxies have lower redshift than the cluster and 15 are background galaxies. Non-members include field galaxies, group members, pairs and mergers.

The mean redshift error calculated from the standard deviation of all measured emission lines of each galaxy gives a value of 0.00021 which corresponds to an error of 51.8 Km s^{-1} in the rest-frame velocity at z=0.2, the redshift of the Abell 2163 cluster.

5.2   Morphological classification of regular galaxies

Galaxies can be classified in the Hubble classification scheme when the fraction of light coming from the bulge to the total light of the galaxy is resolved. The sersic profile is most commonly used in the literature to model the brightness distribution in galaxies. Compact sources such as bulges and ellipticals are well modelled with a sersic index n=4, whereas the disk component is well described by an exponential profile with sersic index n=1. The extraction of morphological parameters of galaxies with a regular morphology was trivial and performed using *GALFIT* (Peng et al. (2010a)), however this was not the case for those classified as irregular. The lack of definition between the bulge and disk being the source of the uncertainty.

Galaxies classified	as **regular** and	**regular/irregular**	Galaxies	classified as	**irregular**
Galaxy ID	**RA**	**Dec**	**Galaxy ID**	**Ra**	**Dec**
Q1 8-1	16 15 48.44	-6 07 36.32	2011 Q1 9	16 15 45.01	-6 11 47.02
Q1 11-6	16 15 50.29	-6 09 54.09	w8 Q1 15	16 15 49.31	-6 18 01.35
Q1 16-11	16 15 59.05	-6 12 13.91	w8 Q1 17	16 15 54.81	-6 14 9.81
Q1 17	16 15 58.08	-6 13 18.76	w8 Q1 25	16 15 54.40	-6 16 48.85
Q1 w8 7	16 15 49.31	-6 18 01.35	w8 Q1 26	16 15 54.63	-6 16 54.58
Q1 w16 4	16 15 47.44	-6 08 02.68	2011 Q2 5u	16 15 57.31	-6 01 01.17
Q2 10u-3u	16 15 41.75	-5 59 30.13	w1 Q2 1	16 15 46.06	-5 56 57.99
Q2 10d 12 k	16 15 41.55	-5 59 25.47	w1 Q2 7	16 16 02.88	-5 59 45.20
Q2 13d-5	16 15 56.91	-6 00 52.902	w1 Q2 21	16 15 41.62	-5 58 18.98
Q2 18	16 15 57.10	-6 03 17.11	2010 Q3 11	16 15 12.00	-6 00 20.05
Q2 20	16 16 10.17	-6 04 31.45	2011 Q3 14	16 15 20.57	-6 03 22.97
Q2 w1 14	16 15 43.93	-6 01 20.753	2011 Q3 16	16 15 15.33	-6 05 01.21
Q2 w1 19	16 15 42.35	-5 57 59.30	w2 Q3 4	16 15 20.15	-6 00 01.40
Q3 10-8	16 15 11.80	-5 59 29.29	w10 Q3 26	16 15 23.72	-6 08 05.37
Q3 12-10	16 15 18.62	-6 00 52.26	w M1 Q3 7	16 15 00.83	-6 07 02.05
Q3 w10 11	16 15 09.85	-6 06 49.11	w M1 Q3 16	16 15 12.46	-6 07 45.11
Q3 w M1 14	16 15 15.83	-6 11 03.43	2011 Q4 5	16 15 16.56	-6 08 06.28
Q3 w M1 19	16 15 12.40	-6 07 25.22	2011 Q4 6	16 15 22.86	-6 8 43.58
Q4 10	16 15 21.70	-6 10 04.68	2010 Q4 8	16 15 24.38	-6 09 03.60
Q4 w3 32	16 15 05.46	-6 09 24.19	2010 Q4 9	16 15 15.60	-6 09 42.19
Q4 w3 33	16 14 54.11	-6 06 08.39	2011 Q4 10	16 15 19.77	-6 10 53.04
Q4 w M1 6	16 15 04.02	-6 15 46.94	2011 Q4 11	16 15 9.12	-6 11 13.92
Q4 w M1 13	16 15 03.63	-6 20 15.16	w3 Q4 22	16 15 17.85	-6 12 08.88
			w11 Q4 18	16 15 26.16	-6 18 01.01
			w M1 Q4 3	16 14 58.61	-6 14 34.49
			w M1 Q4 11	16 15 13.17	-6 18 46.691
			w3_Q4_9	16 15 16.44	-6 08 06.18

Table 5.3: Position in RA and Dec of the galaxies of the sample.

The Hubble type of a galaxy was classified using the bulge to total light ratio (Flux Bulge/ (Flux Bulge + Flux Disk)) following the classification as described in Simien and de Vaucouleurs (1986). (see Table 5.4).

Galaxy Type	Ellipticals (E)	S0	Sa	Sab	Sb	Sbc	Sc	Scd	Sd
(B/T)	~ 1	0.57	0.41	0.32	0.24	0.17	0.094	0.058	0.022

Table 5.4: Hubble classification from the bulge to total light ratios of local galaxy types.

The fig:5.2 shows the Hubble type distribution of the sample of galaxies with regular morphology. In total 22 galaxies were classified. A single galaxy from the sub-sample of regular galaxies did not have have photometric data. More than half of the galaxies are cluster members. This result is not surprising as the selection criteria of the Vienna group aimed to study the environmental effects on galaxy evolution. Therefore, the majority of non-member galaxies show disrupted morphology as well as irregular kinematics.
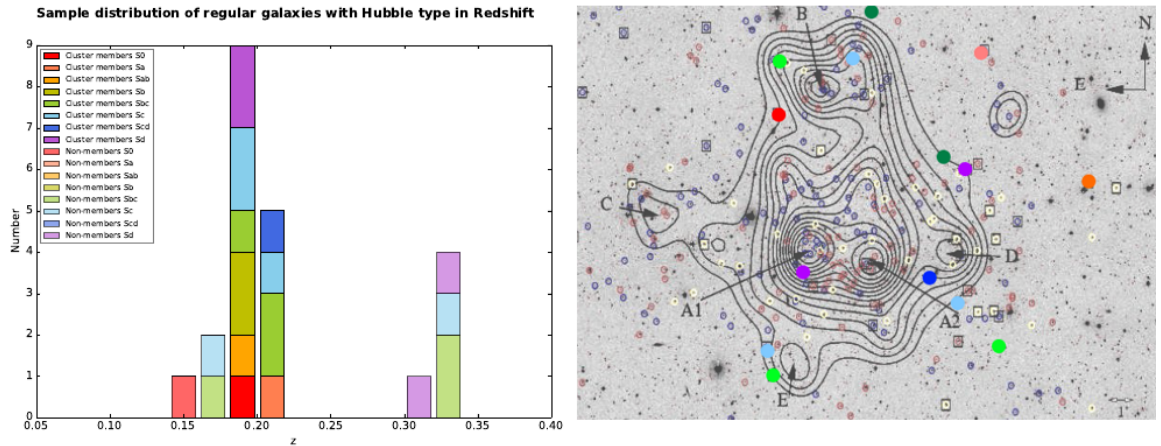

Figure 5.2: Left: Sample distribution of regular galaxies in Hubble type in in redshift bins of z=0.2. Brightest colours show the cluster galaxies and pastel colours show the non-members. Different colours show galaxies classified into the different Hubble types. Right: Same figure as Fig:2.4. Cluster members with Hubble type in colours projected on the sky. The colour code is the same as in the histogram of the figure on the left.

From the morphology-density relation (Dressler (1980)), an increase in passive galaxies and a decrease in star forming disk galaxies with increasing galaxy density is expected. Thus, galaxy clusters have a larger population of "S0"-Type and spheroidal galaxies than the field galaxy population. This relation evolves with time and is related to the evolution of the merger rate and also to the fraction of star forming blue galaxies

(Butcher-Oemler effect). Therefore, clusters at higher redshift have a larger population of star forming disk galaxies.

In comparison to local galaxies, when at the redshift of Abell 2163 the population of S0 Galaxies decreases slightly in favour of the disk galaxy population while the number of ellipticals remains constant. Around half of the galaxy population in a compact cluster might be an **S0**-Type galaxy, whereas 30% of cluster members might be **spiral** galaxies and 20% **ellipticals** (Dressler et al. (1997)). However, these relative population numbers of passive galaxies and their distribution in the cluster depends on the local density of galaxies (Houghton (2015)). This may be not the case for disk galaxies. In Abell 2163, as described before, the population of quiescent galaxies - ellipticals and the majority of S0 galaxies - is about 90% of the galaxy cluster population. These results may be the consequence of two factors. Firstly could be a hierarchical build-up scenario, where this massive cluster has grown through accretion of small sub-clusters and groups. That implies that the galaxies were altered before or during the accretion of their structure to the cluster. Secondly, the high density in the ICM may be responsible for having already quenched star forming disc galaxies as they fall into the centre of the cluster potential.

In the star forming cluster population with regular morphology only one **S0**-Type galaxy was identified in the outskirts of the in-falling Sub-Cluster B (fig:5.2) and 13 spiral galaxies were found to be distributed around the entire cluster. The distribution of the spiral galaxies does not show any correlation with their distance to the centre of the cluster. Since late-type spirals (**Sc**, **Sd**) are gas rich, they are expected to be located in the outskirts of the cluster. Here their interstellar gas will not have been affected by ram pressure stripping. Their apparent location close to the centre of the cluster may be due to projection effects.

The Hubble Type of non-cluster members are as follow: 1 **S0**, 3 **Sbc**, 2 **Sc**, and 2 **Sd**.

5.3 Regular and irregular galaxies in the sample

The observed spectra cover the wavelength range from emission lines [OII]$\lambda3727/3729$ doublet, Hβ, [OIII]$\lambda4959$ and [OIII]$\lambda5007$ in almost all galaxies. For the closest galaxies, only the the last 3 emission lines are obtained and for the galaxies with the highest redshift of the sample only the [OII] doublet is obtained.

Line of sight velocities for all detected emission lines were extracted as described in the section **Kinematics extractions** of Chapter 4. A few galaxies, like the galaxy shown in fig: 5.3, exhibit high intensities in all detected emission lines. In general, the

most prominent emission lines were the [OII] doublet, Hβ and the [OIII]$\lambda 5007$. When many options for extraction presented themselves, the rotation curve with the lowest uncertainty was chosen. This usually corresponded to the curve which extended the farthest.
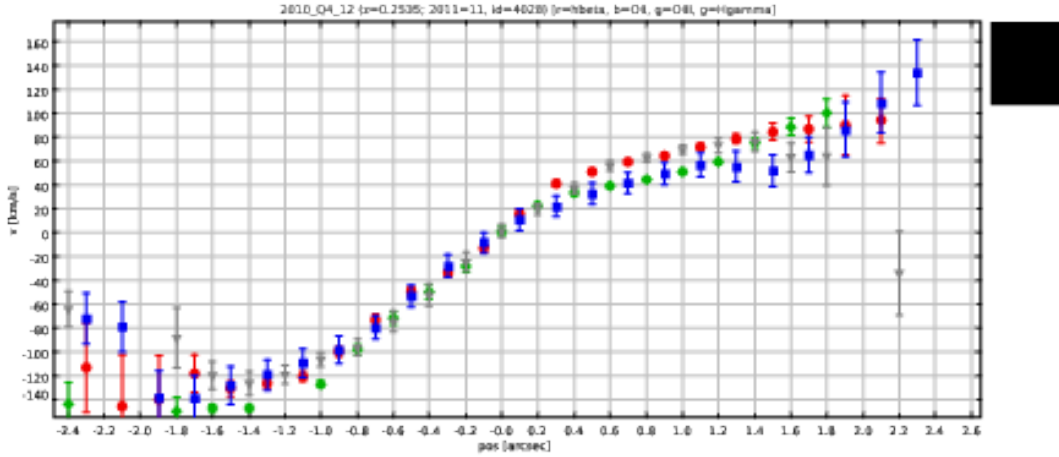

Figure 5.3: Extracted line of sight rotation curves of a galaxy with intense emission lines. Here, the colours red, blue, green and grey show the line of sight rotation curve extracted from the lines Hβ, [OII], [OIII] and Hγ respectively)

After a rough inspection, the extracted rotation curves were classified as regular or irregular following the criteria of symmetry in the receding and approaching side of the rotation curve and a regular morphology. Irregularities in the gas component are found in galaxies affected by all interaction processes. Strong gravitational interactions can change the visual appearance of galaxies. A description of the influence of interaction processes on the kinematics and morphology of galaxies is given in Section **morpho-kinematic classification of distorted galaxies**. Hence, galaxies in dynamical equilibrium show regular rotation curves and morphology.

In this thesis, the galaxy sample was divided in two sub-samples. Galaxies showing distortion in their kinematics and/or morphology were classified as irregular. Otherwise, they were classified as regular galaxies. In some galaxies a subtle distortion in their kinematics or morphology was observed. In these cases, it was not apparent if these galaxies were regular or not, since resolution effects at the galaxy redshifts may play an important role in revealing the dynamical state of galaxies (Kronberger et al. (2007)). These galaxies were classified as "regular/irregular" and were included in both sub-samples.

Fig: 5.16 shows the distribution of regular and irregular galaxies as a function of

redshift. 17 galaxies are classified as regular, 12 of them are cluster members and 5 are non-members. Most of the 27 galaxies classified as irregular are non-cluster member galaxies. Thus, 17 irregulars are non-members versus 10 irregular cluster members. Six galaxies were classified as "regular/irregular", three from cluster members and three non-members. The high number of irregular non-member galaxies is mostly due to the selection criteria as previously explained (see 5.1.

The right of Fig.5.16 shows the projected spatial distribution of regular and irregular cluster members in the cluster. Regular galaxies that are close to the cluster centre A1 and Sub-cluster B might be due to projection effects as they are late type spirals. With the exception of the **S0** galaxy on the east part of the Sub-Cluster B (see fig: fig:5.2). One galaxy classified as regular/irregular is located close to the in-falling group D and cluster centre A2. Its position relative to the cluster centre suggests that the possible distortion might be due to interaction with the ICM. The two remaining galaxies are located at the edges of the cluster, if these display irregularities they may be due to gravitational interactions with surrounding galaxies. The effect of the intracluster medium of the rich cluster Abell 2163 is very clear in the distribution of irregular galaxies. Their location relative to the cluster centre, Sub-Cluster B centre and in-falling group D centre suggests the effect of ram pressure stripping acting on these star forming galaxies as they fall into the cluster centre with high velocities in a high density medium. Nevertheless, four irregular cluster members are located outside the high galaxy density region - inside the contours - (three galaxies are located in the north, outside of Fig 5.16). These galaxies are not affected by the surrounding gas, but gravitational interactions may be responsible for the distortion of their dynamics.

5.4   The sub-sample of regular galaxies

5.4.1   Simulated rotation curves

The extracted line of sight rotation curves were corrected for geometric and observational effects following the method described in Section **rotation curve simulations** of Chapter 4. For each galaxy, a customised model with the structural parameters of the observed galaxy and with an exponential intensity profile was created. An intrinsic RMS was introduced due to seeing conditions. For this purpose, the intensity profile and later the velocity field was convolved with a PSF that was adjusted to the seeing condition during the night of the observations. The measured seeing (FWHM) was $\sim 0".8$ for the Vienna group's observations. To match the observations, a customised long slit with same width and position angle to the galaxy major axis as the
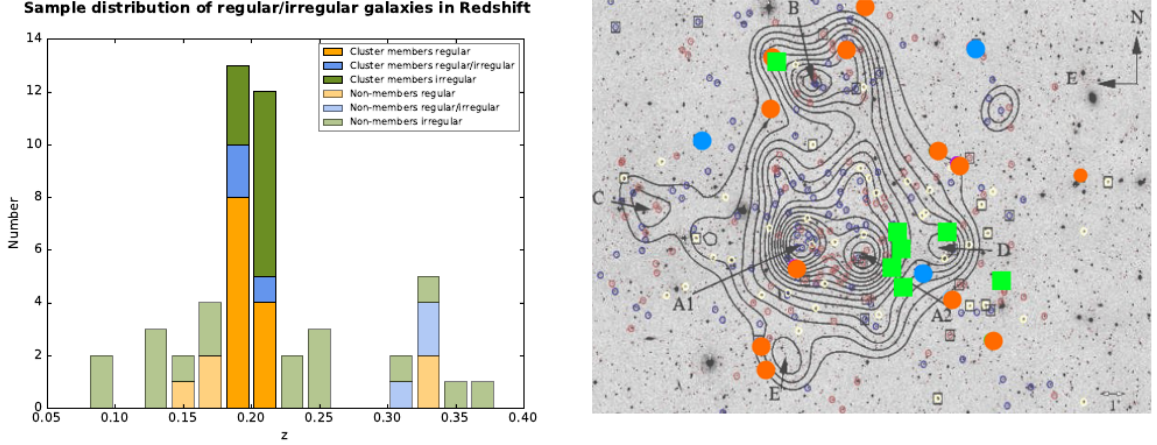
Figure 5.4: Left: Sample distribution of regular and irregular galaxies in redshift bins of z=0.2. Brightest colours show the cluster galaxies and pastel colours show the non-members. Galaxies classified as regular, irregular and regular/irregular are displayed in orange, green and blue respectively. Right: Same figure as Fig:2.4. The filled rectangles in green show irregular (kinematics and/or morphology) cluster members as projected on the sky while the filled circles in orange show the position of the regular cluster members. Galaxies with no clear signature of distortion in their kinematics or morphology are shown with blue filled circles

observation was placed on the intensity profile to create a synthetic spectra. Next, intensity-weighted rotation velocity values along the galaxy major axis were derived (see Bösch et al. (2013b)). This rotation velocity is defined as synthetic rotation curve. Matching the synthetic rotation curve with the observed line of sight rotation curve allows the determination the true intrinsic rotation curve parameters.
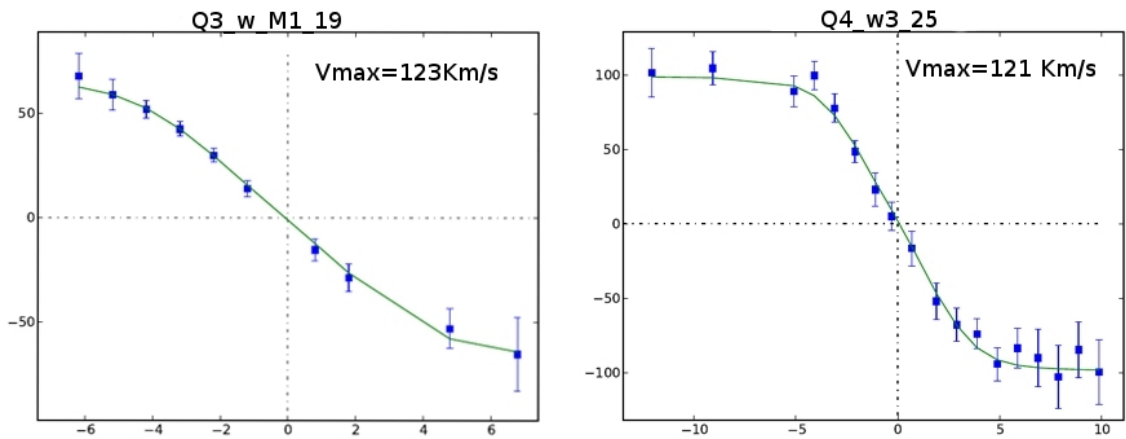

Figure 5.5: Observed (blue squares) and simulated (green line) rotation curve from the same galaxy but with different position angle.

A number of galaxies were observed by both the French and the Vienna group but with

43

different slit positions. These galaxies were used to test the robustness of the extraction and simulation processes used in this work. The Fig. 5.5 shows the extracted (blue squares with error bars) line of sight rotation curve and the simulated (green line) rotation curve of the same galaxy observed with different slit position angles. The average difference in the intrinsic rotation curve is 5 Kms^{-1}. This difference is minimal when considering that in some galaxies the extracted line of sight rotation velocities do not reach the maximum velocity, e.g. Fig 5.5 on the left. Thus, the method applied here provides confidence in the derived intrinsic velocity.

Figures 5.6, 5.7, 5.8 and 5.9 show the observed and intrinsic rotation curves of the regular sub-sample in blue squares and green lines respectively. In six galaxies the line intensity rapidly becomes too weak, resulting in the signal to noise ratio, at large radii, being insufficient to extract the rotation velocity of the constant velocity region. Those galaxies are shown with an orange filled dot on the top, otherwise the colour of the dot is blue. From the galaxies classified as "regular/irregular", in three cases, the observed rotation curves show subtle distortions. They are displayed as orange rectangles, otherwise blue. Cluster members are displayed with a yellow star.

5.4.2 Kinematic properties

The galaxy properties used in the next relations are calculated as follows.

The output parameters of the simulation are the maximum intrinsic rotation velocity (V_{max}) and the turn over radius (r_t). The scale length radius (r_d) was calculated from the effective radius (r_{eff}) as follows $r_d = r_{eff}/1.7$. For this purpose, the effective radius of the *GALFIT* fit was used.

During this thesis, a K-Band image was used to derive the absolute magnitudes and stellar masses of the galaxies. The structural parameters of this image was performed with *SEXTRACTOR*. Using the intensities measured with *SEXTRACTOR*, the absolute magnitudes (M_K) was calculated as follows:

$$M_K = m_K - DM - A_\lambda \qquad (5.1)$$

Where DM is the distance modulus at the galaxy's redshift, and A_λ is the galactic extinction in K-Band at the position of Abell 2163 on the sky, which is 0.1. For the absolute magnitude, the k-correction was not applied. Here the Vega magnitude is used.

The stellar masses are calculated from the luminosity and a Mass to light ratio (M/L)
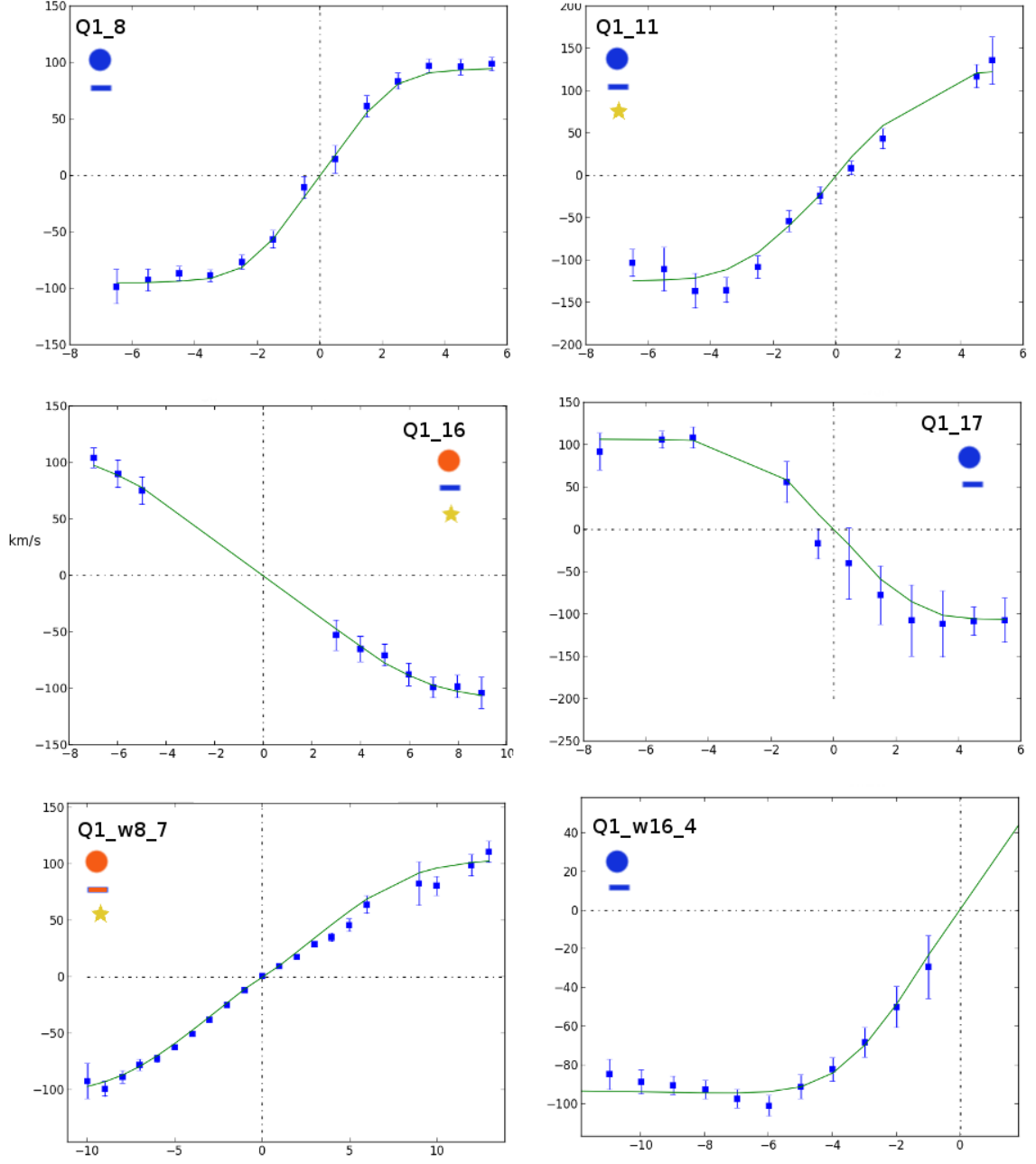
Figure 5.6: Results of the extracted and simulated rotation curves of the regular sub-sample of galaxies. Here, the observed and synthetic rotation curve are shown in blue squares and green line respectively. On the top of each diagram the capitalised galaxy ID is shown. Below, blue and orange colour of the filled dots show the rotation velocities where V_{max} either has been reached or not respectively. Below, the orange rectangles represent the cases where the extracted or simulated rotation curves were classified as low quality (LQ), the blue rectangles indicate rotation curves with high quality (HQ). The yellow star indicates cluster membership.
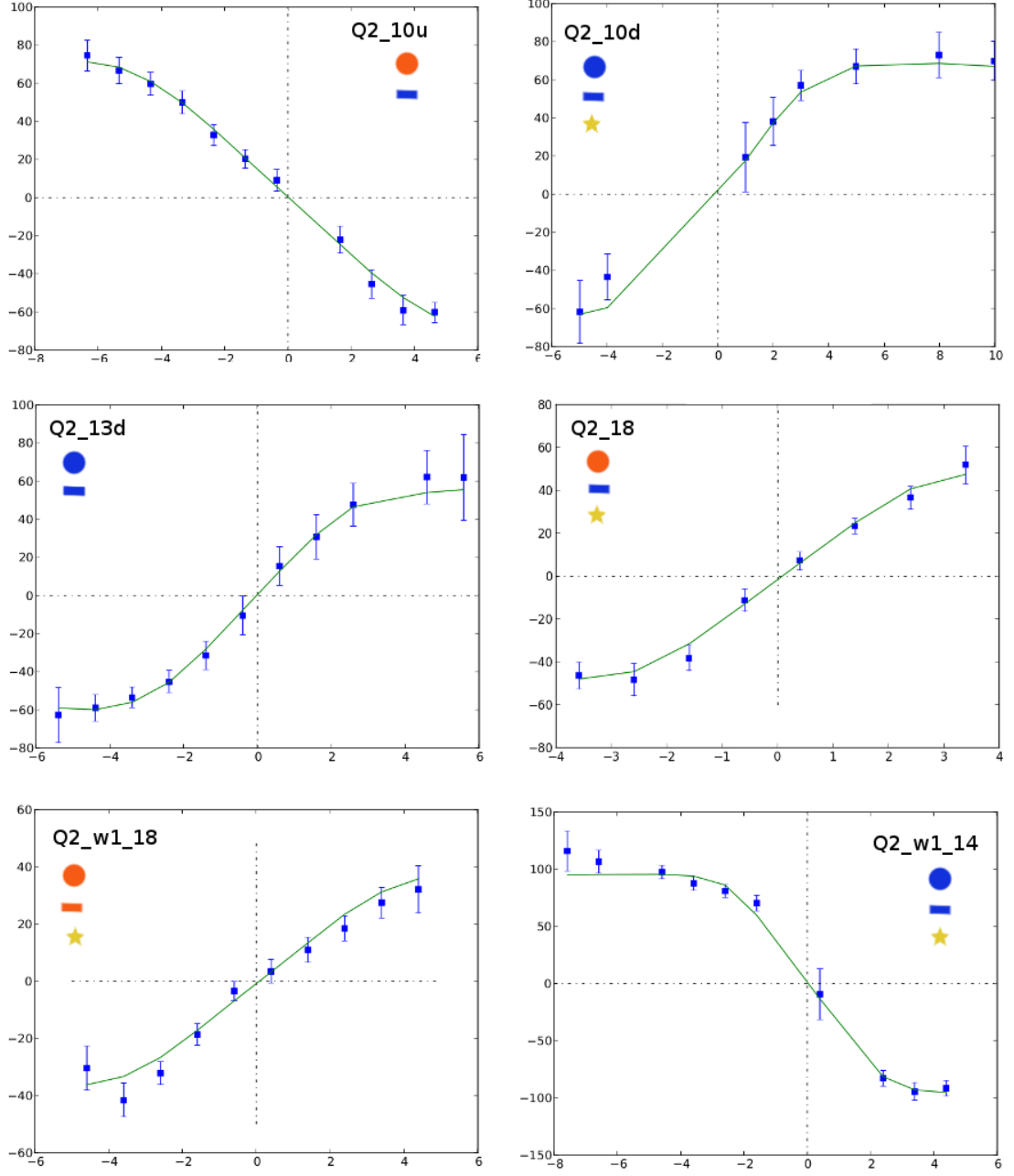
Figure 5.7: Results of the extracted and simulated rotation curves of the regular sub-sample of galaxies. Here, the observed and synthetic rotation curve are shown in blue squares and green line respectively. On the top of each diagram the capitalised galaxy ID is shown. Below, blue and orange colour of the filled dots show the rotation velocities where V_{max} either has been reached or not been reached respectively. Below, the orange rectangles represent the cases where the extracted or simulated rotation curves were classified as low quality (LQ), the blue rectangles indicate rotation curves with high quality (HQ). The yellow star indicates cluster membership.
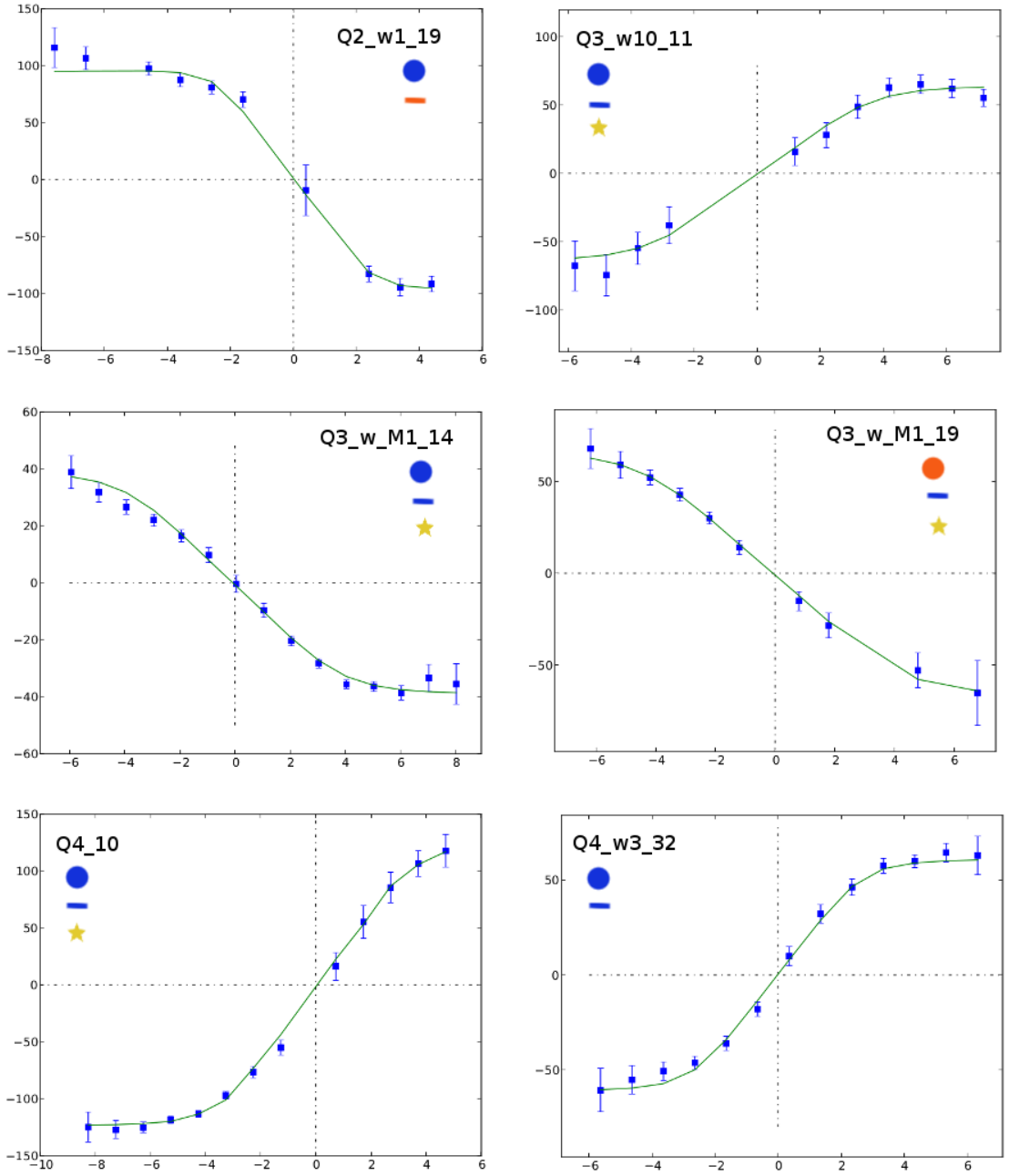
46

Figure 5.8: Results of the extracted and simulated rotation curves of the regular sub-sample of galaxies. Here, the observed and synthetic rotation curve are shown in blue squares and green line respectively. On the top of each diagram the capitalised galaxy ID is shown. Below, blue and orange colour of the filled dots show the rotation velocities where V_{max} either has been reached or not been reached respectively. Below, the orange rectangles represent the cases where the extracted or simulated rotation curves were classified as low quality (LQ), the blue rectangles indicate rotation curves with high quality (HQ). The yellow star indicates cluster membership.
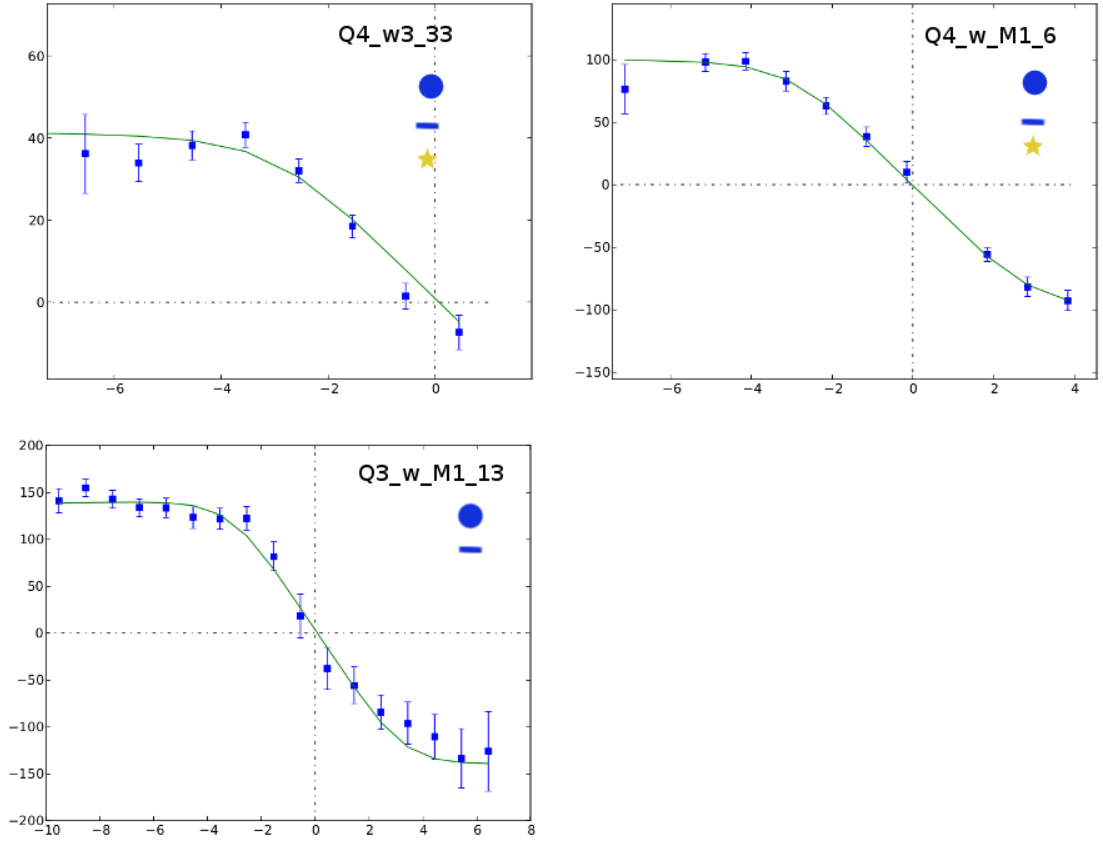
Figure 5.9: Results of the extracted and simulated rotation curves of the regular sub-sample of galaxies. Here, the observed and synthetic rotation curve are shown in blue squares and green line respectively. On the top of each diagram the capitalised galaxy ID is shown. Below, blue and orange colour of the filled dots show the rotation velocities where V_{max} either has been reached or where it has not been reached respectively. Below, the orange rectangles represent the cases where the extracted or simulated rotation curves were classified as low quality (LQ), the blue rectangles indicate rotation curves with high quality (HQ). The yellow star indicates cluster membership.

conversion factor as follows:

$$L = 10^{-0.4(M_K - M_{sun})} \qquad (5.2)$$

$$M_* = L * \left(\frac{M}{L}\right) \qquad (5.3)$$

The absolute magnitude M_{sun} in K-Band observed in Vega magnitude is 2.794. The conversion factor (M/L) range between 0.55 and 0.77 and depends on the stellar population of the galaxies. Here, the stellar masses were taken from the median of the previous results and the smallest and the greatest value were used as the lower and upper limits.

Finally, the dynamical mass was calculated as follows:

$$M_{dyn} \simeq \frac{V_{rot}^2 \cdot r_d}{G} \qquad (5.4)$$

Here, G is the gravitational constant (G=0.004302 [pc (km/s) $M_\odot^{-1}$]). To compute the upper and lower limits, different scale length and velocities were used. Since the scale length and inclination results of *SEXTRACTOR* and *GALFIT* are slightly different, the simulation of the rotation curves were performed again for each variation. Additionally, a rotation velocity was calculated using the scale length from the 2-component fitting. Finally, the smallest and greatest value of the calculated M_{dyn} were taken as the lower and upper limits. It is necessary to highlight that the rotation velocities uncertainties are likely underestimated. Therefore the uncertainties calculated on the dynamical mass are lower than the upper and lower limits.

The tables 5.5 and 5.6 show the results of the kinematic properties for the sub-sample of regular galaxies.

Galaxy ID	z	r_d [Kpc]	M_K * [mag]	V_{max} [Km/s]	V_{max}_err [Km/s]	$\log(M_*)$ [$M_\odot$]	lower limit $\log(M_*)$ [$M_\odot$]	upper limit $\log(M_*)$ [$M_\odot$]
Q1_8-1	0.334	3.50	-23.84	134.8	6.5	10.49	10.32	10.54
Q1_11-6	0.199	2.35	-24.05	203.5	14.6	10.58	10.41	10.63
Q1_16-11	0.198	2.92	-23.41	186.8	9.0	10.32	10.15	10.37
Q1_17	0.166	1.83	-22.62	109.3	5.0	10.01	9.84	10.06
Q1_w8_7	0.196	1.56	-23.73	177.0	16.8	10.45	10.28	10.50
Q1_w16_4	0.332	1.91	0	103.7	2.5	0	0	0
Q2_10u-3u	0.302	3.75	-23.85	129.5	8.5	10.50	10.33	10.55
Q2_10d_12_kl	0.198	2.05	-20.99	85.1	3.7	9.35	9.18	9.40
Q2_13d-5	0.213	1.52	-23.58	122.3	4.6	10.39	10.22	10.44
Q2_18	0.193	1.82	-24.20	92.0	8.0	10.64	10.46	10.68
Q2_20	0.192	1.96	-23.75	178.4	21.5	10.46	10.29	10.51
Q2_w1_14	0.204	2.62	-24.40	159.8	8.9	10.72	10.55	10.77
Q2_w1_19	0.336	4.95	-23.42	155.4	22.1	10.33	10.16	10.38
Q3_10-8	0.155	0.97	-20.38	103.2	25.1	9.11	8.94	9.16
Q3_12-10	0.194	1.79	-23.30	126.6	31.1	10.28	10.11	10.33
Q3_w10_11	0.197	2.35	-23.83	138.6	5.8	10.49	10.32	10.54
Q3_w_M1_14	0.199	2.02	-22.28	77.2	3.6	9.87	9.70	9.92
Q3_w_M1_19	0.197	2.45	-22.39	123.3	4.4	9.91	9.74	9.96
Q4_10	0.203	2.55	-23.84	198.8	10.58	10.49	10.32	10.54
Q4_w3_32	0.165	1.41	-21.14	79.9	2.8	9.418	9.24	9.46
Q4_w3_33	0.212	1.96	-24.01	154.9	3.6	10.56	10.33	10.61
Q4_w_M1_6	0.209	1.33	-22.59	125.0	3.7	9.99	9.82	10.04
Q4_w_M1_13	0.335	3.39	-24.91	162.5	5.4	10.92	10.75	10.97

* M_K errors range from 0.007 to 0.06 [mag].

Table 5.5: Derived parameters of the sub-sample of regular galaxies.

5.5 Tully-Fisher relation

In virial equilibrium, the rotation velocity traces the distribution of the total mass, baryonic and dark matter mass, of the system. Usually its shape is characterised by a steeply rising inner part and flattens in the outer part. Mostly the maximum rotation velocity lies in the transition part, except for galaxies that lack of the flattened part, and galaxies with the lowest fraction of baryonic matter. On the other hand, the luminosity is connected only with the baryonic matter, more precisely with the stellar component of the baryonic matter. Active galactic nuclei (AGN), which can contribute to a higher fraction of the observed light were rejected in this study. Both parame-

Galaxy ID	z	log(M_{dyn}) [$M_\odot$]	lower limit log(M_{dyn}) [$M_\odot$]	upper limit log(M_{dyn}) [$M_\odot$]	M_*/M_{dyn}	Hubble Type
Q1_8-1	0.334	10.62	10.30	10.99	0.74	Sc
Q1_11-6	0.199	10.73	10.52	11.11	0.70	Sd
Q1_16-11	0.198	10.83	10.65	11.10	0.31	Sc
Q1_17	0.166	10.41	10.23	10.65	0.39	Sc
Q1_w8_7	0.196	10.53	10.32	10.75	0.84	Sbc
Q1_w16_4	0.332	10.22	10.07	10.39	0	Sbc
Q2_10u-3u	0.302	10.58	10.36	10.78	0.83	Sd
Q2_10d_12_kl	0.198	9.93	9.74	10.26	0.26	Sb
Q2_13d-5	0.213	10.18	9.96	10.47	1.62	Sbc
Q2_18	0.193	10.08	9.73	10.33	3.61	S0
Q2_20	0.192	10.61	10.41	10.84	0.70	-
Q2_w1_14	0.204	10.79	10.58	10.98	0.84	Sc
Q2_w1_19	0.336	11.00	10.69	11.16	0.21	Sd
Q3_10-8	0.155	9.87	9.47	10.20	0.17	S0
Q3_12-10	0.194	10.36	10.20	10.54	0.82	Sab
Q3_w10_11	0.197	10.52	10.34	10.72	0.92	Sb
Q3_w_M1_14	0.199	10.06	9.92	10.21	0.64	Sc
Q3_w_M1_19	0.197	10.41	11.23	10.66	0.31	Sd
Q4_10	0.203	10.58	10.42	10.77	0.32	Scd
Q4_w3_32	0.165	9.81	9.50	10.13	0.39	Sbc
Q4_w3_33	0.212	10.64	10.49	10.80	0.83	Sa
Q4_w_M1_6	0.209	10.18	10.21	10.33	0.52	Sbc
Q4_w_M1_13	0.335	10.92	10.79	11.06	1.00	Sbc

Table 5.6: Derived parameters of the sub-sample of regular galaxies.

ters, the rotation velocity and the luminosity of galaxies are linked together by the Tully-Fisher relation. Therefore, the Tully-Fisher relation provides the link between baryonic and dark matter content in galaxies. Studying the matter content in different environments and at different redshifts provides valuable information on evolution of galaxies. In the past, the Tully-Fisher relation has been used as indirect distance indicator (Tully and Fisher (1977)), but its precision is sensitive to irregularities in the dynamics of the system.

The evolution of the time dependent Tully-Fisher relation is still not well understood. Several studies (Böhm et al. (2004),Bamford et al. (2006),Vogt et al. (1996)) show a luminosity evolution from local galaxies to galaxies at intermediate redshift (until

z=1). That is, as redshift increases, galaxies become brighter. The main driving power might be the evolution of the star formation activity in spiral galaxies. This evolution may be mass-dependent and is stronger for low-mass galaxies(Böhm et al. (2004)). Stacking the rotation curves of galaxies with a redshift from z∼0.6 to z∼2.6 Lang et al. (2003) shows a fall-off of the outer part of the curve, this contrasts with local galaxies and indicates a larger fraction of baryonic to dark matter within the disk scale. Übler et al. (2017) investigated the evolution of the Tully-Fisher relation from z∼0.9 to z∼2.3 and found an evolution in the baryonic matter content in galaxies at z∼2.3 with similar stellar masses compared with the galaxies at z∼0.9.

Studies on the Tully-Fisher relation in different environments are still under discussion. Bösch et al. (2013b),Ziegler et al. (2003),Nakamura et al. (2006) show no strong differences between cluster and field galaxies, but the later are in general slightly brighter in their luminosities at fixed rotation velocity. In contrast, other authors (Milvang-Jensen et al. (2003),Bamford et al. (2005)) found greater luminosities in cluster galaxies than in field galaxies. These contradictory results may be explained due to biases towards sample selections, methods and misclassification of disturbed galaxies as virialised systems. Despite these disagreements, all mentioned authors agree that cluster galaxies are redder in colours than field galaxies and that the fraction of star forming disk galaxies is higher in the field population.

Irregular galaxies are very populous in dense environments. In those systems, the rotation velocity does not trace the total mass of the system. Additionally, galaxy interaction processes and environmental effects trigger starburst episodes which can increase the luminosity in galaxies (Kapferer et al. (2005, 2008, 2009)). Both parameters define the Tully-Fisher relation, so by including distorted systems in this relation induce an increment of the scatter. These systematic errors increase with redshift when at an intermediate redshift, since distortions are not well disentangled due to resolution effects. Irregularities are not always seen in long slit spectroscopy and can contribute to errors when misclassifying distorted galaxies as regular.

5.5.1 Comparison with the local TFR

Figure: 5.10 shows the Tully-Fisher relation of cluster and field galaxies of the subsample of regular galaxies. The maximum rotation velocity covers a range from 77 $Km \cdot s^{-1}$ to 203 $Km \cdot s^{-1}$ and the absolute magnitude in K-Band extends from $M_K \sim$ -20 mag to $M_K \sim$ -25 mag. The grey line corresponds to the best fit of the K-Band TFR for local galaxies (RC/FD Sample) from Verheijen (2001). It is defined by the following equation:

$$M_K = -10 \cdot log(V_{max}) - 1.9 \qquad (5.5)$$

The dashed lines show the region inside the estimated errors for the above mentioned slope. The slope of the TFR depends on the used passband and is steeper towards redder colours.

Almost all galaxies in this sample are located along the slope and inside the errors of the TFR of local galaxies (fig: 5.10). There is no clear trend in the luminosity evolution with redshift in this sample and in the local population of galaxies. Even less clear is the mass-dependent luminosity evolution in low-mass galaxies (lower rotation velocities). This might be explained mainly due to two factors: the small galaxy sample and environmental effects in cluster galaxies.

Tully-Fisher Relation
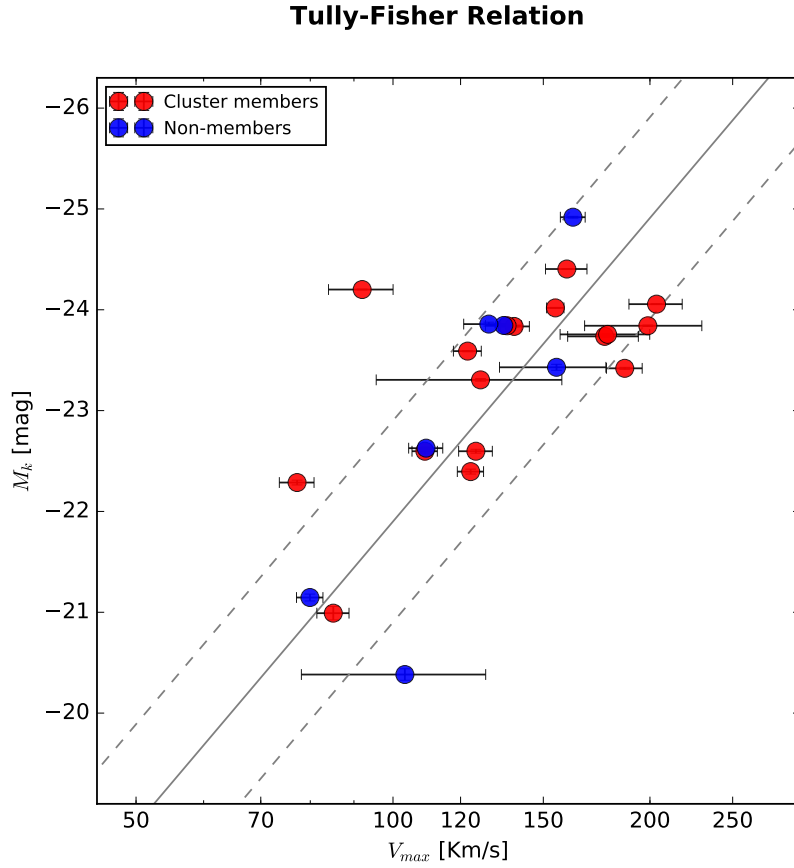
Figure 5.10: Tully-Fisher relation of cluster members and non-members. The grey line and dashed lines show the best-fit slope of the local TFR from Verheijen (2001) within 3 sigma errors.

5.5.2 Cluster members and non-members Tully-Fisher relation

When comparing the cluster and non-cluster population, the increased luminosity in field galaxies becomes clearer. The offset of the cluster and non-cluster population to the best-fit of the local TFR was quantified as the weighted mean. Were the weights of each value are inversely proportional to the square of its error. The expected luminosities M_{K0} were first calculated from the rotation velocities using the equation 5.5. Then, the difference of the measured luminosities and the expected luminosities (eq:5.6) provides the offset from the local TFR.

$$\Delta M_K = M_K - (-10 \cdot log(V_{max}) - 1.9) \qquad (5.6)$$

These offsets are ΔM_K(Abell)=-0.37 mag and ΔM_K(non-members)=-0.40 mag with scatters of $\sigma_{\Delta M_k}$(Abell)=0.59 mag and $\sigma_{\Delta M_k}$(non-members)=0.32 mag. There are no significant differences in the the offsets for cluster and non-cluster members. These results are in agreement with previous studies, e.g. (Bösch et al. (2013b),Ziegler et al. (2003),Nakamura et al. (2006)), which have found a weak enhancement in the luminosities of field galaxies compared to the cluster population. A large scatter of the cluster population is expected compared to the non-cluster galaxies, which originate mainly from distortions in the velocity field as previously explained. Nevertheless, the scatters calculated in this thesis for the cluster and non-cluster populations are ∼1.5 smaller than the scatter found by Böhm (2003) for their high-quality objects. One explanation could be the strict classification of regular galaxies not only based on the kinematics, but also on the morphology. These results suggest that the regular cluster members have not been strongly influenced by environmental effects. The smaller numbers of low mass galaxies may reduce the scatter in the low end considerably.

When fitting the slope of cluster and non-members galaxies (fig: 5.11), the slope of cluster members is more shallow (slope=-4.45, intercept=-13.84 for $log(V_{max})$) than the best-fit of the local TFR. In contrast the non-cluster population fit is quiet steep (slope=-30.68 intercept=43.70 for $log(V_{max})$). Here, the fit of non-cluster population is not representative for the non-cluster population due to the low number of galaxies in this sub-group, therefore it will not be discussed. Comparing the best-fit of the cluster population to the slope found by Ziegler et al. (2003) shows that they both are in agreement. On the contrary, Bamford et al. (2005) found a steeper slope of the cluster population with respect to the local sample. Moreover, the slope found here for the cluster population is in agreement with the slope found by Böhm (2003); Böhm et al. (2004) for galaxies at intermediate redshift. This result suggests a mass-

dependent enhancement of the luminosity in cluster members. Low mass galaxies show increased luminosities due to an enhancement of star formation activity induced by environmental effects or gravitational interactions. On the other hand, the cold gas fuel of star formation might be reduced significantly in massive star forming cluster members not only due to environmental quenching, but also due to mass quenching. In a work by Bösch et al. (2013b), were dusty red galaxies are thought to be the link between active and passive disk galaxies in cluster, it was found that dusty red galaxies are located preferentially below the best-fit line. These galaxies could either be red spirals or simply in process of quenching.
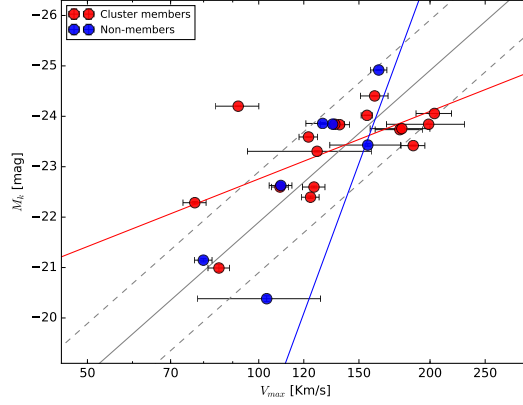
Figure 5.11: Same figure as the previous figure 5.10, but with the best-fit line of the cluster and non-members population in red and blue respectively. Blue fit of non-members is not representative for the non-cluster members due to the low number of galaxies.

5.5.3 Testing possible biases on the Tully-Fisher analysis

Figure 5.12 shows four potential affects that could introduce biases in the Tully-Fisher analysis. The first test consists of galaxies with rotation curves that do not reach the Turn-over radius (Fig 5.12 plot on the top, first column), therefore the V_{max} value might be underestimated. It is important to note that in the Figures 5.6, 5.7, 5.8, 5.9, these galaxies show an orange dot on the top. Five galaxies fulfil this criterion, but only one is far offset from the best-fit line and the reason for that is most likely due to an underestimation of the V_{max}. As previously mentioned, the simulation process applied here was found to be very robust and it can be safely assumed that the balance galaxies show reliable V_{max} results.

The second test consists of galaxies in which the simulations do not trace perfectly the extracted rotation curve (Fig 5.12 top plot, second column). Three galaxies fulfil this

criteria. All of them belong the local TFR. Therefore, it is suggested that this affect does not effect the result in the corresponding galaxies.

The third test comprises of galaxies that show slight distortions in their kinematics or morphologies (Fig 5.12 bottom plot). For Figures 5.6, 5.7, 5.8, 5.9 galaxies with slightly distorted kinematics are presented with an orange rectangle on the top. These galaxies are classified as regular/irregular and are part of the sub-samples of regular and irregular galaxies. Again, all galaxies follow the trend of their counterparts. Hence, there is no clear evidence of bias introduced by these effects.
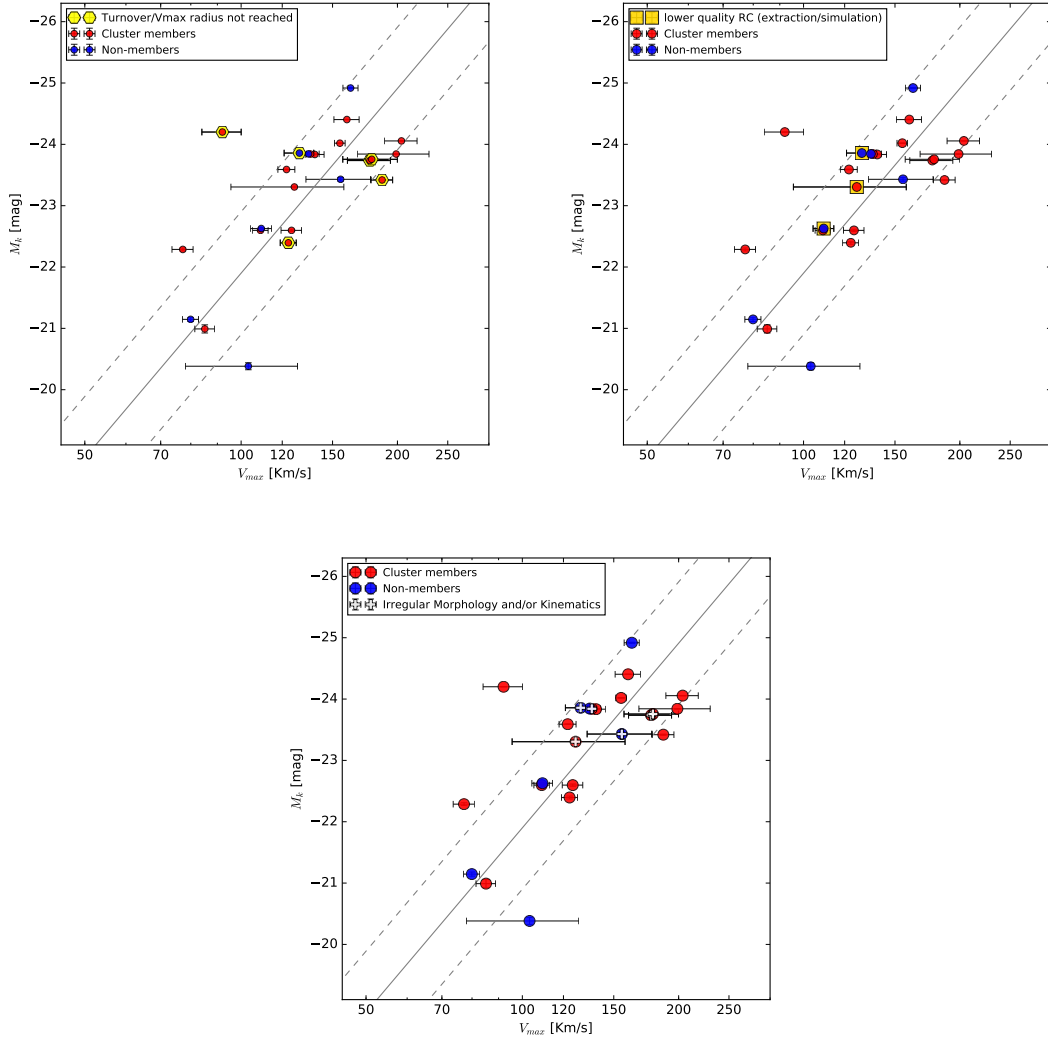
Figure 5.12: Testing possible bias on the K-Band Tully-Fisher relation. On the top: first column, highlighted are galaxies with rotation curves that have not reached their flat region. Second column, highlighted are galaxies where the simulation does not trace exactly the extracted rotation curves. On the bottom, highlighted are galaxies classified as regular/irregular.

56

After the tests that have been performed, only one galaxy was found with an under-estimated V_{max}. This is the cluster member on the left side of the best-fit slope. The non-member galaxy with a higher offset in the lower end of the Tully-Fisher is not effected by any affects. Therefore it is unclear if there is some processes acting on this galaxy that result in these lower luminosities.

5.5.4   Dynamical Mass

The calculated dynamical masses, stellar masses as well as the fraction of stellar mass to dynamical mass of the galaxies are presented in Tables 5.5 and 5.6. The dynamical masses cover the range from $10^{9.81}$ to 10^{11}. Four galaxies of the non-cluster members are dark matter dominated, these represent the 57% of this sub-group. For one galaxy of the non-member galaxies the stellar mass information is unavailable. From the cluster population, four galaxies are dark matter dominated, but they represent only 26% of the cluster population. The median stellar to dynamical mass fraction in the cluster population is 0.7, whereas for the non-members population this fraction is 0.4. This result is in agreement with the general trend of baryonic dominated systems in cluster galaxies. Part of the dark matter halo is lost when they fall into the centre of the cluster. Eichner (2013) found a truncated dark matter halo in a lensed elliptical, which is interpreted as a phenomenon of stripping effect on the dark matter halo.
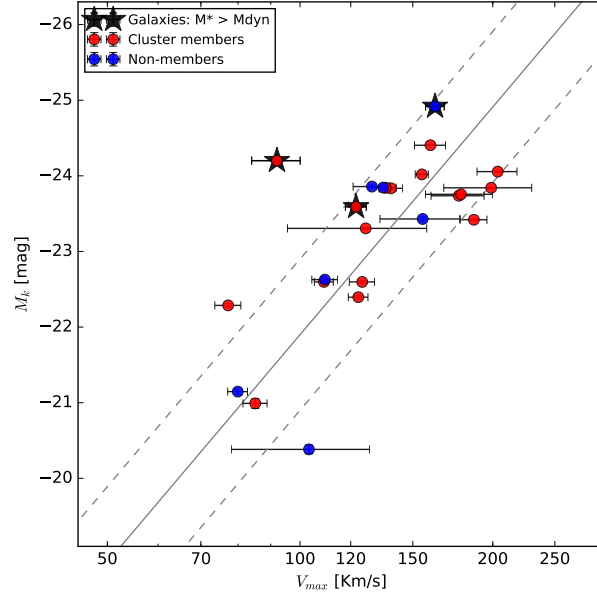

Figure 5.13: K-Band Tully-Fisher relation highlighting the galaxies with stellar masses greater than their dynamical masses.

Interestingly, one non-members galaxy and two cluster members do not show dark matter content, even more, their stellar mass content is larger than the total mass derived from their rotation velocity (see fig: 5.13). Since the rotation curve velocity is an indicator of the total mass content, the dynamical mass should always be greater or similar to the stellar mass content. One of this two cluster members was found to have underestimated V_{max}, therefore this fraction (3.61) does not represent the real stellar to dark matter fraction. The remaining galaxies are located inside the local Tully-Fisher trend, and the reason for this difference remains unclear.

5.5.5 Hubble Type and the Tully-Fisher relation

There are some trends in the properties of galaxies with Hubble type. The dark matter fraction increases with increasing Hubble type. Early type disk galaxies are in general more massive than the late type counterparts. Late type disk galaxies have younger stellar populations.
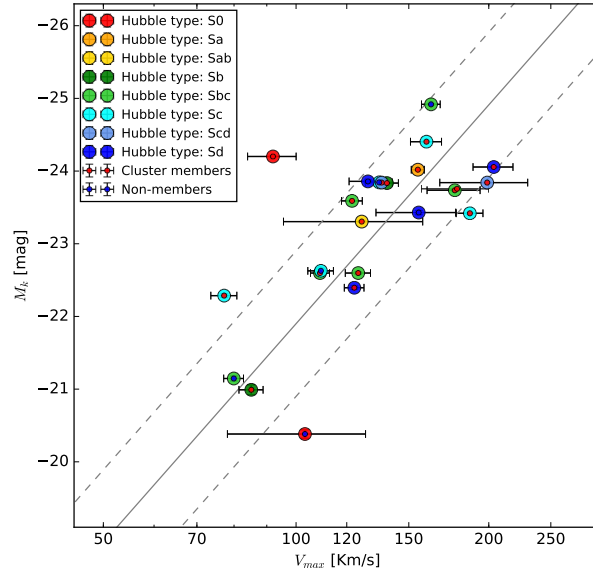

Figure 5.14: K-Band Tully-Fisher relation showing the galaxies with Hubble type

In this context, Rubin et al. (1985b) found greater rotation velocities for early type galaxies. At a fixed velocity, the luminosity of an early type disk galaxy decreases in the blue band and increases in redder bands when compared to late Type spirals. Additionally, at fixed luminosities, the rotation velocities decrease from Sa to Sc Hubble Type. The author found that the shape of the rotation curve does not depend on the Hubble Type, with the exception observing a bulge dominant luminosity in early

type spirals. Giraud (1986) found an increasing slope at a zero point for early to late type disk galaxies in the B-Band Tully-Fisher relations. Bösch et al. (2013b) found an increase in luminosity of -0.09 mag for each T-Type (T1=Sa, T2= Sab, T3=Sb, T4=Sbc, T5=Sc, T6=Scd, T7=Sd) in the B-Band Tully-Fisher relation.

Figure 5.14 shows the Hubble type of the galaxies the galaxies presented here in the Tully-Fisher relation. This result does not show any trend of increasing luminosity for the early-type galaxies in the K-Band Tully-Fisher relation. The increased scatter for late-Type spiral is also not observed here. It is not clear if environmental or gravitational effects are responsible for this result. The lower number of galaxies for these results are not statistically significant. A larger galaxy sample is needed.

5.6 Stellar Mass

The figure 5.15 shows the Stellar Mass Tully-Fisher relation. This has similarities to the K-Band Tully-Fisher relation as presented before, as the stellar mass values are derived from the K-Band magnitude. This broadband traces the old population of the galaxies. Since the analysis is similar to the K-Band Tully-Fisher relation and has been described in detail before, it will not be discussed here.
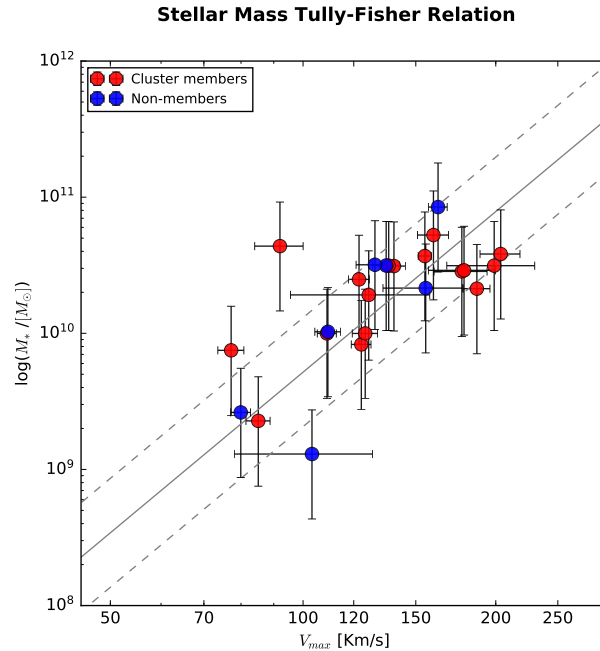

Figure 5.15: Stellar mass Tully-Fisher relation for cluster members and non-members. The grey line and dashed lines are the slope for the local Tully-Fisher relation with the errors.

5.7 morpho-kinematic classification of distorted galaxies

As mention in Section 5.1, an important observational fact of the Abell 2163 cluster is its very low number fraction of star forming galaxies. It is thought to have less, by roughly half, than the fraction found in several massive clusters.

The first question that arises is, are most of the galaxies quenched due to cluster specific quenching processes when falling into the cluster centres or rather have they been quenched before they have been accreted by the cluster. Dressler et al. (2013) have published an interesting study about the evolution of galaxies in five rich clusters as part of the IMACS cluster building survey by means of their spectral signatures. The authors found that ∼50 % of the cluster population are in-falling galaxies, two third of them belong to groups. The balance are virialised populations of the galaxy cluster. Galaxies that are part of groups are affected by group environment, where major and minor merger play a fundamental role. These galaxies begin the "preprocessing phase" of quenching and several cases of morphological transformations before they enter the cluster environment. This affect may be dominate when considering the high number of passive galaxies falling into the clusters. In this context, passive galaxies are created by major mergers. This is the case for elliptical galaxies. Environmental effects such as strangulation and ram pressure stripping is the case for S0 galaxies. Moreover, in a rich intracluster medium, the cluster environmental affects might be sufficient to quench galaxies quickly, which might be the case for the in-falling field population. First in-falling cluster galaxies are affected by strangulation effects. Here they loose part of their halo and their cold gas reservoir. Afterwards viscous pressure dominates. This strips away the remaining gas. This process is very effective for galaxies that have first been subjected to strangulation effects.

In a cluster population a high number of star forming galaxies affected by ram pressure stripping effects is to be expected. Since the strength of the viscous pressure is proportional to the ICM density and the squared velocity of the galaxy, it is more effective in the cluster centre, where galaxies reach the highest velocities and the the ICM density is the highest. Strangulation on the other hand, does not leave any imprint in the kinematics or morphology. Major mergers are not common in cluster environment. Nevertheless, interacting galaxies and mergers are found in accreted groups and galaxy pairs, principally in the outskirts of the cluster. Galaxies in dense environments, groups and clusters, have larger relative velocities and therefore harassment may occur for galaxy encounters. Instead of merger, galaxies with high velocities fly-by close, altering or destroying their morphology. In this process, their kinematics

and their morphology will be affected. Warps and an asymmetric shape are common imprint of this process.

Irregulars Non-cluster members are composed of groups members, merging systems, pairs and interacting systems. However undistorted systems with regular morphology and kinematics are found mostly in the field. These galaxies are not included here. As explained before, major and minor mergers as well as interacting galaxies are expected in this sub-group of galaxies.

In this section, a subjective analysis was performed of distortion signatures in the morphology and kinematics of the sub-sample of irregular galaxies. In addition, any remarkable features in the galaxy spectra of the same sample were explored. The goal being the identification of ongoing environmental and gravitational affects acting on these galaxies. For this purpose, a sample galaxy's morphology, their extracted line of sight rotation curve and the emission line shape were examined by eye and compared with simulated models and observational data of the above mentioned processes.

- **Ram pressure stripping** is a common phenomena responsible for the quenching of galaxies in rich environments. These kinematic and morphological signatures are well investigated in simulations and observational studies. The identification of this affect on cluster galaxies is based on studies from the following authors: Kronberger et al. (2008),Kapferer et al. (2008),Kapferer et al. (2009),Bellhouse et al. (2017),Bösch et al. (2013a),Jaffé et al. (2011),Jaffé et al. (2015). Gas rich galaxies falling into the cluster centre during their first passage will experience ram pressure if this is higher than the anchoring self-gravity. As this takes place galaxies gain and lose speed. This is dictated by the cluster potential and continues until they become quenched and virialised Jaffé et al. (2015). This affect is very strong in low-mass galaxies. Its effect depends on the in-falling angle. For face-on in-falling galaxies, distortions on the kinematics are observed in the outer regions, whereas in the edge-on cases the in-falling side shows strong distortions with declining velocities (Kronberger et al. (2006); Kronberger et al. (2008); **?**). In the effected side, the gas scale length is truncated, which compared to the stellar disk shows the division line where the gas has been stripped away and the remaining part of the disk that still has gas. The ram pressure triggers star formation on the surface where its acts over the galaxy gas. Morphologically this phenomena might not affect the appearance of the galaxy and may explain the high number of kinematically distorted galaxies in cluster. Nevertheless, if the mass of the stripped gas is high enough, it might begin forming new stars. Star formation might be found in the wake up to hundred of Kpc of the galaxy (Kapferer et al. (2009)). The orientation of the

filaments of the stripped gas shows the in-falling direction of the galaxy.

- **Strangulation** is described by the following authors: Peng et al. (2015),Rasmussen et al. (2008) and Kawata and Mulchaey (2007) among of others. It refers to removing the cold gas located in the galaxy halos, in which the star formation will cease ones the galaxy has consumed its gas available in the disk. This process is not observable directly but via the analysis of the galaxy metallicities and simulations.

- **Major merger** systems are well identify in photometric images and in their kinematics. The criteria for the identification of mergers is based on the following authors Bellocchi et al. (2016),Barrera-Ballesteros et al. (2015),Rodriguez-Gomez et al. (2017), Hung et al. (2015)Weigel et al. (2017)Darg et al. (2010) among of others. Since a major merger involves two galaxies of nearly the same mass, the gravitational interaction between them will destroy their kinematics and morphology transforming two disk galaxies in a spheroidal one. Distortions on the kinematics depend on the interaction state of the mergers and it is at highest for mergers with two close nuclei. Until virialisation, merger remnants show high dispersion velocity and a high fraction of them might conserve part of their rotational velocities. Therefore, galaxies showing two nuclei, pattern of passage, unwinding spiral arms in an almost spheroidal galaxies are the common criteria in morphology of mergers. Ongoing mergers show asymmetries from 30% to 100% in their kinematics, without a common pattern.

- **Minor mergers** involve the merging of a large galaxies and a dwarf galaxy. The identification of their kinematic and morphological imprints are based on the following authors: Haynes et al. (2000),Qu et al. (2011),Gómez et al. (2012),Krabbe et al. (2008). In optical photometry it is quite difficult to identify a minor merger event due to the high intensity of the large galaxy. However, they are better observed in edge-on galaxies when they fall into the disk, or in the outer disk. In minor mergers, the kinematics of the star and gas are usually decoupled. In this process, the dispersion velocity increases while the circular velocity decreases. Furthermore, bump signatures are observed indicating variation of the regular circular velocity and are related to the interactions. Resulting in warps, rings and tidal features.

- **Interacting galaxies** are the prior phase of merging system. Most of the previously mentioned authors mentioned show kinematics and morphology from interacting systems to post-mergers, therefore their information is used here to identify interacting systems. Interacting galaxies are still well separated but they usually display tidal bridges connecting both galaxies. The asymmetries in the

kinematics produced by interactions start from 3% to 40%.

- **Harassment** is addressed by the following authors: Moore et al. (1996); Moore et al. (1998, 1999),González-García et al. (2005),Smith et al. (2015) and Bialas et al. (2015) among others. Harassment as mergers, transform the morphology of the galaxies drastically. In this process, up to 50% of stars might be lost to the circumstellar medium, resulting in galaxies with flatter shapes. The effectiveness of the destruction of the encounters depend on the impact parameters such as the spin orientation, inclinations, mass ratio and the encounter velocity. The kinematics signatures start from fine distortion to complete random motions.

- The identification of **warps** are based on the morphological and kinematic information published by the following authors Battaglia et al. (2006),Kamphuis et al. (2015),Józsa (2007); Józsa et al. (2009),Arnaboldi and Galletta (1993). Warps are not always visible in optical images, but better traced in 21cm observations. This phenomena is even more difficult to detect in the galaxy kinematics as the weak asymmetry caused by this process might be comparable with the noise of the extracted kinematics. This is not the case for extreme warp cases, their emission lines spectra show a characteristic profile, which extends almost straight and suddenly flattens in the outer regions. These borders could be connected with the continuum through a weak bridge. Examples of mechanisms that produce warps are **harassment, gas in-fall and interaction** with companion galaxies.

In the sub-sample of irregular galaxies (Fig: 5.16), six cluster galaxies show distorted kinematics and six have distorted kinematics and morphology, whereas one shows only a distorted morphology but regular kinematics. Almost all galaxies with distorted kinematics are candidates for being effected by ram pressure stripping. The galaxies close to the cluster centre and sub-cluster B centre show filaments and trails of star formation in the stripped gas, which suggest strong ram pressure exerted by the IGM on their gas components. Few galaxies with distorted morphology and kinematics are located in the outskirts of the cluster. These galaxies show signatures of ongoing violent gravitational interaction such as merging or harassment.

From the non-members group, 11 galaxies are classified as galaxies with distorted kinematics and morphology. These galaxies show signatures of galaxy interactions, minor merger or gas in-fall, warps and harassment. From the remaining eight galaxies, six of them show signatures of distortions only in their kinematics, whereas two galaxies are slightly distorted in their morphology. Possible mechanisms acting on the kinematic of these galaxies are ram pressure stripping for rich group members, and minor mergers or cannibalisms, since these two affects are not always visible in the morphology of massive galaxies. For the group with only distorted morphology, there is not a clear

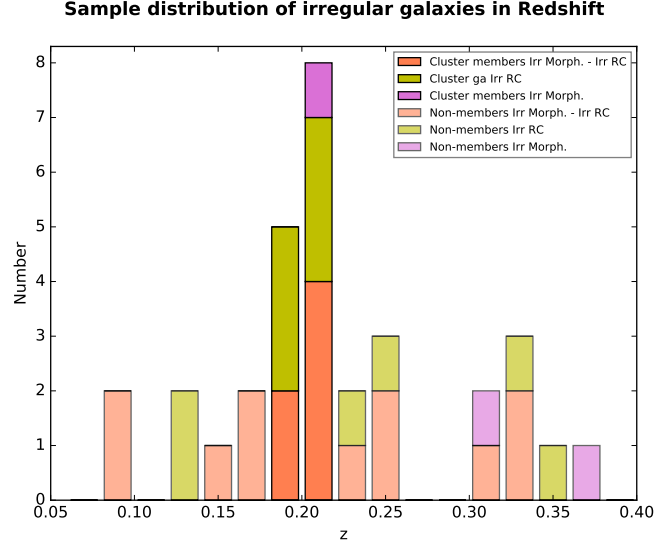evidence of an ongoing phenomena acting on these galaxies.

Figure 5.16: Sample distribution of irregular galaxies in redshift bins of z=0.2. Galaxies classified as undetermined are included. Brightest colours show the cluster galaxies and pastel colours show the non-members. Different colours show the galaxies with irregular morphology, kinematics or both in violet, green and coral colours respectively.

Below is a brief description of the distortion signatures for each irregular galaxy along with the suggested ongoing phenomena. This is presented by means of its R-Band image, emission line spectra and its extracted line of sight rotation curve. In the photometric image north is on the top and east is on the left. In the extracted rotation curves starting from the kinematic centre, the negative positions, in arcsec, shows the kinematics along the mayor axis from the upper disk part of the galaxy while the positive positions shows the kinematics in the lower part of the galaxy. Receding and approaching part of the galaxy have positive and negative velocities respectively.

- **2011_Q1_9**. at z=0.33. Early type star forming galaxy with a compact bulge. On the north-east part, an elongated structure is visible. It appears as though it is connected with the galaxy, it may be a tidal stream or a bridge structure between two interacting galaxies. Otherwise it may be a background or foreground galaxy. On the south, between the galaxy and the bright star, there is a small and bright clump. The kinematics of the galaxy are irregular and asymmetric. The approaching rotation curve shape - negative velocities - shows a bump which gives hints of interaction signatures with the small bright clump in the south. The receding part of the rotation curve shows irregularities. Compared with the literature, the shape of the rotation curve is similar to that of an fly-by interacting system. Therefore, the distorted kinematics and the hints of interacting

64

signatures in the morphology suggest a galaxy effected by gravitational interaction with a companion, although it is not clear if it is undergoing harassment or merging.

- **w16_Q1_4** at z=0.33. Galaxy with regular morphology close to an elliptical galaxy in the south and two bright stars in the north. Its kinematics shows regular rotation curve until the outer part where it rises suddenly. It is not clear if this increased velocity is related either to a low signal to noise in the emission line of the outer part or if it is an effect of tidal disturbances.

- **w8_Q1_15** at z=0.30. Galaxy with an irregular morphology. A compact bulge inside of a disk structure is observed. Moreover, around the galaxy a boxy structure encloses the galaxy disk. The east part shows signatures of a loop. In the south part, there is a weak wake that connects the galaxy to the structure on the south. However, the emission line in the south is truncated, opposite as what is expected for an interacting bridge. The kinematics shows a lower velocity at the centre that increase rapidly in the middle of the extracted rotation curve. The irregular morphology shows hints of harassment affects. This is in agreement with distorted kinematics.

- **w8_Q1_17** at z=0.25. Interacting galaxy with a small companion on the south, visible in the residual image on the right. In the north there is a small bright structure that could either be connected to the galaxy or it is a background structure. The kinematics shows distortions in its approaching part in the south that is likely related with the interaction to the small companion. The distortion in the kinematics is widely extended up to the centre of the galaxy. Therefore, the morphological and kinematic signatures suggest an ongoing minor merger event. Gravitational interactions at larger distances only affect one side of galaxy disk.

- **w8_Q1_26** at z=0.0866. and **w8_Q1_25** at z=0.0870. Low-mass galaxy pair at a low redshift. The galaxy on the north shows a weak tail at the south that could possibly connect to the companion galaxy. The galaxy on the south shows a regular morphology. Additional, the kinematics of both galaxies show strong distortions due to the gravitational interactions.

- **2010_Q2_10** at z=0.30. Compact galaxy with a prominent arm in the north. The kinematics shows regular morphology. This is likely to be the extracted kinematics as they do not reach the outer part of the galaxy. The morphological distortions hint to a post-merger system.

- **2011_Q2_5u** at z=0.2. Cluster galaxy with regular compact spheroidal morphology. The emission line spectra indicates that the gas scale length is not

extended to the outer regions. An irregular rotation curve. Flat rotation in the centre suggests a large velocity dispersion in this part. Asymmetric and random distortions suggest effects of past gravitational interactions, such as remnants of a merger event. The affect of ram pressure is unclear in its kinematics.

- **2010_Q2_20** at z=0.2. Cluster galaxy with irregular morphology and kinematics. Its morphology and kinematics are similar to galaxies with a prominent warp, which have been effected by harassment processes. The kinematics does not show clearly whether it have also been influenced by ram pressure from the ICM.

- **w1_Q2_19** at z=0.34. Spiral galaxy showing a weak spiral arm in the north. In the south-east, a bright clump is visible that might be a prolongation of the spiral arm. This galaxy shows irregular kinematics. The extracted position velocity is extended to the north reaching the spiral arm. The morphology and the rotation curve shape suggest gravitational interaction with a companion, in which case the clump south-east could be the interacting companion.

- **w1_Q2_1** at z=0.2. Early-type cluster member with regular morphology. Spiral arms are not visible except for the weak feature on the north which gives a hint of a spiral arm structure. The stellar distribution shows a relaxed S0-Type galaxy. The kinematics shows distortions in the approaching and receding side which might be the result of gravitational interactions. Therefore, its kinematics and morphology suggest a galaxy result of a previous merging event, with imprints of spiral structures of the parent galaxies in its homogeneous disk. The gas component is not relaxed jet. Moreover, the close projected distance to the to the cluster-B centre would suggest strong effects of ram pressure stripping, but this affect is not clear in its kinematics.

- **w1_Q2_21** at z=0.2. Cluster member with a peculiar morphology. Its smooth centre typical of a late-type galaxy is surrounded by a light distribution highly asymmetric which is not related to a galaxy disk. The simulated galaxy, seen in Fig.6 of **?** shows similar appearance. The galaxy model is a dwarf galaxy inside of a dense halo that has undergone several passages. It has been effected by tidal and ram pressure stripping affects which has torqued its structure. Additionally, dust and gas filaments resulting from ram pressure stripping are visible. Although the morphology is quite distorted, the kinematics shows only weak distortions on the outer region. It can be assumed that this galaxy is probably undergoing a strong tidal and ram pressure stripping affects that are responsible for the distorted morphology and kinematics. Despite of its strong distorted morphology, there are no hints of strong gravitational interactions in its kine-

matics.

- **w1_Q2_7** at z=0.2. Galaxy member of the cluster Abell 2163 with regular morphology. Its light distribution is concentrated in the centre suggesting a prominent bulge of an early-type galaxy. The kinematics are distributed asymmetrically with a lower receding velocity in the south part and a higher approaching velocity in the north part. The lower velocity could be due to ram pressure stripping. Its projected position with respect to the cluster centre suggests that it is falling towards the subcluster-B centre from the outskirts.

- **2010_Q3_11** at z=0.25. Early type star forming galaxy with regular morphology and small distortions in its kinematics. The kinematics do not show hints of tidal interactions in the outer regions and it is possible that the surrounding galaxies might be foreground or background structures. There is a small distortion in the receding part close to the centre that could result from a close companion. Nevertheless, due to the large errors in the kinematics, it is not clear if any of the distortions are real.

- **2010_Q3_12** at z=0.2. Early type cluster galaxy falling from the outskirts into the cluster centre. Its evolution morphology and low star formation activity suggest preprocessing affects. This galaxy shows asymmetric kinematics with lower velocities in the approaching north part and higher velocities in receding south part. The kinematic centre is shifted with respect to the luminous centre which suggests remnants of a minor merger event.

- **2011_Q3_14** at z=0.15. Galaxy showing an irregular morphology with a signature of a warp structure. Its intense star formation activity, as indication by the bright emission line, and the irregular kinematics suggest recent gravitational interactions. These might be responsible for the large velocity dispersion in the disk which is apparent from the observed the line width. Warps originate from minor mergers, harassment or gas in-fall. It is unclear whether the larger velocity extracted in the outer regions are real or not. If they are, it might either be gas escaping from the galaxy, harassment or a bridge that connects the galaxy with the encounter.

- **2011_Q3_16** at z=0.23. Galaxy with irregular morphology, that does not show a clear centre in its light distribution. Its kinematics shows irregularities. The rotation velocity increases steeply and then flattens in the south, whereas in the north it increases slowly and continuously. This asymmetry suggests a possible harassment mechanism or gravitational interactions acting on this galaxy.

- **w10_Q3_26** at z=0.2. Cluster galaxy with irregular morphology and kinematics.

The east part of the galaxy shows a filamentary structure with ongoing star formation activity, signature of strong ram pressure. The kinematics shows that the gas in the disk is compressed in one side, in the direction in which the galaxy is moving. The direction of the long wake suggests that the galaxy has already crossed the centre of the cluster and is moving away.

- **w2_Q3_4** at z=0.23 Early-type galaxy with a prominent bulge structure. From the morphological structure it is not clear if it is a face-on disk galaxy or a spheroidal galaxy. Its kinematics show strong distortions that are blue shifted at both parts of the galaxy. This could be introduced by a major merger event or harassment. Signatures of an ongoing merger event are not visible in the optical image.

- **w_M1_Q3_16** at z=0.13. Disk galaxy with an asymmetric brightness distribution in the centre. A bright small structure is visible close to the north-west part of the galaxy. The kinematics of the galaxy are irregular. The velocity gradient in the centre is quite small, that could come from a dispersion dominated bulge. The extracted rotation curve does not reach the maximum velocity in the south part of the galaxy. The kinematics of the north part do not show signatures of interaction with the clump observed in the image. There are not signatures of interaction in the photometric image, but the imprints in the kinematics show possible remnants of gravitational interactions.

- **w_M1_Q3_7** at z=0.17 Galaxy with increased star formation in the centre as it can be seen in the emission line spectra. The photometric image shows a weak tail in the south south-east part connected to the galaxy. This indicates a minor merger or gas inflow that has triggered the current strong star formation in the galaxy centre as well as its high velocity dispersion. The kinematics shows distortions at the centre that may be connected with the weak structure observed in the optical image.

- **2011_Q4_5** at z=0.2. Cluster member with regular morphology. The galaxy studied is the background galaxy in the photometric image, while the foreground galaxy has a lower redshift. Its kinematics shows zero velocity within 2.3 Kpc from the centre towards the north-west and it rises suddenly to the outer disk. The galaxy does not show a bulge and its line width does not suggest higher velocity dispersion. It is not clear which mechanisms act on this galaxy, which have resulted in a considerable reduction of the rotation velocity. Ram pressure stripping affect is not imprinted in the kinematics of this galaxy.

- **2011_Q4_9** at z=0.2. Cluster member with a truncated light distribution in the

east part. Its projected position is close to the in-falling group D centre. The galaxy shows asymmetric kinematics, with low velocities in the north-east east part of the disk. The morphology suggests ram pressure stripping acting on this galaxy, which has already truncated the gaseous disk as it falls into the group centre.

- **2011_Q4_10** at z=0.2. Cluster member with a diffused light distribution in the galaxy disk. A weak tail structure is visible in the south-west part. Its kinematics its asymmetric with lower velocity in the north east part and rising velocities in the south-west part. This galaxy is located close to the in-falling group D centre as it can be seen from its projected location. The kinematics and morphology suggest a galaxy which has been effected by harassment processes in the past and it is undergoing strong ram pressure stripping as it falls into a denser ICM.

- **w_M1_Q3_15** at z=0.25. Galaxy with a double nuclei and a peanut shape. This galaxy shows a clear morphology of a merger system. In the south part, a weak and broad tail is visible, whereas in the north part the galaxy shows a weak narrow tail. These features could be remnants of arms of its progenitors. The kinematics shows distortion in the side where both galaxies are interacting. From examining the spectra, it appears as though the merger event has triggered the intense star formation.

- **2011_Q4_6** at z=0.2. Cluster galaxy with a prominent warp surrounded by a diffuse light distribution in its halo. Filaments are visible in direction south south-west that begin in the galaxy disk and extend out to the ICM. The kinematics of the galaxy are irregular. The north part shows a truncated gaseous disk while in the south part the line of sight velocities increase quickly to a maximum velocity and then decline for several Kpc. The combination of the morphology and kinematics suggest a galaxy that has been effected by harassment and it is undergoing strong ram pressure stripping as it falls into the cluster centre. Its projected distance to the cluster centre suggests a strong ram pressure acting on its gaseous component. This affect might be responsible for compressing the stripped gas and triggering star formation in the wake.

- **2010_Q4_8** at z=0.2. Massive gas rich disk galaxy member of the Abell 2163 cluster. The light distribution in the south outer disk is truncated. This suggests a process that has began removing the cold gas before it starts forming stars intensively. The galaxy does not show a strong bulge. This galaxy might have been a gas rich field galaxy before it was bound by the cluster. The kinematics show a truncated rotation curve in the south and an extended flat part in the

north up to a 25 Kpc radius. Its projected position to the cluster centre A2, its truncated south gas disk and its filamentary structure suggest strong ram pressure stripping acting on the gas of the galaxy. The stripped gas is compressed by the same mechanism that has triggered star formation visible in the filaments. The kinematics does not show interaction with the structures in the north.

- **2010_Q4_9** at z=0.34 Galaxy with regular morphology close to a bright star at the west. Its rotation curve shows a bump close to the centre in the north-east part of the disk. It suggests gravitational interactions with a low-mass structure, such as minor mergers.

- **w11_Q4_18** at z=0.13 Early-Type galaxy with a prominent bulge. The galaxy shows regular morphology and irregular rotation curve. The south part of the disk shows a distortion with the shape of a prominent bump, which is typical of gravitational interactions with a less massive structure.

- **w3_Q4_22** at z=0.17. Galaxy with irregular morphology and kinematics. It shows an asymmetric disk in morphology. The north west disk appears truncated in the visible light distribution. Its intense emission line with a broad line width suggests intense star formation activity and higher dispersion velocities. The galaxy shows irregularities in its kinematics. It is not clear which processes could have modify strongly the kinematics without visible effects in its morphology.

- **w_M1_Q4_11** at z=0.37. Galaxy with irregular morphology. It has a diffuse and similar distributed light intensity to the edges, without a clear centre but a slightly brighter region on the east part (left). Its morphology suggests that is has undergone harassment affects. In that case, its kinematics should present distortions which are not visible from the extracted rotation velocities. Therefore, it is not clear which physical processes could influence the morphology of this galaxy without affecting its kinematics.

- **w_M1_Q4_3** at z=0.2. Early-Type cluster galaxy with regular morphology and asymmetric kinematics. This galaxy shows two weak structures in the north-east and north-west part. The kinematics show a bump in the south part of the galaxy, characteristic of gravitational interactions with a low mass structure such as minor merger. The kinematics in the north part does not show distortions from gravitational interactions, therefore both clumps in the north are probably not interacting with the galaxy. The kinematics shows lower velocities in the north part, then decreases in the middle of the disk. This imprint is typical for ram pressure acting on the gas of the galaxy as it falls into denser environments.
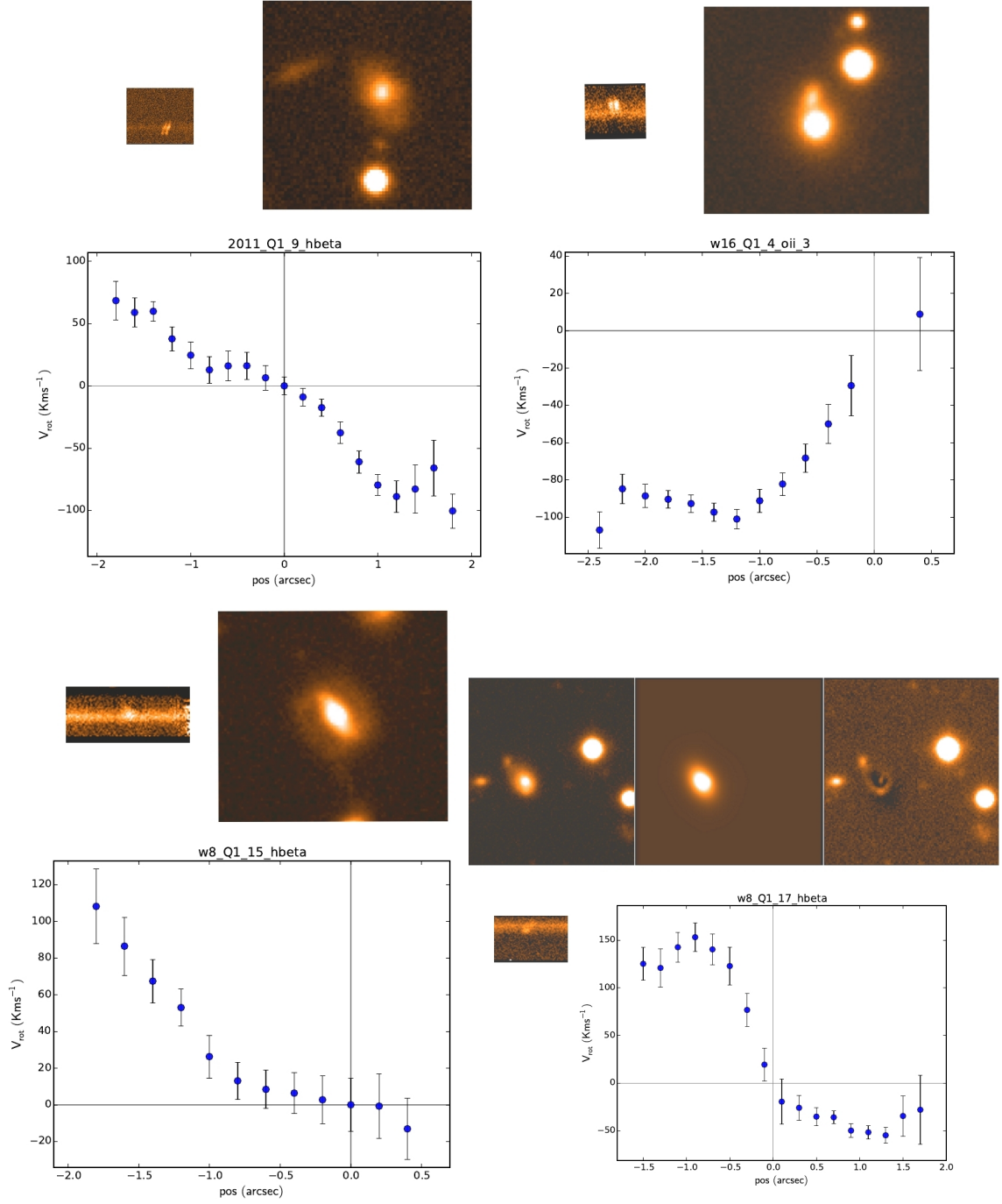
Figure 5.17: R-Band image, spectra and line of sight rotation curve of the galaxies: 2011_Q1_9, w16_Q1_4, w8_Q1_15 and w8_Q1_17.
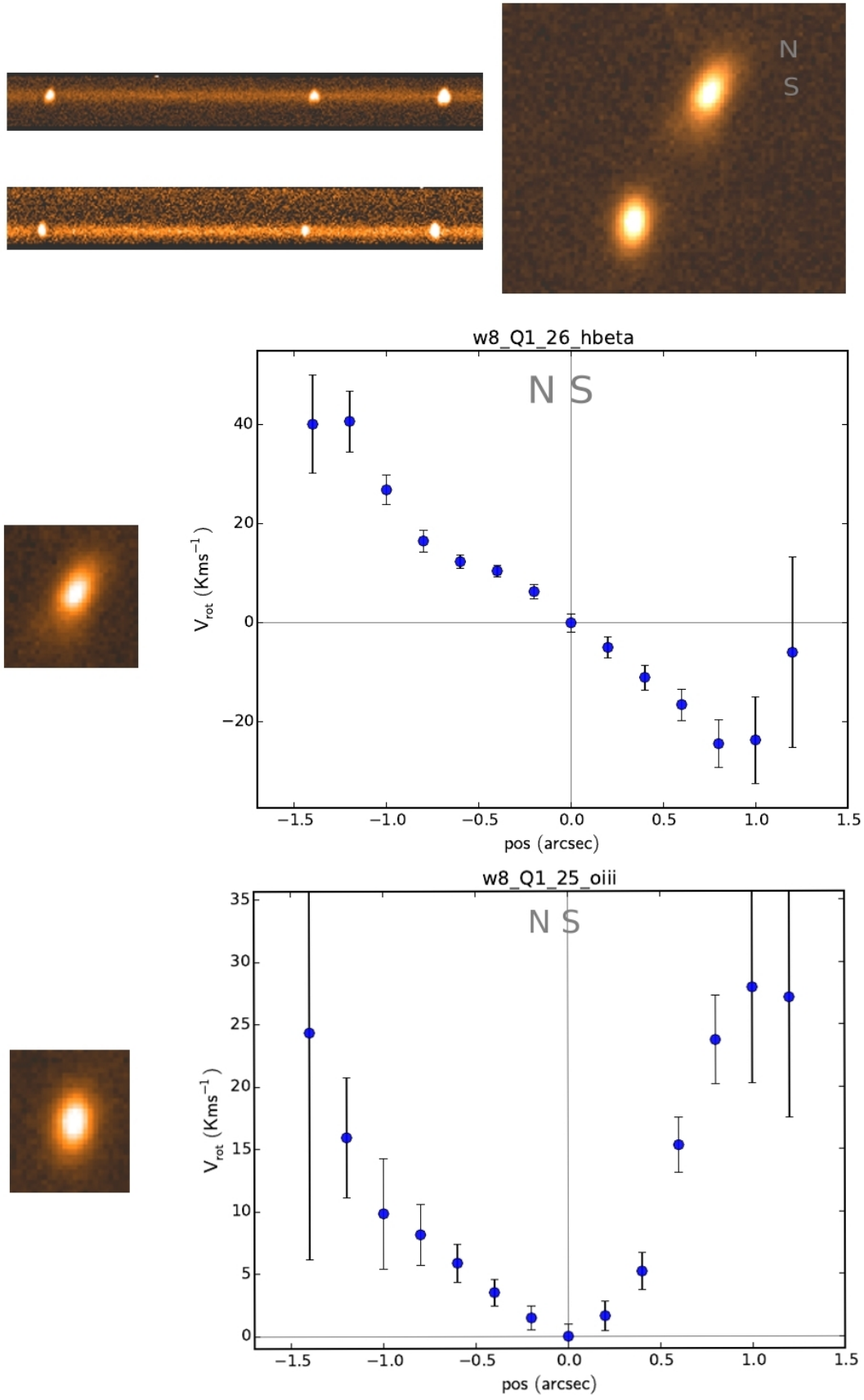
Figure 5.18: R-Band image, spectra and line of sight rotation curve of the galaxies: w8_Q1_26 and w8_Q1_25.
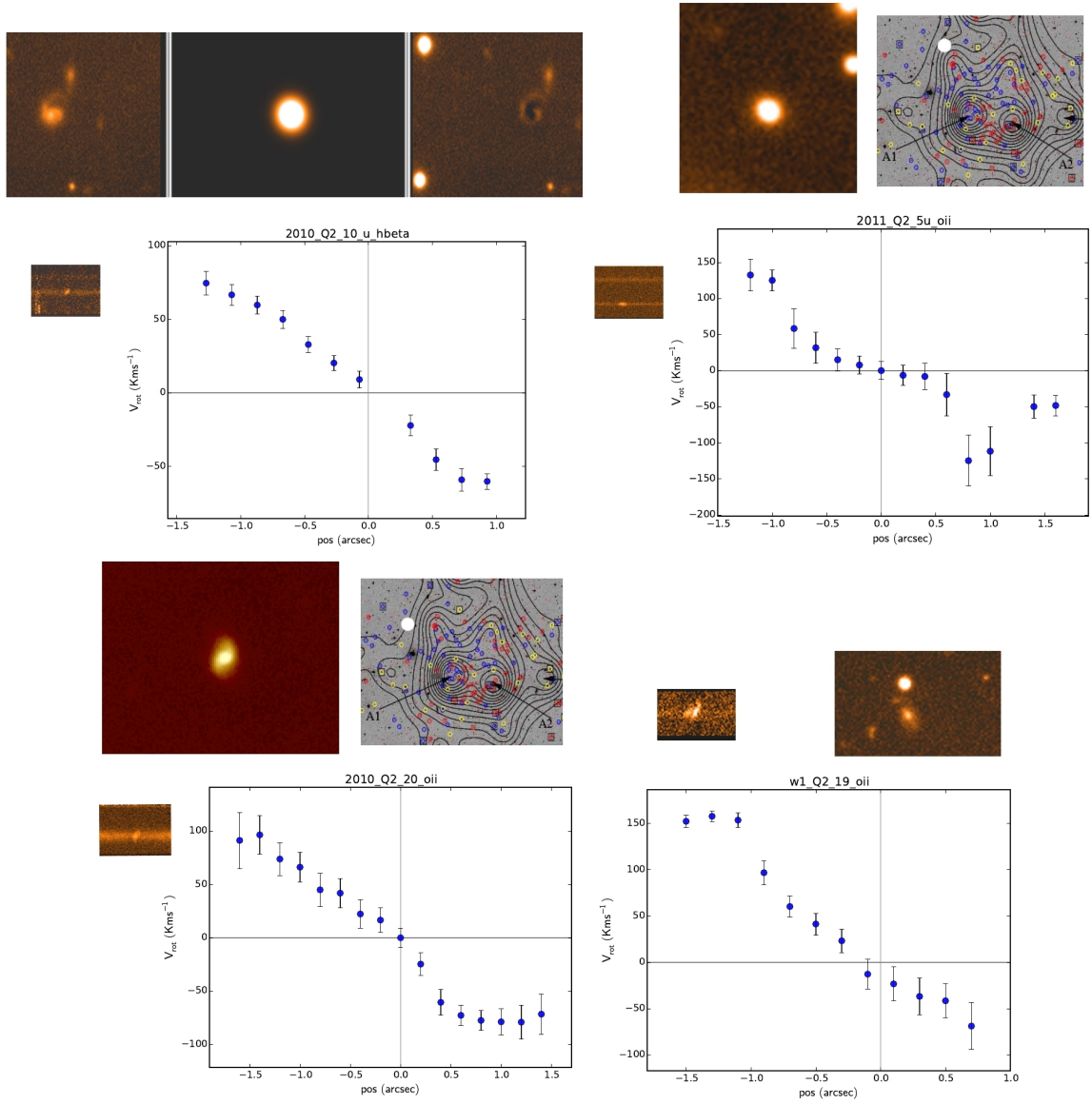
Figure 5.19: R-Band image, spectra and line of sight rotation curve of the galaxies: 2010_Q2_10u, 2011_Q2_5u, 2010_Q2_20 and w1_Q2_19.
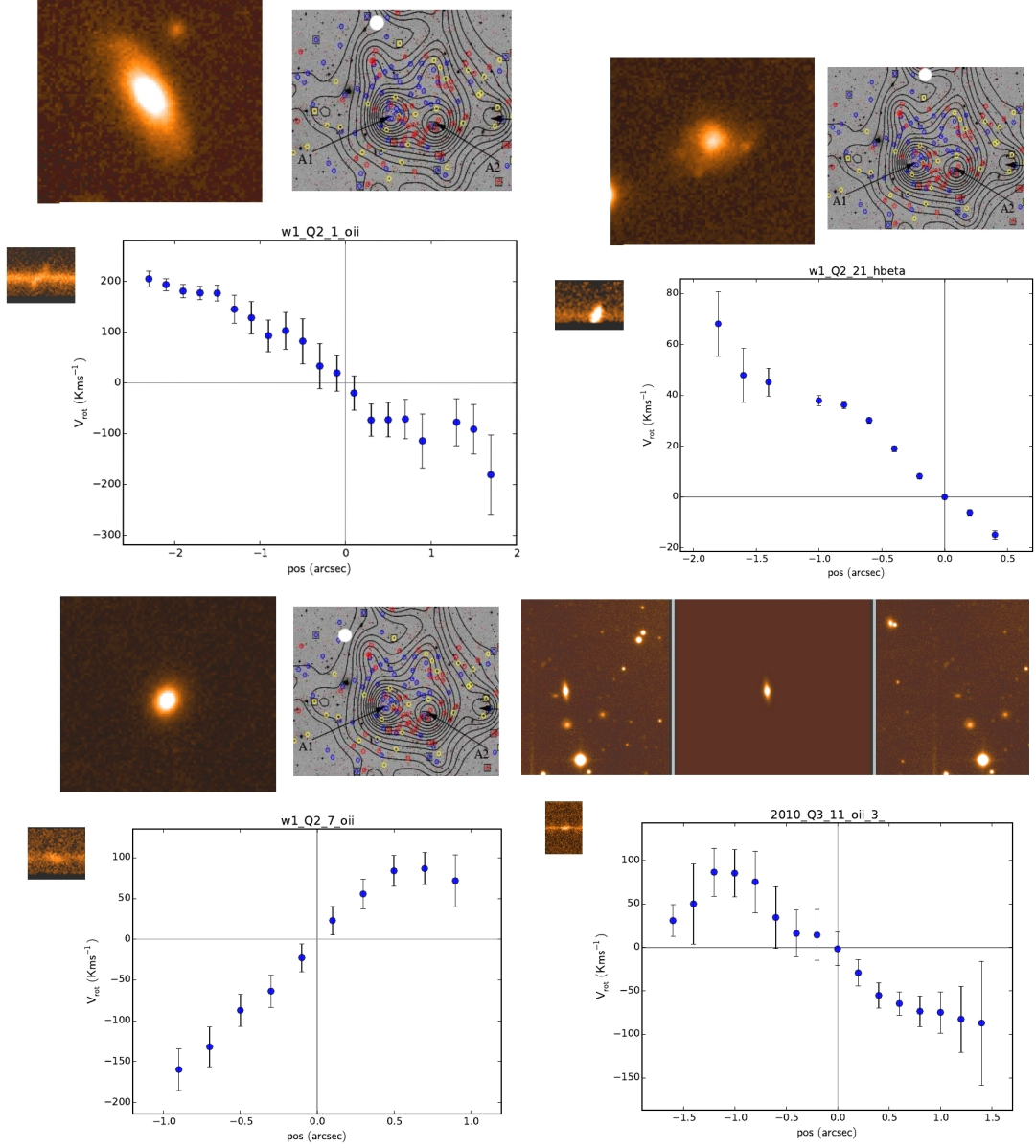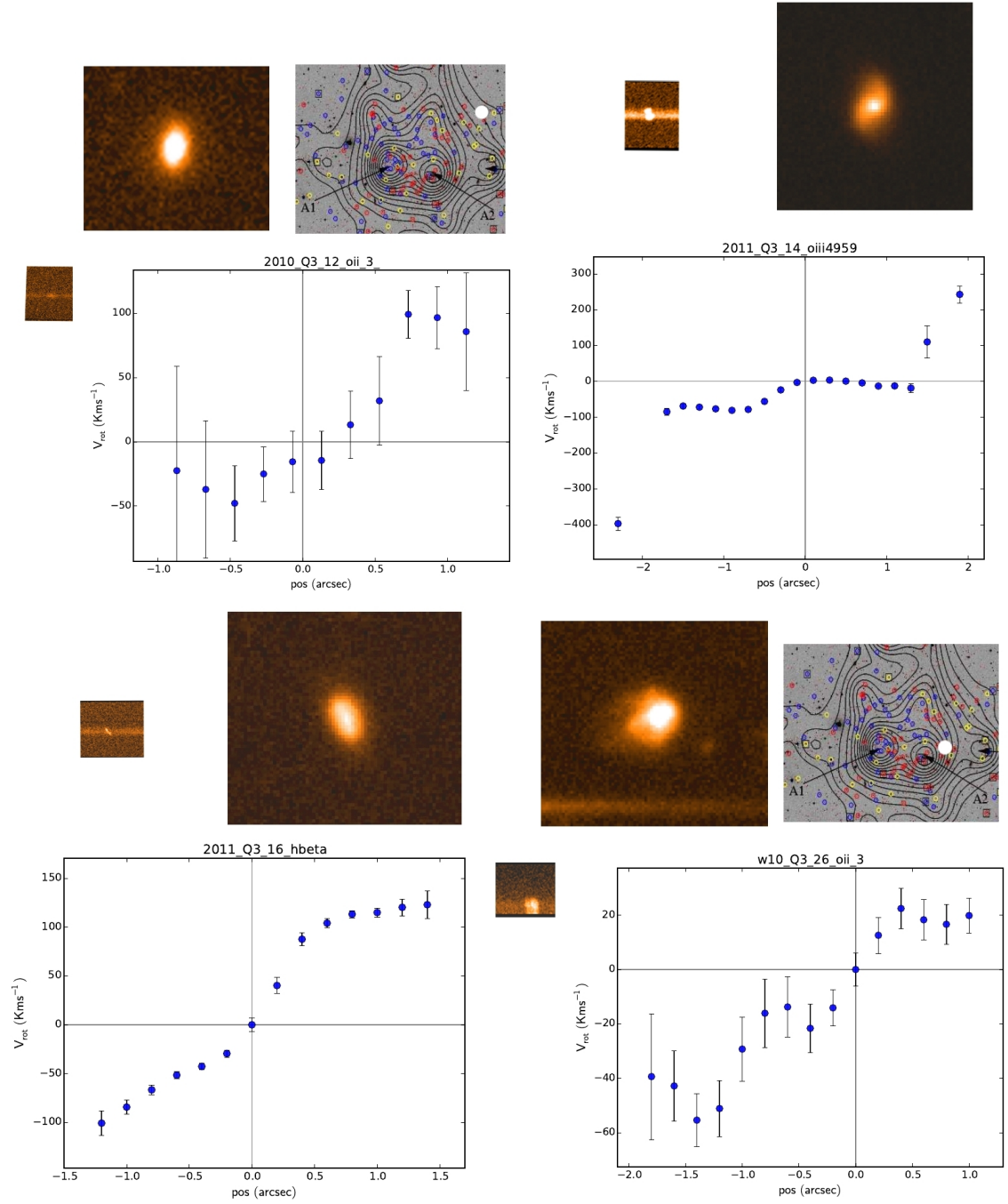
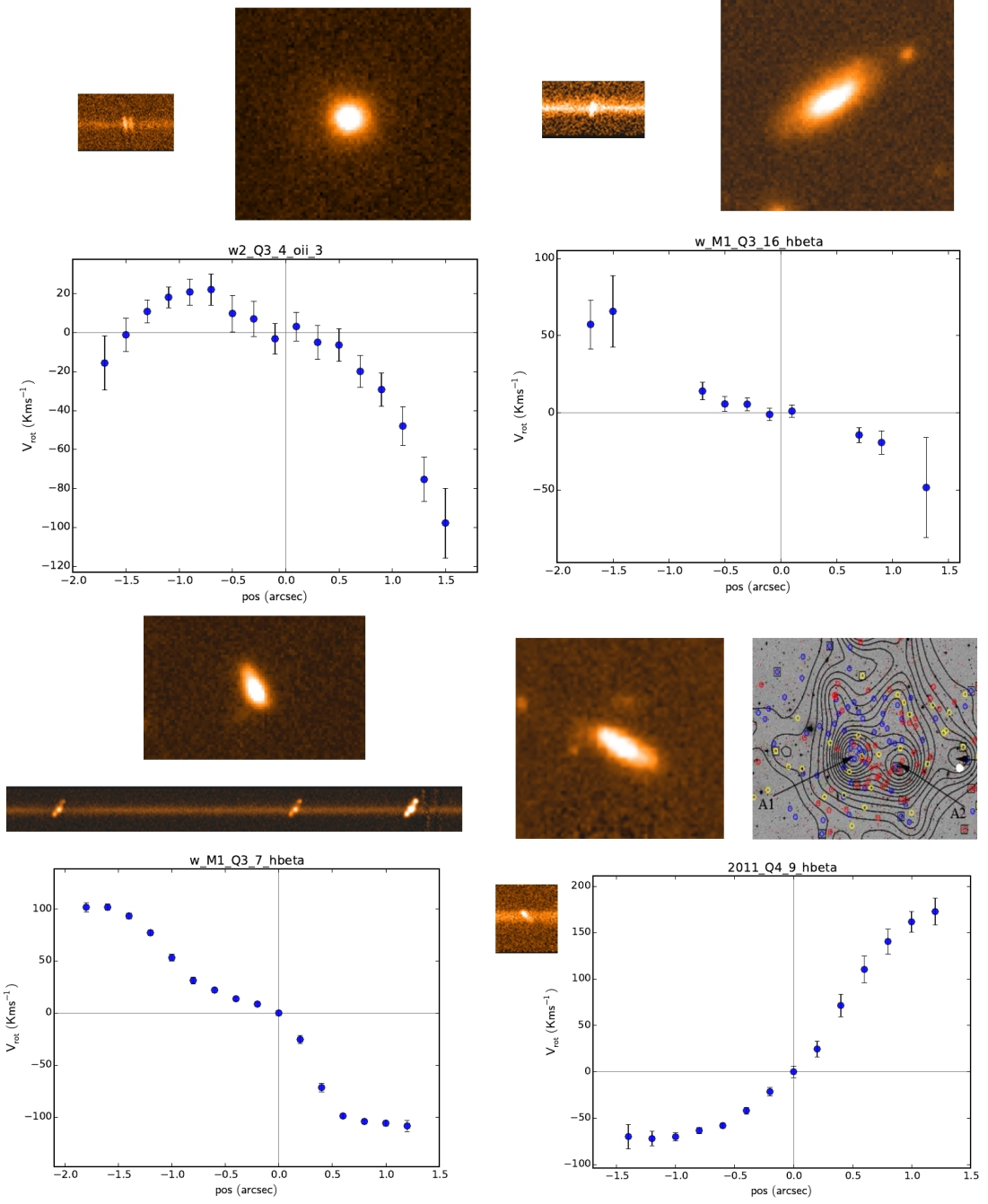Figure 5.20: R-Band image, spectra and line of sight rotation curve of the galaxies: w1_Q2_1, w1_Q2_21, w1_Q2_7 and 2010_Q3_11. The image on the left is the original image. The image in the middle is the *GALFIT* model of the galaxy and on the right it is the residual image (i.e. the original photometric image minus the galaxy model).

Figure 5.21: R-Band image, spectra and line of sight rotation curve of the galaxies: 2010_Q3_12, 2011_Q3_14, 2011_Q3_16 and w10_Q3_26.

Figure 5.22: R-Band image, spectra and line of sight rotation curve of the galaxies: w2_Q3_4, w_M1_Q3_16, w_M1_Q3_7 and 2011_Q4_9.

76
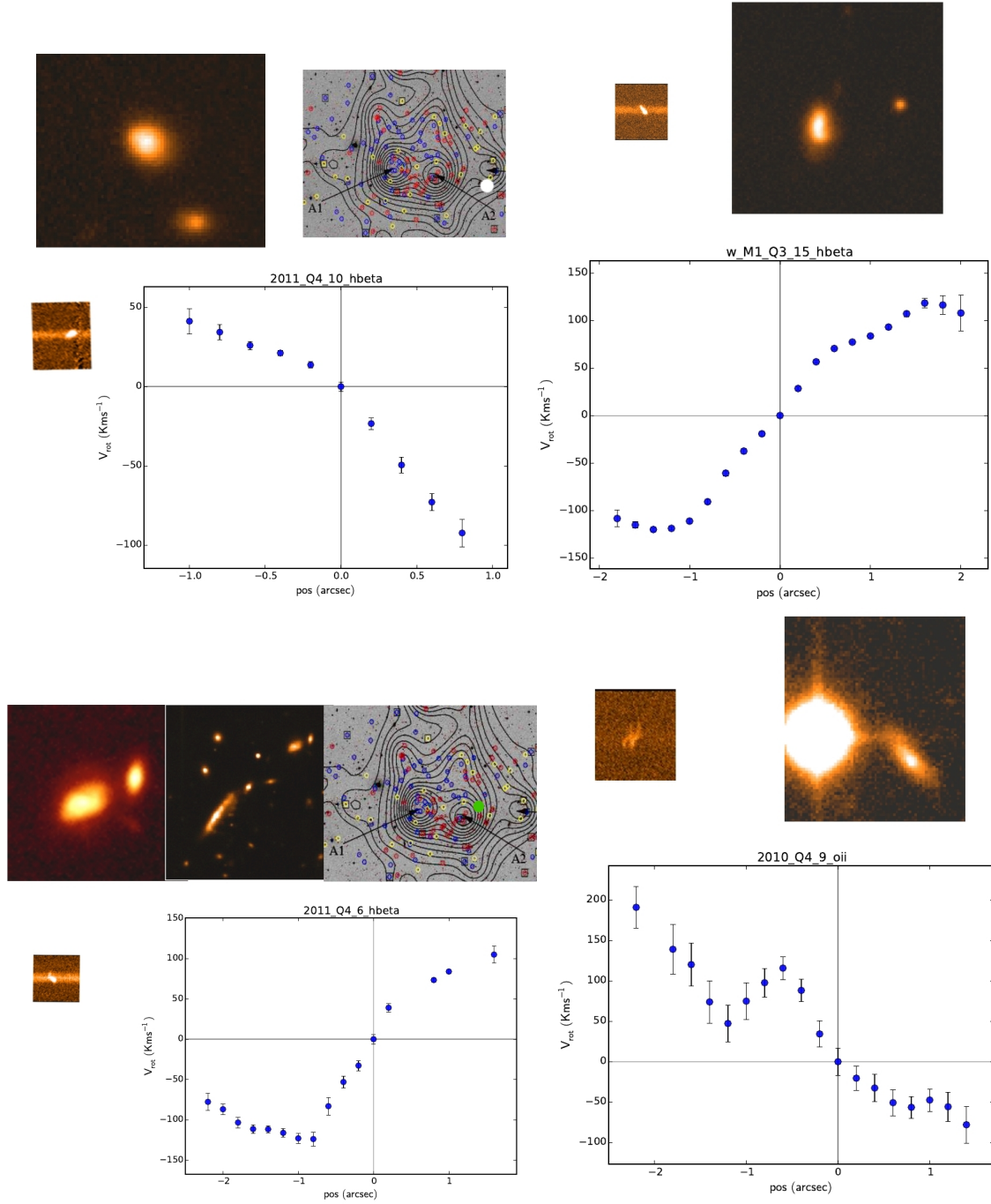
Figure 5.23: R-Band image, spectra and line of sight rotation curve of the galaxies: 2011_Q4_10, w_M1_Q3_15, 2011_Q4_6 and 2010_Q4_9. The image on the left is the original image. In the second row, first column. The image in the middle shows the galaxies 2011_Q4_6 in the top right corner, north-west to the galaxy 2010_Q4_8 (figure 5.24. Next page.) and the surrounding field.
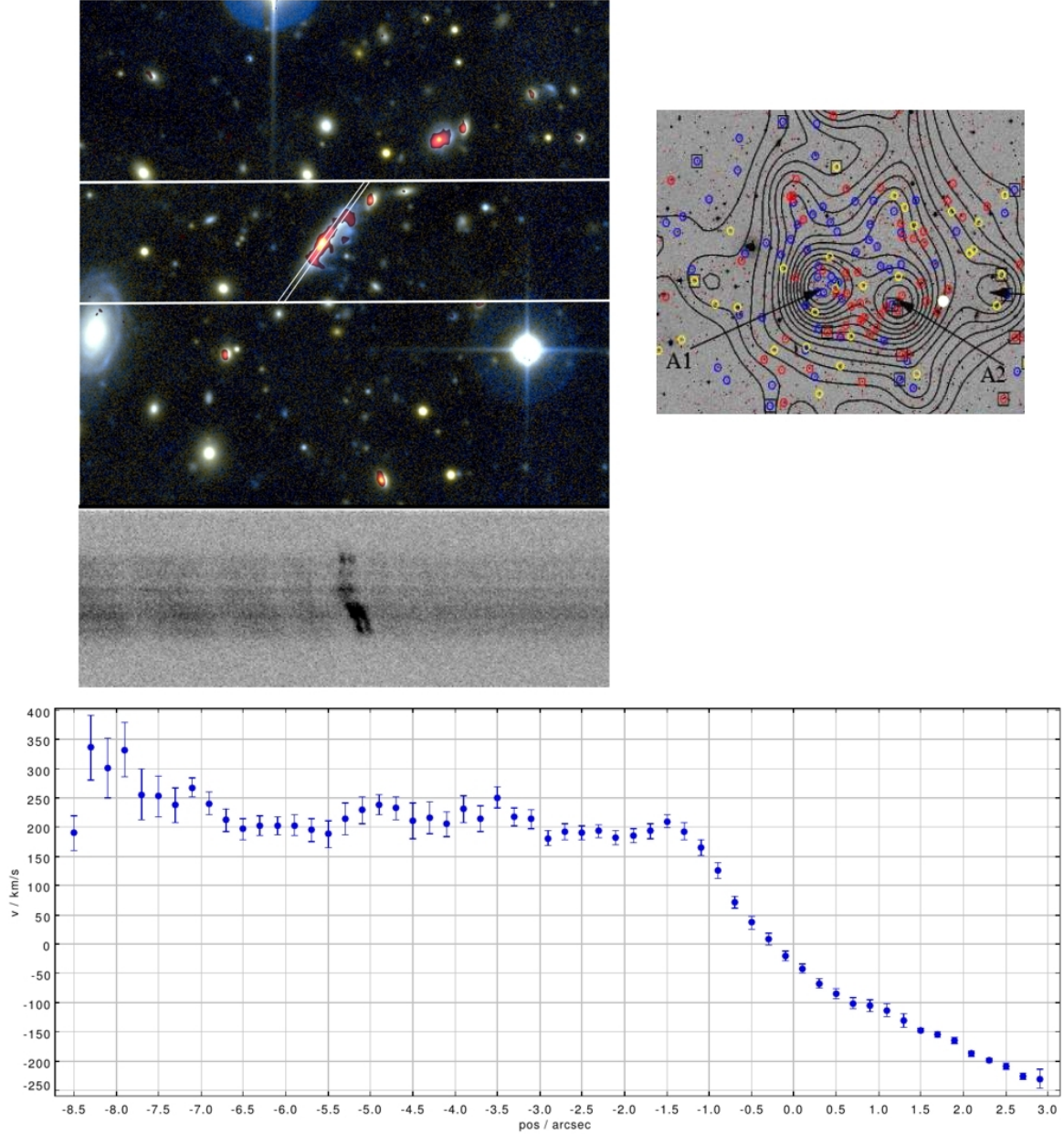
Figure 5.24: R-Band image, spectra and line of sight rotation curve of the galaxy: 2010_Q4_8. The image shows the position of the slit as a white line. Superimposed in red is the Hα narrow band image. This was used to calculate the star formation rate of the cluster galaxies. It should be noted that the analysis of the star formation rate and the data reduction processes of the Hα image have been performed by Dr. M. Verdugo, my supervisor and they are not part of this thesis. The Hα emission shows a clear truncated distribution of the gas in the south outer part of this galaxy. The star formation activity is truncated in the outer part of the disk and shows the shape of a crab which is typical of a galaxy affected by strong ram pressure stripping. This is falling face on towards the cluster centre. Additionally, stars are being newly formed in the filamentary structure of the stripped gas.
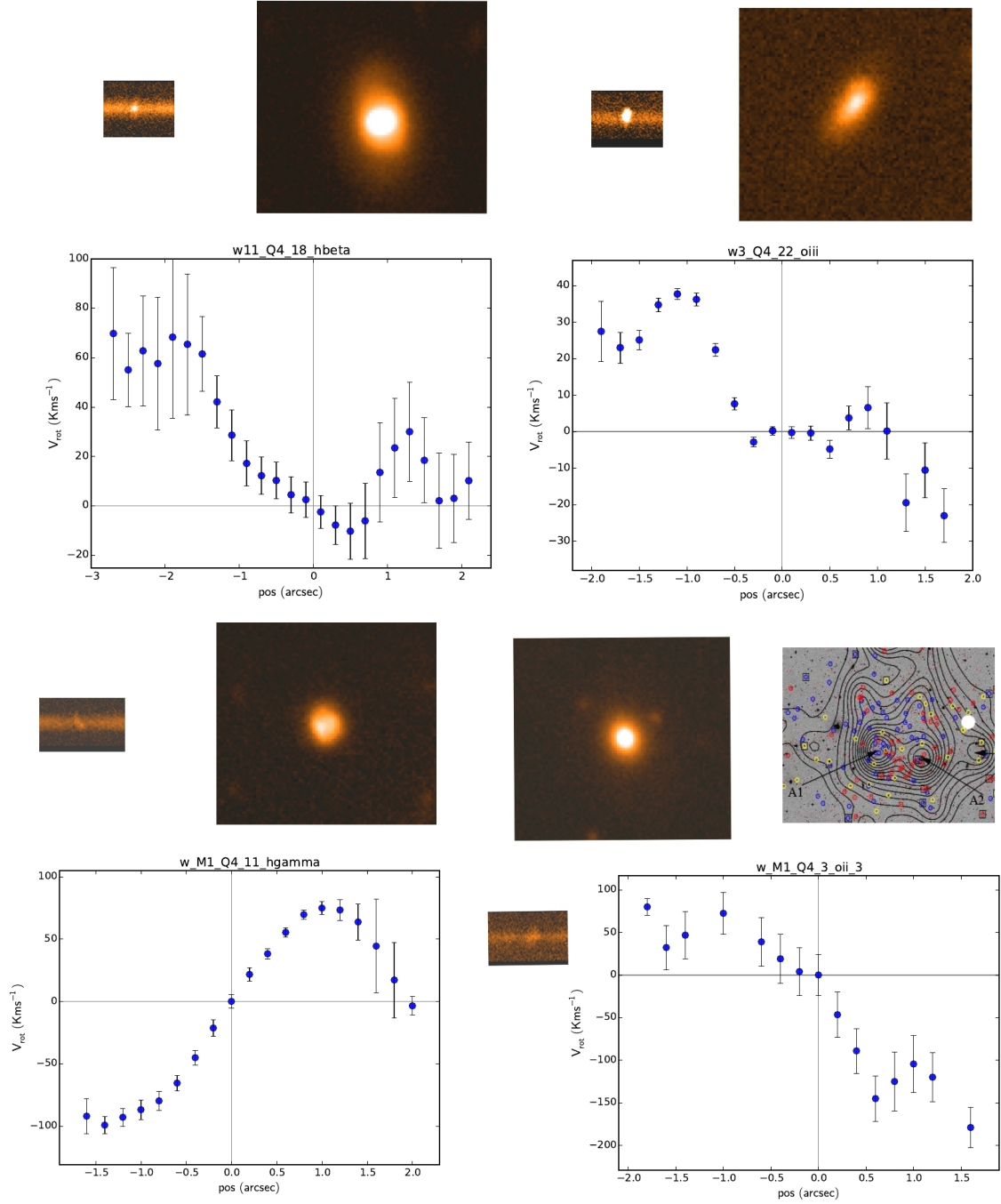
Figure 5.25: R-Band image, emission line spectra and the extracted line of sight rotation curve of the galaxies: w11_Q4_18, w3_Q4_22, w_M1_Q4_11 and w_M1_Q4_3. The galaxy in the second row, first column, shows the extracted line of sight rotation velocity of the Hγ emission. This is the only galaxy in the "non-cluster group" that displays strong signatures of harassment. This phenomenon is not typical for less dense environments. Although there are no close galaxies in the surrounding area, it could be part of a rich group. The last galaxy is a member of the cluster Abell 2163 and is falling into the cluster centre.

5.8 Summary and conclusions

This thesis is based on the morphological and kinematic analysis of a sample of galaxies with redshift lower than z<0.4. Half of the galaxies in the sample are members of the massive cluster Abell 2163 at redshift z~0.2, while the "non-members" are group members, pairs, interacting galaxies and field galaxies. The galaxy sample consists of galaxies with regular and irregular morphology. The Tully-Fisher relation was derived from the sub-sample of regular galaxies to study possible differences in the luminosities and rotation velocities from cluster and non-cluster galaxies, as well as the possible evolution of this relation. For the sub-sample of irregular galaxies, a morpho-kinematic analysis was performed with the aim to identify possible environmental effects and gravitational interaction processes acting on the galaxies. Additionally, to pinpoint galaxies responsible for the distortions in their morphologies or kinematics or both.

The most important results are listed below.

The galaxy sample

- Only 11% of the cluster members observed are star forming galaxies, while the balance are passive galaxies. This value is half of the fraction of the star forming galaxy population observed in several massive complex clusters. This result indicates the impact of preprocessing mechanisms in the consumption the gas in galaxies members. This starts acting when galaxies are members of smaller structures, like groups, before they have been accreted by the cluster Abell 2163.

- After a visual inspection, the galaxy sample was divided in two sub-samples of regular and irregular galaxies, by means of their kinematics and morphology. 17 galaxies are classified as regular and 27 galaxies show irregularities. Six galaxies were classified as "regular/irregular" with no clear distortions. They were added to both sub-groups.

The sub-sample of regular galaxies

- The galaxies studied here follow the local k-Band Tully-Fisher relation. There is no evidence of evolution in the Tully-Fisher relation derived in this sub-sample of galaxies as it has been found in several studies before.

- There is no clear difference in the Tully-Fisher relation for cluster members and non-members. When fitting the slope of the Tully-Fisher relation for cluster members, it shows a shallower slope. This result suggests a mass-dependent enhancement of the luminosity in cluster members, which could be caused by environmental effects in cluster environments.

- In the sub-sample of regular galaxies, cluster members are baryonic dominated galaxies whereas non-members are dark matter dominated systems. The average stellar to dynamical mass fraction in the cluster and non-cluster population is 0.7 and 0.4 respectively. Two galaxies - one cluster member and one non-member- have stellar masses greater than their calculated dynamical masses. These galaxies appear normal in their properties, but a deeper analysis should be performed to understand their nature.

- No correlation was found in the Tully-Fisher relation for galaxies with different Hubble-Type.

The sub-sample of irregular galaxies

- In the sub-sample of irregular galaxies, environmental affects and gravitational interactions were identified in the cluster and non-cluster population.

- The processes acting on the cluster members are related to their projected position with respect to the cluster centre. Galaxies close to the cluster centre, sub-cluster B centre and in-falling groups centres show effects of ram pressure stripping while irregular galaxies in the outskirts are affected by gravitational interaction processes such as merger and tidal tails. Several cluster members show signatures of harassment affects.

- Non-cluster members are generally distorted by galaxy interaction processes such as minor and major merger and interacting pairs. Nevertheless the morphology and kinematics of some galaxies suggest hints of harassment and ram pressure stripping, which can take place in rich galaxy groups.

Deutsche Zusammenfassung

Die vorliegende Masterarbeit untersucht sowohl die Kinematik der Galaxien mit Sternentstehung in verschiedenen Umgebungen als auch die Prägung der physikalischen Transformationsprozesse, die in der Kinematik und Morphologie beobachten werden können.

Im Universum, Galaxien befinden sich in verschiedenen Umgebungen. Isolierte Galaxien haben reguläre Morphologie und Kinematik. Aber wenn das gravitationspotential durch Störungen beeinflusst wird, kann sich eines oder beides verändern. Galaxien in dichter Umgebung, wie zum Beispiel Mitglieder von massereichen Galaxiengruppen oder Galaxienhaufen, hingegen erfahren physikalischen Transformationsprozesse schneller auf Grund von Wechselwirkung mit der Umgebung. Wechselwirkende Galaxien wie Galaxienverschmelzung und Harassment können ihre Morphologie und Kinematik komplett verändern, während in Ram Pressure Stripping nur die Gas Komponente beeinflusst wird, ihre Morphologie jedoch gleich bleibt. Alle diese Prozesse sind abgedruckt in die Rotationskurve und Morphologie.

Diese Masterarbeit wurde als Teil einer Kollaboration zwischen die Gruppe von Prof. Ziegler in Wien und Prof. Maurogordato in Toulouse gemacht und wurde auf spektroskopischen Beobachtungen basiert, die zwischen 2005 und 2011 mit VLT/VIMOS durchgefürt wurden. Strukturparameter wurden entweder aus meinem Bachelorarbeit (Menacho (2012)) genommen oder hier abgeleitet. Ein Ziel der Beobachtung war, die Effekte von Transformationsprozessen in Galaxien zu untersuchen, deshlab mehr als die Hälfte der Galaxien in der Sample zeigen Abweichungen in ihrer Kinematik und Morphologie.

Diese Arbeit beschäftigt sich speziell mit den Mitgliedern der Galaxienhaufen Abell 2163. Dabei wurden die abgeleiteten Parameter von Galaxien Mitgliedern und nicht-Mitgliedern genau analysiert und verglichen. Nicht-Mitgliedern sind isolierte Galaxien, Mitgliedern von Galaxiengruppen und Wechselwirkende Galaxien.

Das Galaxien-Sample besteht aus 53 Galaxien mit einer Rotverschiebung zwischen z=0.05 und z=0.4. Ihre stellare Masse variiert zwischen 10^9 und 10^{11}. Die Balmer-

linien Hα, Hβ und die verbotenen Emissionslinien [OIII] $\lambda5007$ wurden benutzt um die kinematische Information wie Rotationsgeschwindigkeit, dynamische Masse und die Form der Rotationskurve zu gewinnen. R-Band und K-Band Photometrie wurde für die morphologische Analyse benutzt.

Die Ergebnisse dieser Arbeit werden wie folgt zusammengefast: Die Hälfte der Galaxien in dem Sample sind Galaxienhaufen Mitglieder. Mehr als die Hälfte davon haben reguläre Rotationskurven. Von der Gruppe der nicht-Mitgliedern, nur ein Drittel sind im Gleichgewicht. 23 Galaxien haben insgesamt reguläre Rotationskurven. Davon haben nur 19 haben photometrische Information und wurden für die Tully-Fisher Beziehung verwendet.

Galaxien, die gestörte Rotationskurven aufweisen, wurden mit Hilfe ihrer Morphologie mit Rotationskurven-Modellen von Simulationen oder Beobachtungen verglichen. Diese Analyse wurde benutzt, um Transformationsprozesse in diesen Galaxien zu identifizieren. Die kombinierte Analysis von Kinematik und Morphologie sind sehr Wichtig um die Entwicklungsprozesse in Galaxien zu verstehen.

List of Figures

List of Tables

References

Aarseth SJ, Fall SM (1980) Cosmological N-body simulations of galaxy merging. ApJ 236: 43–57.

Abadi MG, Moore B, Bower RG (1999) Ram pressure stripping of spiral galaxies in clusters. MNRAS 308, URL http://dx.doi.org/10.1046/j.1365-8711.1999.02715.x.

Aguilar LA, White SDM (1985) Tidal interactions between spherical galaxies. ApJ 295: 374, URL http://dx.doi.org/10.1086/163382.

Arnaboldi M, Galletta G (1993) Kinematical models of warped disks. A&A 268: 411–417.

Baldry IK, Glazebrook K, Brinkmann Jea (2004) Quantifying the Bimodal Color-Magnitude Distribution of Galaxies. ApJ 600: 681694, URL http://dx.doi.org/10.1086/380092.

Bamford SP, Aragón-Salamanca A, Milvang-Jensen B (2006) The Tully-Fisher relation of distant field galaxies. MNRAS 366: 308–320.

Bamford SP, Milvang-Jensen B, Aragón-Salamanca A, Simard L (2005) The Tully-Fisher relation of distant cluster galaxies. MNRAS 361: 109–127.

Barrera-Ballesteros JK, García-Lorenzo B, Falcón-Barroso J, van de Ven G, Lyubenova M, et al. (2015) Tracing kinematic (mis)alignments in CALIFA merging galaxies. Stellar and ionized gas kinematic orientations at every merger stage. A&A 582: A21.

Battaglia G, Fraternali F, Oosterloo T, Sancisi R (2006) ion{H}{i} study of the warped spiral galaxy NGC 5055: a disk/dark matter halo offset? A&A 447: 49–62.

Bellhouse C, Jaffé YL, Hau GKT, McGee SL, Poggianti BM, et al. (2017) GASP. II. A MUSE View of Extreme Ram-Pressure Stripping along the Line of Sight: Kinematics of the Jellyfish Galaxy JO201. ApJ 844: 49.

Bellocchi E, Arribas S, Colina L (2016) Distinguishing disks from mergers: Tracing the kinematic asymmetries in local (U)LIRGs using kinemetry-based criteria. A&A 591: A85.

Bertin E (2011) Automated Morphometry with SExtractor and PSFEx 442: 435.

Bertin E (2013) PSFEx: Point Spread Function Extractor .

Bertin E, Arnouts S (2010) SExtractor: Source Extractor .

Bialas D, Lisker T, Olczak C, Spurzem R, Kotulla R (2015) On the occurrence of galaxy harassment. A&A 576: A103.

Böhm A (2003) The evolution of distant spiral galaxies in the FORS Deep Field. Ph.D. thesis, Georg-August-Universitat zu Gottingen.

Böhm A, Ziegler BL, Saglia RP, Bender R, Fricke KJ, et al. (2004) The Tully-Fisher relation at intermediate redshift. A&A 420: 97–114, URL `http://dx.doi.org/10.1051/0004-6361:20034256`.

Bösch B, Böhm A, Wolf C, Aragón-Salamanca A, Barden M, et al. (2013a) Ram pressure and dusty red galaxies - key factors in the evolution of the multiple cluster system Abell 901/902. A&A 549: A142.

Bösch B, Böhm A, Wolf C, Aragón-Salamanca A, Ziegler BL, et al. (2013b) Tully-Fisher analysis of the multiple cluster system Abell 901/902. A&A 554: A97.

Bourdin H, Arnaud M, Mazzotta P, Pratt GW, Sauvageot JL, et al. (2011) A2163: Merger events in the hottest Abell galaxy cluster. A&A 527: A21, URL `http://dx.doi.org/10.1051/0004-6361/201014907`.

Butcher H, Oemler J A (1984) The evolution of galaxies in clusters. V - A study of populations since Z approximately equal to 0.5. ApJ 285: 426, URL `http://dx.doi.org/10.1086/162519`.

Cohen SA, Hickox RC, Wegner GA, Einasto M, Vennik J (2014) Star Formation and Substructure in Galaxy Clusters. ApJ 783: 136.

Courteau S (1997) Optical Rotation Curves and Linewidths for Tully-Fisher Applications. ApJ 114: 2402, URL `http://dx.doi.org/10.1086/118656`.

Courteau S, Rix HW (1997) Maximal Disks and the Tully-Fisher Relation 29: 1332.

Darg DW, Kaviraj S, Lintott CJ, Schawinski K, Sarzi M, et al. (2010) Galaxy Zoo: the fraction of merging galaxies in the SDSS and their morphologies. MNRAS 401: 1043–1056.

De Lucia G, Poggianti BM, Aragon-Salamanca A, White SDM, Zaritsky D, et al. (2007) The build-up of the colour-magnitude relation in galaxy clusters since z 0.8. MNRAS 374: 809822, URL `http://dx.doi.org/10.1111/j.1365-2966.2006.11199.x`.

Desai V, Dalcanton JJ, Aragon-Salamanca A, Jablonka P, Poggianti B, et al. (2007) The Morphological Content of 10 EDisCS Clusters at 0.5 ¡ z ¡ 0.8. ApJ 660: 1151164, URL `http://dx.doi.org/10.1086/513310`.

Di Matteo P, Combes F, Melchior AL, Semelin B (2007) Star formation efficiency in galaxy interactions and mergers: a statistical study. A&A 468: 61–81.

Dressler A (1980) Galaxy morphology in rich clusters - Implications for the formation and evolution of galaxies. AJ 236: 351, URL `http://dx.doi.org/10.1086/157753`.

Dressler A, Augustus Oemler J, Couch WJ, Smail I, Ellis RS, et al. (1997) Evolution

since z = 0.5 of the Morphology-Density Relation for Clusters of Galaxies. AJ 490: 577, URL `http://stacks.iop.org/0004-637X/490/i=2/a=577`.

Dressler A, Oemler A Jr, Poggianti BM, Gladders MD, Abramson L, et al. (2013) The IMACS Cluster Building Survey. II. Spectral Evolution of Galaxies in the Epoch of Cluster Assembly. ApJ 770: 62.

Eichner TM (2013) Dark matter distributions in Early-type galaxies from strong gravitational lensing. Ph.D. thesis, Ludwig-Maximilians-Universitat Munchen.

Eneev TM, Kozlov NN, Sunyaev RA (1973) Tidal Interaction of Galaxies. A&A 22: 41.

Feretti L, Fusco-Femiano R, Giovannini G, Govoni F (2001) The giant radio halo in Abell 2163. A&A 373: 106112, URL `http://dx.doi.org/10.1051/0004-6361:20010581`.

Feretti L, Orrù E, Brunetti G, Giovannini G, Kassim N, et al. (2004) Spectral index maps of the radio halos in Abell 665 and Abell 2163. A&A 423: 111119, URL `http://dx.doi.org/10.1051/0004-6361:20040316`.

Gallagher JS, Hunter DA (1984) Structure and Evolution of Irregular Galaxies. Annu Rev Astro Astrophys 22: 3774, URL `http://dx.doi.org/10.1146/annurev.aa.22.090184.000345`.

Giraud E (1986) The dependence of the Tully-Fisher relation on morphological type. ApJ 309: 512–521.

Gómez FA, Minchev I, Villalobos Á, O'Shea BW, Williams MEK (2012) Signatures of minor mergers in Milky Way like disc kinematics: ringing revisited. MNRAS 419: 2163–2172.

González-García AC, Aguerri JAL, Balcells M (2005) Harassment origin for kinematic substructures in dwarf elliptical galaxies? A&A 444: 803–812.

Gunn JE, Gott JR III (1972) On the Infall of Matter Into Clusters of Galaxies and Some Effects on Their Evolution. ApJ 176: 1.

Hausman MA, Ostriker JP (1978) Galactic cannibalism. III - The morphological evolution of galaxies and clusters. ApJ 224: 320, URL `http://dx.doi.org/10.1086/156380`.

Haynes MP, Jore KP, Barrett EA, Broeils AH, Murray BM (2000) Kinematic Evidence of Minor Mergers in Normal Sa Galaxies: NGC 3626, NGC 3900, NGC 4772, and NGC 5854. AJ 120: 703, URL `http://stacks.iop.org/1538-3881/120/i=2/a=703`.

Holwerda BW (2005) Source Extractor for Dummies v5. ArXiv Astrophysics e-prints .

Holz DE, Perlmutter S (2012) THE MOST MASSIVE OBJECTS IN THE UNIVERSE. ApJ 755: L36, URL `http://dx.doi.org/10.1088/2041-8205/755/2/L36`.

Houghton RCW (2015) Revisiting the original morphology-density relation. MNRAS 451: 3427–3436.

Hung CL, Rich JA, Yuan T, Larson KL, Casey CM, et al. (2015) Kinematic Classifications of Local Interacting Galaxies: Implications for the Merger/Disk Classifications at High-z. ApJ 803: 62.

Icke V (1985) Distant encounters between disk galaxies and the origen of S0 sspiral. A&A 144: 115–123.

Jaffé YL, Aragón-Salamanca A, Kuntschner H, Bamford S, Hoyos C, et al. (2011) The effect of the environment on the gas kinematics and the structure of distant galaxies. MNRAS 417: 1996–2019.

Jaffé YL, Smith R, Candlish GN, Poggianti BM, Sheen YK, et al. (2015) BUDHIES II: a phase-space view of H I gas stripping and star formation quenching in cluster galaxies. MNRAS 448: 1715–1728.

Józsa GIG (2007) Kinematic modelling of disk galaxies. II. A case-study of symmetrically warped galaxy disks. A&A 468: 903–917.

Józsa GIG, Oosterloo TA, Morganti R, Klein U, Erben T (2009) Kinematic modeling of disk galaxies. III. The warped "Spindle" NGC 2685. A&A 494: 489–508.

Kamphuis P, Józsa GIG, Oh SH, Spekkens K, Urbancic N, et al. (2015) Automated kinematic modelling of warped galaxy discs in large H I surveys: 3D tilted-ring fitting of H I emission cubes. MNRAS 452: 3139–3158.

Kapferer W, Knapp A, Schindler S, Kimeswenger S, van Kampen E (2005) Star formation rates and mass distributions in interacting galaxies. A&A 438: 87–101.

Kapferer W, Kronberger T, Ferrari C, Riser T, Schindler S (2008) On the influence of ram-pressure stripping on interacting galaxies in clusters. MNRAS 389: 1405–1413.

Kapferer W, Sluka C, Schindler S, Ferrari C, Ziegler B (2009) The effect of ram pressure on the star formation, mass distribution and morphology of galaxies. A&A 499: 87–102.

Kawata D, Mulchaey JS (2007) Strangulation in Galaxy Groups. ApJ 672: L103–L106, URL http://dx.doi.org/10.1086/526544.

Krabbe AC, Pastoriza MG, Winge C, Rodrigues I, Ferreiro DL (2008) Kinematics and physical properties of southern interacting galaxies: the minor merger AM2306-721. MNRAS 389: 1593–1604.

Kronberger T, Kapferer W, Ferrari C, Unterguggenberger S, Schindler S (2008) On the influence of ram-pressure stripping on the star formation of simulated spiral galaxies. A&A 481: 337–343, URL http://dx.doi.org/10.1051/0004-6361:20078904.

Kronberger T, Kapferer W, Schindler S, Böhm A, Kutdemir E, et al. (2006) Internal kinematics of modelled interacting disc galaxies. A&A 458: 69–78.

Kronberger T, Kapferer W, Schindler S, Ziegler BL (2007) 2D-velocity fields of sim-

ulated interacting disc galaxies. A&A 473: 761–770, URL http://dx.doi.org/10.1051/0004-6361:20077696.

Lang RH, Boyce PJ, Kilborn VA, Minchin RF, Disney MJ, et al. (2003) First results from the HI Jodrell All Sky Survey: inclination-dependent selection effects in a 21-cm blind survey. MNRAS 342: 738–758.

LeFevre O, Saisse M, Mancini D, Brau-Nogue S, Caputi O, et al. (2003) ¡title¿Commissioning and performances of the VLT-VIMOS¡/title¿. Instrument Design and Performance for Optical/Infrared Ground-based Telescopes URL http://dx.doi.org/10.1117/12.460959.

Madau P, Dickinson M (2014) Cosmic Star-Formation History. Annu Rev Astro Astrophys 52: 415–486, URL http://dx.doi.org/10.1146/annurev-astro-081811-125615.

Markevitch M, Gonzalez AH, David L, Vikhlinin A, Murray S, et al. (2002) A Textbook Example of a Bow Shock in the Merging Galaxy Cluster 1E 0657-56. ApJ 567: L27–L31, URL http://dx.doi.org/10.1086/339619.

Maurogordato S, Cappi A, Ferrari C, Benoist C, Mars G, et al. (2008) A 2163: Merger events in the hottest Abell galaxy cluster. A&A 481: 593–613, URL http://dx.doi.org/10.1051/0004-6361:20077614.

Menacho VM (2012) Study of galaxy structures in Abell 2163 with SExtractor and Galfit, bachelor Thesis.

Milvang-Jensen B, Aragón-Salamanca A, Hau GKT, Jørgensen I, Hjorth J (2003) The Tully-Fisher relation of cluster spirals at z= 0.83. MNRAS 339: L1–L5.

Moore B, Katz N, Lake G, Dressler A, Oemler A (1996) Galaxy harassment and the evolution of clusters of galaxies. Nature 379: 613–616.

Moore B, Lake G, Katz N (1998) Morphological Transformation from Galaxy Harassment. ApJ 495: 139–151, URL http://dx.doi.org/10.1086/305264.

Moore B, Lake G, Quinn T, Stadel J (1999) On the survival and destruction of spiral galaxies in clusters. MNRAS 304: 465–474, URL http://dx.doi.org/10.1046/j.1365-8711.1999.02345.x.

Mortlock DJ, Warren SJ, Venemans BP, Patel M, Hewett PC, et al. (2011) A luminous quasar at a redshift of z = 7.085. Nature 474: 616–619, URL http://dx.doi.org/10.1038/nature10159.

Murray N, Quataert E, Thompson TA (2005) On the Maximum Luminosity of Galaxies and Their Central Black Holes: Feedback from Momentum-driven Winds. ApJ 618: 569–585, URL http://dx.doi.org/10.1086/426067.

Nakamura O, Aragón-Salamanca A, Milvang-Jensen B, Arimoto N, Ikuta C, et al. (2006) The Tully-Fisher relation of intermediate redshift field and cluster galaxies from Subaru spectroscopy. MNRAS 366: 144–162.

Peng CY, Ho LC, Impey CD, Rix HW (2002) Detailed Structural Decomposition of Galaxy Images. AJ 124: 266–293, URL `http://dx.doi.org/10.1086/340952`.

Peng CY, Ho LC, Impey CD, Rix HW (2010a) DETAILED DECOMPOSITION OF GALAXY IMAGES. II. BEYOND AXISYMMETRIC MODELS. AJ 139: 2097–2129, URL `http://dx.doi.org/10.1088/0004-6256/139/6/2097`.

Peng Y, Maiolino R, Cochrane R (2015) Strangulation as the primary mechanism for shutting down star formation in galaxies. Nature 521: 192–195.

Peng Yj, Lilly SJ, Kovac K, Bolzonella M, Pozzetti L, et al. (2010b) MASS AND ENVI-RONMENT AS DRIVERS OF GALAXY EVOLUTION IN SDSS AND zCOSMOS AND THE ORIGIN OF THE SCHECHTER FUNCTION. ApJ 721: 193–221, URL `http://dx.doi.org/10.1088/0004-637X/721/1/193`.

Peng Yj, Lilly SJ, Renzini A, Carollo M (2012) MASS AND ENVIRONMENT AS DRIVERS OF GALAXY EVOLUTION. II. THE QUENCHING OF SATELLITE GALAXIES AS THE ORIGIN OF ENVIRONMENTAL EFFECTS. ApJ 757: 4, URL `http://dx.doi.org/10.1088/0004-637X/757/1/4`.

Qu Y, Di Matteo P, Lehnert MD, van Driel W, Jog CJ (2011) Minor mergers and their impact on the kinematics of old and young stellar populations in disk galaxies. AAP 535: A5.

Rasmussen J, Ponman TJ, Verdes-Montenegro L, Yun MS, Borthakur S (2008) Galaxy evolution in Hickson compact groups: the role of ram-pressure stripping and strangulation. MNRAS 388: 1245–1264.

Rodriguez-Gomez V, Sales LV, Genel S, Pillepich A, Zjupa J, et al. (2017) The role of mergers and halo spin in shaping galaxy morphology. MNRAS 467: 3083–3098.

Rubin VC, Burstein D, Ford J W K, Thonnard N (1985a) Rotation velocities of 16 SA galaxies and a comparison of Sa, Sb, and SC rotation properties. ApJ 289: 81, URL `http://dx.doi.org/10.1086/162866`.

Rubin VC, Burstein D, Ford J W K, Thonnard N (1985b) Rotation velocities of 16 SA galaxies and a comparison of Sa, Sb, and SC rotation properties. ApJ 289: 81, URL `http://dx.doi.org/10.1086/162866`.

Ryder SD, Dopita MA (1994) The relationship between past and present star formation in galactic disks from CCD surface photometry. ApJ 430: 142, URL `http://dx.doi.org/10.1086/174389`.

Salim S, Fang JJ, Rich RM, Faber SM, Thilker DA (2012) GALAXY-SCALE STAR FORMATION ON THE RED SEQUENCE: THE CONTINUED GROWTH OF S0s AND THE QUIESCENCE OF ELLIPTICALS. ApJ 755: 105, URL `http://dx.doi.org/10.1088/0004-637X/755/2/105`.

Scodeggio M, Franzetti P, Garilli B, Zanichelli A, Paltani S, et al. (2005) The VVDS Data-Reduction Pipeline: Introducing VIPGI, the VIMOS Interactive Pipeline and

Graphical Interface. PUBL ASTRON SOC PAC 117: 1284–1295, URL `http://dx.doi.org/10.1086/496937`.

Shapiro SL (2005) Spin, Accretion, and the Cosmological Growth of Supermassive Black Holes. ApJ 620: 59–68, URL `http://dx.doi.org/10.1086/427065`.

Simien F, de Vaucouleurs G (1986) Systematics of bulge-to-disk ratios. ApJ 302: 564–578.

Smith R, Sánchez-Janssen R, Beasley MA, Candlish GN, Gibson BK, et al. (2015) The sensitivity of harassment to orbit: mass loss from early-type dwarfs in galaxy clusters. MNRAS 454: 2502–2516.

Solomon PM, Sage LJ (1988) Star-formation rates, molecular clouds, and the origin of the far-infrared luminosity of isolated and interacting galaxies. ApJ 334: 613–625.

Soucail G (2011) personal communication.

Soucail G (2012) Dark matter distribution in the merging cluster Abell 2163. A&A 540: A61, URL `http://dx.doi.org/10.1051/0004-6361/201118283`.

Sparke L, Gallagher J (2007) Galaxies in the Universe: An Introduction. Cambridge University Press.

Springel V, Di Matteo T, Hernquist L (2005) Modelling feedback from stars and black holes in galaxy mergers. MNRAS 361: 776–794, URL `http://dx.doi.org/10.1111/j.1365-2966.2005.09238.x`.

Takamiya T, Sofue Y (2002) Iteration Method to Derive Exact Rotation Curves from Position-Velocity Diagrams of Spiral Galaxies. ApJ 576: L15–L18, URL `http://dx.doi.org/10.1086/343028`.

Thronson J Harley A, Tacconi L, Kenney J, Greenhouse MA, Margulis M, et al. (1989) Molecular gas, the interstellar medium, and star formation in S0 and SA galaxies. ApJ 344: 747, URL `http://dx.doi.org/10.1086/167839`.

Tully RB (1988) Nearby galaxies catalog .

Tully RB, Fisher JR (1977) A new method of determining distances to galaxies. A&A 54: 661–673.

Übler H, Förster Schreiber NM, Genzel R, Wisnioski E, Wuyts S, et al. (2017) The Evolution of the Tully-Fisher Relation between z $\sim$ 2.3 and z $\sim$ 0.9 with KMOS^{3D}. ApJ 842: 121.

Verheijen MAW (2001) The Ursa Major Cluster of Galaxies. V. H I Rotation Curve Shapes and the Tully-Fisher Relations. ApJ 563: 694–715.

Vogt NP, Forbes DA, Phillips AC, Gronwall C, Faber SM, et al. (1996) Optical Rotation Curves of Distant Field Galaxies: Keck Results at Reshifts to Z approximately 1. ApJL 465: L15.

Wei LH, Vogel SN, Kannappan SJ, Baker AJ, Stark DV, et al. (2010) THE RELATIONSHIP BETWEEN MOLECULAR GAS AND STAR FORMATION IN LOW-

MASS E/S0 GALAXIES. ApJ 725: L62–L67, URL `http://dx.doi.org/10.1088/2041-8205/725/1/L62`.

Weigel AK, Schawinski K, Caplar N, Carpineti A, Hart RE, et al. (2017) Galaxy Zoo: Major Galaxy Mergers Are Not a Significant Quenching Pathway. ApJ 845: 145.

Young JS, Allen L, Kenney JDP, Lesser A, Rownd B (1996) The Global Rate and Efficiency of Star Formation in Spiral Galaxies as a Function of Morphology and Environment. AP 112: 1903.

Ziegler BL, Böhm A, Jäger K, Heidt J, Möllenhoff C (2003) Internal Kinematics of Spiral Galaxies in Distant Clusters. ApJL 598: L87–L90.